QST-M-56

QST Takasaki Annual Report 2024

Takasaki Institute for Advanced Quantum Science

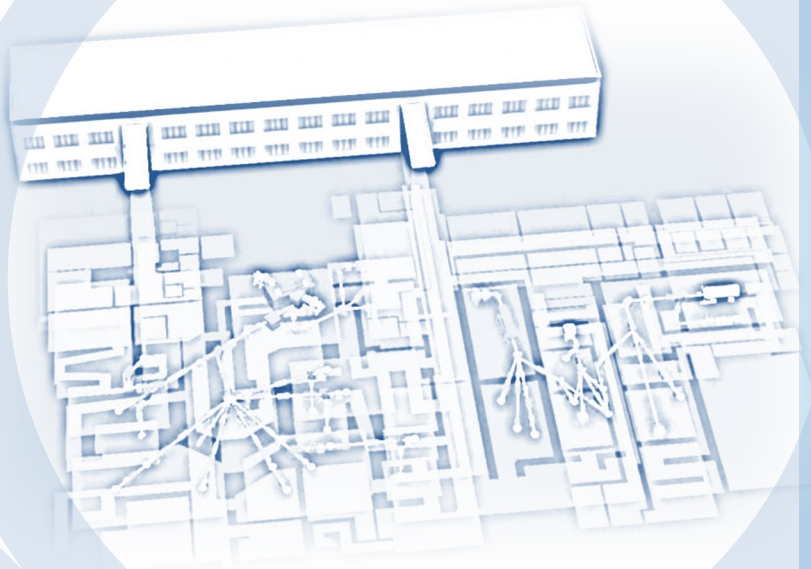

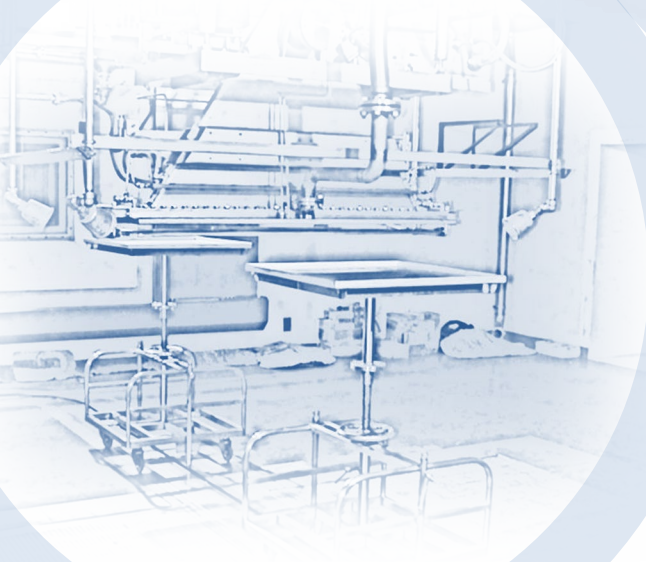

National Institutes for Quantum Science and Technology

Preface

HAKODA Teruyuki

Director General
Takasaki Institute for Advanced Quantum Science
National Institutes for Quantum Science and Technology (QST)

The Takasaki Institute for Advanced Quantum Science of the National Institutes for Quantum Science and Technology (QST), together with its preceding organizations, has been a global leader in quantum beam science for over six decades. Throughout this period, the institute continually strengthened its world-class research infrastructure, including state-of-the-art ion, electron, and gamma-ray irradiation facilities. Through pioneering technologies for the generation and control of charged particles and gamma rays, this institute has enabled highly precise material processing and advanced observation techniques, thereby establishing itself as a premier center for quantum beam research.

Since April 2024, the Takasaki Institute has been designated as one of Japan's Quantum Technology Innovation Hubs (QIH). Under this framework, fundamental research spanning a wide range of quantum technologies is being advanced, from next-generation quantum device development to fabrication and measurement techniques using quantum beams.

In fiscal year 2024 (FY2024), fifteen research projects in quantum technology and quantum beam science were conducted at the Quantum Materials and Applications Research Center, Department of Advanced Functional Materials Research, and Department of Quantum-Applied Biosciences. In addition, research and development on ion beam technology were pursued at the Beam Engineering Section of the Department of Advanced Quantum Beam Technology, which operates and manages three major radiation facilities: the Takasaki Ion Accelerators for Advanced Radiation Application (TIARA), a MeV electron accelerator, and cobalt-60 (^{60}Co) gamma-ray irradiation facilities. These beam facilities are open to users from industry, academia, and government research institutes, with beam time allocated through a rigorous proposal evaluation process.

This annual report summarizes research activities at the Takasaki Institute for FY2024 and is organized in two parts. Part I outlines the recent activities of all fifteen research projects and the Beam Engineering Section. Part II presents research and development results obtained using the quantum beam facilities of QST Takasaki, comprising fifty research reports across the fields of Quantum Materials and Applications, Materials Science, Life Science, and Quantum-Beam Technology, and eight status reports on facility operation and maintenance.

One of the key research topics addressed this year was the development of quantum devices that integrate rare earth elements with gallium nitride (GaN) semiconductors. This approach is aimed at realizing

room-temperature single-photon sources for quantum communication and advanced sensing technologies. Erbium (Er) ions were successfully implanted into GaN and activated via thermal annealing. Er ions emit photons at telecommunication wavelengths around 1.5 μm, which corresponds to the region of minimal transmission loss in optical fibers. Although oxygen co-implantation is generally known to enhance Er emission, the present study revealed a different behavior for Er implanted into GaN. Increasing the oxygen dose reduced the photon emission intensity, likely because of crystal-damage-induced nonradiative transitions. These findings provide valuable insights into the optimization of quantum light sources for future communication and sensing applications.

Another key topic is the creation of an in vitro model of slow-twitch muscles using soft structured gels. Slow-twitch muscles play essential roles in posture and daily activity but deteriorate with disease or inactivity, leading to a decline in the quality of life. Conventional culture dishes cannot reproduce slow-twitch characteristics owing to their stiffness and flatness. To address this limitation, gelatin-based gels with muscle-like softness and a fibrous architecture were fabricated using radiation processing. Muscle cells on soft gels exhibited increased expression of genes associated with the contraction and energy production characteristics of slow-twitch fibers. Grooved gels align cells in a manner similar to that of natural muscle fibers. By combining these features, aligned muscle cells with slow-twitch properties were successfully generated in vitro for the first time. This model is expected to accelerate the development of drugs and therapies for preventing muscle frailty and improving longevity.

In addition to these advances, fundamental biological responses to quantum-beam irradiation have also been investigated. DNA double-strand breaks (DSBs) are one of the most critical forms of DNA damage and a major source of radiation-induced mutations. A detailed analysis of mutations arising from DSBs in irradiated plants revealed that distinct DSB repair mechanisms operate depending on the developmental stage: in seeds, DSBs are mainly repaired with minimal end modification, whereas in seedlings, repair preferentially occurs after substantial processing of DSB ends. These findings highlight the importance of developmental stage in determining the outcomes of radiation-induced mutagenesis and breeding.

These three major radiation facilities operate continuously and safely throughout the year. To maintain global technological competitiveness, key components of the accelerator systems at TIARA are systematically upgraded annually. A recent notable achievement is the upgrade of the Heavy Ion Microbeam System (H-MB), which aims to contribute quantum-related research and applications through the formation of stable submicron ion beams. To achieve this goal, the H-MB was redesigned with higher demagnification by extending its beamline length, introducing a flexible quadrupole position system, and implementing an automatic beam-focusing system based on secondary electron imaging. As a preliminary experimental result, a micron beam size of approximately 1 μm × 1 μm was successfully achieved.

Through these efforts, we aim to advance quantum science and technology to promote industrial innovation and realize the United Nations Sustainable Development Goals (SDGs) and Society 5.0, Japan's vision for a future society. We appreciate your support for the activities of the Takasaki Institute for Advanced Quantum Science.

Part I

1. Quantum Material and Applications

2. Material Science

3. Life Science

2. Material Science

Appendix

Quantum Beam Facilities in QST Takasaki

- Takasaki Ion Accelerators for Advanced Radiation Application: TIARA
- Cobalt-60 gamma-ray and electron beam irradiation facilities

Part I

P1-1 Quantum Sensing Project

Leader : OHSHIMA Takeshi
URL: https://www.qst.go.jp/site/semiconductor/

To realize a Super Smart Society, it is essential to advance quantum technologies such as quantum sensing, quantum information, and quantum computing. Consequently, intensive R&D on quantum technologies is being conducted worldwide. The Quantum Sensing Project investigates quantum technologies based on spin defects in wide bandgap semiconductors, such as nitrogen-vacancy (NV) centers in diamonds. We introduce quantum defects into host semiconductors using energetic particle irradiation (both ion and electron beams) and characterize their optical and spin properties to establish methodologies for creating high-quality quantum sensors. In addition, we study radiation effects on semiconductor materials and devices to develop radiation-resistant technologies for space and nuclear applications. These technologies are expected to be applicable to future quantum devices operating in harsh environments.

Noise analysis for entanglement-enhanced sensing

Quantum entangled states can surpass the Standard Quantum Limit and approach what is known as the Heisenberg Limit. To explore this possibility, we are studying entanglement-enhanced sensing using arrays of NV centers in diamond. NV centers function as qubits even under ambient conditions, which makes them highly promising for sensing applications. A major obstacle, however, is decoherence. Under ambient conditions, decoherence in entangled systems occurs faster than in ensemble-based measurements. As a result, the achievable sensitivity remains limited to the level of the Standard Quantum Limit when the surrounding noise behaves like white noise, meaning that the advantage of entanglement cannot be obtained.

To overcome this issue, it is crucial to understand how environmental noise affects NV centers and to determine the conditions that allow entanglement to improve sensing performance. We therefore analyzed the noise environment around shallow NV centers and evaluated how fluctuations from nearby electron spins and lattice vibrations contribute to decoherence. These measurements allowed us to estimate the characteristic timescales and strengths of the dominant noise sources.

Based on these evaluations, we found that the expected sensitivity of entanglement-enhanced sensing can improve modestly, by less than 1 dB, compared with ensemble-based sensing, even when decoherence is considered. Moving forward, we plan to investigate how the noise characteristics vary under different diamond conditions and irradiation parameters, with the goal of identifying an optimal environment for realizing practical entanglement-enhanced sensing.

Development of a nanoscale characterization method for luminescent centers using cathodoluminescence

We developed a novel method for evaluating the nanoscale properties of luminescent color centers utilized as quantum sensors by analyzing the photon statistics of cathodoluminescence (CL) [1]. CL is a light emission phenomenon induced by electron beam irradiation and enables spatial resolution beyond the optical diffraction limit. It plays a vital role in visualizing the local optical response of materials in fields such as nanophotonics and quantum optical materials research. Recent investigations on CL photon correlation measurement have shown that pure statistical information originating from photon generation is disguised due to the randomness of the timing of electron irradiation [2]. To address this issue, we introduced a photon correlation measurement technique that removes the modulation effect of the electron beam and enables the extraction of photon statistics corresponding to individual electron excitation events.

This approach enables quantitative evaluation of statistical properties, such as Poisson distributions for randomly generated photons and super-Poisson (bunched) distributions for collectively generated photons. We found that electrons do not generate photons directly but produce intermediate particles (e.g., bulk plasmons or secondary electrons), which subsequently emit photons through a multi-step excitation process. In the experiments, using cerium-doped yttrium orthosilicate (Y_2SiO_5:Ce), we performed spatially resolved CL measurements while varying the sample thickness. The results exhibited that the degree of photon bunching increased with the number of intermediate particles generated, indicating a cascade-type excitation mechanism. In thinner regions near the surface, a reduction in photon emission efficiency was observed. This can be explained by the non-radiative relaxation due to surface traps.

The method developed in this study provides a novel analytical avenue for CL-based characterization, enabling not only high spatial resolution but also insight into excitation and emission processes. This paves the way for future applications in nanophotonic and quantum optical devices, involving quantum emitters or defect-based color centers.

References

[1] S. Yanagimoto *et al.*, Commun. Phys. **8**, 56 (2025). DOI: 10.1038/s42005-025-01978-6
[2] T. Yuge *et al.*, Phys. Rev. B **107**, 165303 (2023). DOI: 10.1103/PhysRevB.107.165303

P1-2 Spin-photonics in 2D Materials Project

Leader : SAKAI Seiji

URL: https://www.qst.go.jp/site/2d-spin-ja/

Our project aims to develop novel spin-photonic devices for future information technology applications, taking advantage of the low dimensionality and quantum electronic properties of two-dimensional (2D) materials and related low-dimensional nanostructures. Advanced quantum material synthesis and quantum-beam-based analysis techniques developed by our group, through extensive collaborations with colleagues both within and outside QST, enable us to investigate and design the local atomic and electronic structures as well as the spin- and photon-related quantum properties of 2D material-based heterostructures and devices.

Development of micro Mössbauer spectroscopy technique for quantum material and device research

To apply Mössbauer spectroscopy to the microscopic analysis of the local electronic and magnetic properties of quantum materials, such as heterostructures consisting of 2D materials and magnetic materials, and related devices, we newly developed an advanced synchrotron conversion electron Mössbauer spectroscopy (CEMS) technique based on ^{57}Fe synchrotron Mössbauer source (SMS) γ-rays at BL11XU of SPring-8, in collaboration with the Kansai Institute for Photon Science (Harima site) in QST.

Mössbauer spectroscopy is generally performed in transmission geometry. However, for measuring magnetic thin films less than a few hundred nanometers thick, conversion electron Mössbauer spectroscopy (CEMS) in backscattering geometry is often used. In conventional CEMS, which uses a radioisotope (RI) source, the thin film sample is placed in a gas-flow proportional counter, and backscattered conversion electrons with escape distances of approximately 100 nm are then detected under γ-ray irradiation from the RI source. This provides information within the escape depth from the surface, making CEMS a highly effective, non-destructive analysis method for magnetic thin films. However, the non-directional γ-ray and the severely restricted sample environment in conventional CEMS make microscopic Mössbauer measurements under high vacuum, at various temperatures, and under the applied electric fields and currents challenging.

Recently, an advanced CEMS technique using SMS was developed at BL11XU of SPring-8[1]. Thanks to its excellent beam properties, such as extremely high brilliance, a micrometer-scale beam size, and pure linear polarization, the synchrotron-generated focused ^{57}Fe Mössbauer γ-ray beam enables microscopic Mössbauer spectroscopy. These characteristics enable us to overcome the limitations of RI-based CEMS and pave the way for Mössbauer spectroscopy applications in the microscopic analysis of the electronic and magnetic properties of quantum materials and devices.

A new micro CEMS system consists of a CEMS chamber and a sample preparation chamber (Fig. 1(a)) [1]. The CEMS chamber is equipped with a two-stage, tapered micro channel plate (MCP) conversion electron detector (Hamamatsu Photonics), which provides a high multiplication factor of 10^6 and a high signal detection efficiency of 90%. This allows for highly sensitive microscopic measurements of the CEMS spectrum corresponding to a single atomic layer of ^{57}Fe atoms in 100-nm-thick films, from the 20-μm-wide irradiation area of the ^{57}Fe Mössbauer γ-ray beam. The chamber is maintained at a pressure of 10^{-9} Pa using an ion pump and a non-evaporable getter pump. The sample can be cooled down to 20 K (80 K) using liquid He (N_2) and heated up to 1,200 K using electron bombardment heating. Magnetic fields in the range of ± 500 Oe can be applied along the beam direction by using Helmholtz coils. Additionally, several microelectrodes can be installed in the chamber for operando measurements under electric fields and currents. The sample preparation chamber has a base pressure of 10^{-8} Pa and is used for offline thin film fabrication based on molecular beam epitaxy (MBE), as well as for sample pretreatment such as annealing, and structure characterization by reflection high energy electron diffraction. The CEMS chamber and the sample preparation chamber can be connected via a gate valve without breaking UHV for sample translation. This micro CEMS system enables microscopic Mössbauer spectroscopy of quantum materials and devices under various experimental conditions for the first time, contributing to the progress in quantum science and technology.

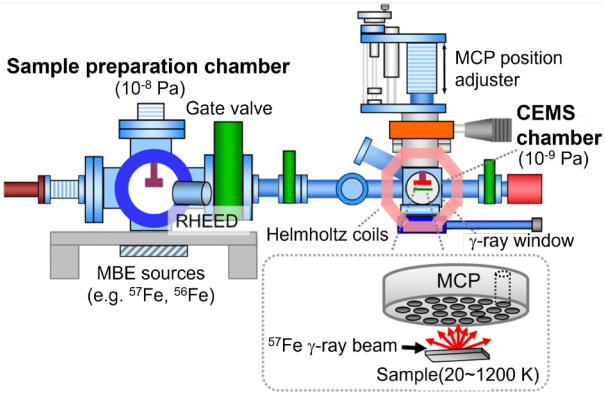

Fig. 1 Schematic of newly developed micro CEMS system in BL11XU of SPring-8. The system consists of an MCP-based CEMS chamber and a sample preparation chamber [1].

References

[1] T. Mitsui *et al.*, Interactions **245**, 347 (2024). DOI: 10.1007/s10751-024-02195-3

P1-3 Laser-cooled Ion Research Project

Leader : NARUMI Kazumasa
URL: https://www.qst.go.jp/site/laser-cooled-ion/

The objectives of the laser-cooled ion research project are to develop an ultrahigh-precision single-ion-implantation system to create any number of nitrogen-vacancy (NV) centers at any place in diamond, and to establish fundamental technologies to realize a quantum computer based on ion traps with $^{133}Ba^{+}$. The key techniques for both the objectives are trapping ions and laser cooling.

Development of a laser-cooled ion source for an ultrahigh-precision single-ion implanter [1]

Deterministic ion implantation and color-center creation methods on a nanometer scale provide a route towards scalable quantum information processing. For this purpose, we have developed an inherently deterministic single-ion implantation method based on a linear Paul trap (LPT) as a single-ion source since the laser-cooling technique can be applied to the trap system to obtain ultralow-temperature ions and manipulate single ions one by one.

The schematic view of a laser-cooled ion source constructed at QST for 100-keV ion implantation is depicted in Fig. 1(a). Doubly charged nitrogen ions (N^{2+}) produced in a sputter ion source was introduced into the LPT and sympathetically cooled with laser-cooled calcium ions (Ca^{+}). Both the sputter ion source and the LPT chamber were elevated up to +50 kV for the 100-keV ion implantation of doubly charged single ions into a grounded diamond crystal.

The LPT consists of four cylindrical rods and two gate electrodes A and B. The distance from the trap center axis to the surface of the rod electrodes was 3.0 mm and the distance between the gate electrodes A and B was 6.0 mm. Neutral Ca gases were photo-ionized by two lasers (423 nm and 390 nm). The LPT utilized an rf quadrupole field to confine charged particles transversely. The rf frequency and amplitude were 1.9 MHz and 20 V, respectively. The axial ion confinement was achieved by applying DC voltages to the two gates A and B ($V_A = V_B = +1.0$ V). The trapped $^{40}Ca^{+}$ were Doppler cooled with cooling (397 nm) and repumping (866 nm) lasers. Laser-induced fluorescence (LIF) photons were detected with a CCD camera.

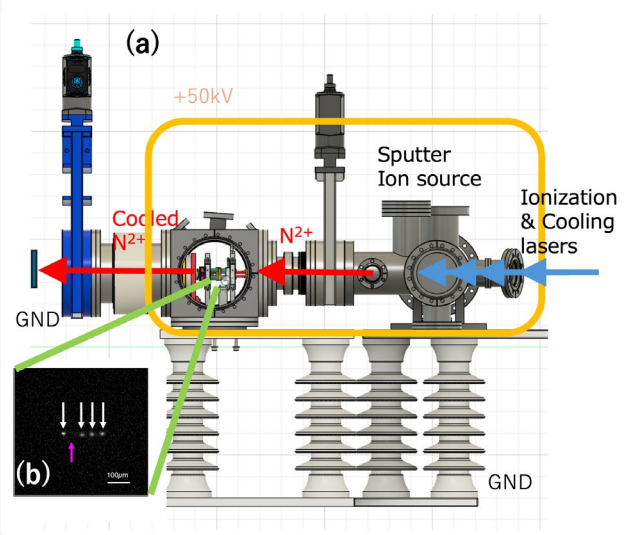

Fig. 1 (a) Schematic overview of the ultrahigh-precision single-ion implanter. (b) LIF image of a two-component string Coulomb crystal.

Figure 1(b) shows an example of LIF images obtained with the CCD camera, where each bright spot (↓) represents a single $^{40}Ca^{+}$. This spatially ordered structure is called a “Coulomb crystal”, where the translational motion of the ions is negligibly small, and each ion stays at its own position as the result of the balance between Coulomb repulsion and trapping electric field. A pink arrow (↑) indicates a sympathetically cooled dark ion.

Extracted doubly charged cold ions are accelerated and focused on a target by 50-kV electrostatic lenses to reach an ion kinetic energy of 100 keV on the target for an appropriate penetration into a target sample.

Ba^{+} ion trap systems for quantum information processing

Trapped ions are one of the promising platforms for implementing high-fidelity quantum information processing systems. Among various kinds of ions investigated so far, Ba^{+} ions have favorable properties in this respect, having major optical transitions in the visible range and a simple electronic structure allowing the electronic shelving technique for state discrimination. There exist various isotopes of Ba, having different nuclear spin I and thus different cooling/manipulation schemes. We have been constructing an ion trap system capable of cooling various isotope ions of Ba, particularly ^{138}Ba ($I = 0$), ^{133}Ba ($I = 1/2$, radioisotope), and ^{137}Ba ($I = 3/2$).

We have performed experiments for trapping and cooling $^{138}Ba^{+}$ ions using our first trap system. Neutral Ba atoms evaporated from an oven were ionized with an electron beam. By detecting and analyzing ions from the trap by a channel electron multiplier, we have confirmed that Ba ions have been trapped in the trap. However, no fluorescence signals accompanied by the laser-cooling process have been observed so far. The main difficulties of the present system lie in that we do not have means of evaluating the density of various isotopes of Ba atoms and ions inside the trap, and cooling in the radial direction is impossible due to the limited optical access of the chamber.

To overcome these difficulties, the second-generation trap system is under development. In this system, Ba atoms will be ionized via resonant photoionization, instead of electron impact. By doing so, only the desired isotopes are ionized. In addition, quantitative monitoring of Ba vapor density becomes possible by detecting the resonant fluorescence from Ba atoms. For this purpose, a new light

source consisting of a diode laser and a wavelength conversion crystal is developed. The new chamber containing the trap is equipped with large optical ports and thus improved optical access, allowing laser cooling both in the axial and the radial directions. With this second-generation trap system, we will attempt trapping and cooling various isotopes of Ba^+ ions.

Reference

[1] Y. Yuri *et al*., Prog. Theor. Exp. Phys. **2025** (2025) 023G01. DOI: 10.1093/ptep/ptaf019

P1-4 Quantum Optical and Spin State Control Project

Leader : KOHDA Makoto
URL: https://kohdalab-material-tohoku.jp/en/top-qst/

The goal of the Quantum Optical and Spin State Control Project is to bridge the gap between quantum and classical technologies necessary for the future quantum information society. We focus on the precise control of quantum states of single electron spins by exploiting defects in wide-gap semiconductors such as diamond and SiC. We are also working on the precise control of spin and magnetic structures for parallel computing and efficient magnetization reversal based on electron spin waves. Our research interests range from the creation of two-dimensional materials to the optical and electrical control of spin defects, as well as quantum device applications utilizing the spin degrees of freedom of semiconductors.

Enhanced interlayer electron transfer by surface treatments in mixed-dimensional van der Waals semiconductor heterostructures

Two-dimensional (2D) semiconductors such as monolayer WS2 are promising materials for next-generation optoelectronic and spintronic devices, where interlayer charge transfer plays a key role in device performance. However, when these 2D layers are integrated with III–V semiconductor substrates, the surface condition of the substrate strongly influences electron transfer across the interface. In this work, we investigated how substrate surface treatments—native oxide, oxide removal, and sulfur passivation—affect the interlayer electron transfer and excitonic photoluminescence (PL) properties of WS2/III–V heterostructures. The goal was to clarify the role of surface states and to explore interface engineering for improved charge transport.

Monolayer WS_2 was transferred onto III–V semiconductor substrates under three different surface conditions: (A) native oxide preserved, (B) oxide removed, and (C) oxide removed followed by sulfur passivation. Low-temperature polarized-PL spectroscopy was performed under near-resonant excitation to evaluate the relative contributions of neutral excitons, negatively charged excitons (trions), and localized excitons (Fig. 1).

For substrates with native oxide, the PL spectra were dominated by trion emission (Type A in Fig. 1), indicating electron accumulation in the WS_2 layer. After oxide removal, neutral exciton emission became predominant, while trion intensity was suppressed. A new low-energy shoulder appeared, which was attributed to localized excitons formed by defect states (Type B in Fig. 1). When sulfur passivation was applied after oxide removal, the PL spectrum remained dominated by neutral excitons, but the localized exciton shoulder disappeared, suggesting suppression of interfacial disorder (Type C in Fig. 1). A quantitative analysis of excitonic contributions confirmed a significant increase in neutral exciton fraction and a reduction of defect-related features upon surface treatment.

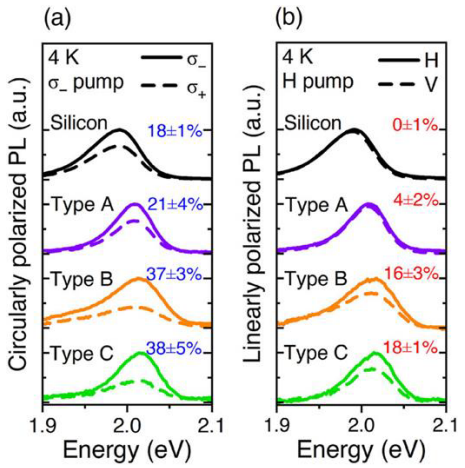

Fig. 1 Photoluminescence spectra at low temperature for the three surface conditions, showing the evolution of trion, neutral exciton, and localized exciton contributions.

The results demonstrate that native oxide layers hinder electron transfer from WS_2 to the III–V substrate, leading to higher electron density and trion formation in the monolayer. Removal of the oxide drastically enhances interlayer electron transfer, depleting excess electrons in WS_2 and thereby favoring neutral exciton emission. The emergence of localized excitons suggests that bare substrate surfaces introduce defect-related trap states. Importantly, sulfur passivation effectively reduces these defect states, eliminating localized exciton emission while maintaining efficient electron transfer.

This systematic trend highlights the crucial role of interface chemistry in governing charge redistribution at 2D/3D heterojunctions. By tailoring surface states through chemical treatments, excitonic populations can be controlled, which is highly relevant for exciton transport, valley physics, and optoelectronic applications.

This study establishes that surface treatments provide a powerful route to engineer interlayer electron transfer in mixed-dimensional van der Waals heterostructures. Oxide removal enables efficient electron transfer from WS_2 to the III–V substrate, while sulfur passivation suppresses defect-related localized excitons. These findings open new opportunities for optimizing charge and exciton dynamics in 2D/3D hybrid systems, offering guidelines for future device designs in optoelectronics, spintronics, and valleytronics.

References

[1] T. Odagawa *et al.*, APL Materials **12**, 061129 (2024). DOI: https://doi.org/10.1063/5.0214718

P1-5 Quantum Materials Theory Project

Chief : MATSUSHITA Yu-ichiro
URL: https://www.qst.go.jp/site/q-material-theory/

To further accelerate the adoption of quantum devices, the challenge is to understand and improve device properties in detail and to reduce noise under real-world conditions. The Quantum Materials Theory Project will analyze the fundamental properties of quantum devices, search for new materials for quantum devices, and develop protocols for noise reduction under real-world conditions from an approach based on theoretical simulations in collaboration with the experimental groups at the Quantum Materials and Applications Research Center (QUARC).

Revealing a mechanism to concentrate electronic states within a tiny energy range

Electronic properties in solid materials are governed by electronic states hosted by their crystal structures. One of our research targets is accurate simulation of electronic states in materials. The first-principles calculation methods have enabled people to analyze the electronic wavefunctions and energy spectra, which can accelerate exploration of novel materials. However, it does not tell us the governing mechanism as to why intriguing electronic states emerge in the corresponding crystals. If simplified mechanisms are at hand, mechanism-oriented efficient prediction should become available.

Recently, hydrogen compound superconductors with extraordinarily high transition temperatures (Tc) have been discovered at laboratory pressures of more than 1 megabar, that is comparable to earth's core. Among those superconductors, sulfur hydride H_3S is a pioneering system that exhibits Tc over 200 kelvin. Early simulation studies have already showed that this superconductivity is due to highly concentrated electronic states being metallic. The energy distribution of these states forms a peaked structure around the Fermi level, which boosts Tc to such high. However, why this system can host such peaked distribution has long remained elusive.

We recently addressed this problem theoretically. We analyzed a nearly-uniform electron model, where electrons are represented as plane waves and diffracted by ions' periodic potentials. Although this is a classic model for trivial metals, we found an unknown mechanism inducing electronic states' concentration. The key is hybridization of multiple plane-wave modes. Three or more plane waves are degenerate at linear regions in momentum space. By introducing the diffraction to induce hybridization of those degenerate states, anomalous concentration of the electronic energy spectrum emerges. We showed that this mechanism is working in H_3S, resolving the long-standing puzzle of this system, as well as opening an avenue for systematic design of superconductors with similar electronic concentration.

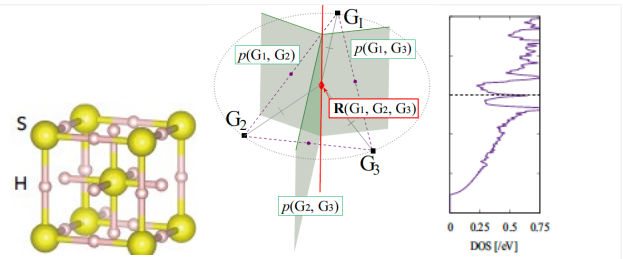

Fig. 1 Mechanism of concentration of electrons. (Left) Crystal structure of superconductor H_3S. (Center) Degeneracy of three plane waves. (Right) Resulting concentration of electrons, where dashed line indicate the Fermi level (metallic regime).

Boosting Performance of Quantum Machine Learning with Channel Attention

We explored a way to improve the performance of Quantum Convolutional Neural Networks (QCNNs), a type of quantum computer-based machine learning algorithm. QCNNs aim to do traditional computer learning tasks like recognizing images, but using the unique capabilities of quantum computers. However, quantum computers are still in their early stages, and making QCNNs practical requires minimizing the resources needed to run them. Our work focuses on enhancing QCNNs specifically for quantum phase classification, a task relevant to studying materials at a fundamental level.

The core idea is to introduce a "channel attention mechanism". In regular machine learning, "attention" allows the model to focus on the most important parts of the input data. We have adapted this concept to QCNNs. This new approach measures how important each of these channels is, and discards the less valuable ones. This is like a human focusing on a key detail in an image instead of trying to process everything at once. By strategically focusing on the most important channels, we show that they can achieve better accuracy in classifying quantum phases without drastically increasing the computational demands of the QCNN. In essence, they are making the QCNN more efficient. We also demonstrate that this channel attention mechanism requires adding a minimal number of quantum bits (qubits), the basic units of quantum information, to the system. This is a crucial point, as a smaller number of qubits makes the algorithm more feasible to run on current quantum hardware.

In conclusion, our research provides a practical step towards building more effective and efficient QCNNs for solving complex problems in the field of quantum materials science.

References

[1] R. Akashi, Phys. Rev. Res. **6**, 033012 (2024). DOI: 10.1103/PhysRevResearch.6.033012
[2] G. Budiutama *et al.*, Phys. Rev. A **110**, 012447 (2024). DOI: 10.1103/PhysRevA.110.012447

P1-6 Rare-Earth Quantum Device Project

Leader : SATO Shin-ichiro
URL: https://www.qst.go.jp/site/reqdev/

Rare-Earth Quantum Device Project is focused on developing quantum devices that combine rare-earth (RE) ions and gallium nitride (GaN) semiconductors. RE ions possess excellent properties as qubits and single-photon sources, and GaN is a semiconductor known for its high material quality and advanced nanofabrication technologies. This unique combination offers the potential to realize several novel functionalities that have not yet been achieved. These include electrically controlled single-photon sources (SPSs) operating at optical communication wavelengths and room temperature, integrated sources of quantum-entangled light on a chip, and real-time diagnostics inside GaN devices using quantum sensing techniques.

At present, the project is investigating methods to optically activate RE ions in GaN through ion implantation followed by thermal annealing. In addition, the local atomic structure of the implanted ions is being studied to better understand their behavior. We are also studying to develop quantum sensing applications using RE ions ions in GaN, and to enhance their spontaneous emission by coupling them to photonic crystal structures.

Erbium–Oxygen Co-Implantation in GaN for C-Band Photon Emitters

Erbium (Er) ions implanted into GaN semiconductors exhibit stable and narrow-linewidth emission near 1.5 μm at room temperature. This emission originates from intra-4f shell transitions and corresponds to the C-band wavelength range (1530–1565 nm), which is widely used in optical communications due to its low transmission loss in optical fibers. As a result, Er ions are considered promising candidates for SPSs in quantum communications.

To realize Er-doped GaN SPS, it is essential to precisely position individual Er ions, typically achieved through ion implantation. However, this process can cause damage to the crystal lattice, leading to non-radiative transitions. Therefore, appropriate thermal annealing is necessary to restore the crystallinity and enable optical activation of the implanted ions [1]. In this study, we examined the optical activation of Er ions implanted in GaN by combining ion implantation with post-implantation thermal annealing.

Er ions were implanted into epitaxially grown undoped GaN thin films on silicon substrates at the Takasaki Institute for Advanced Quantum Science, QST. The implantation energy was set to 350 keV, and the dose was 3×10^{14} cm^{-2}. Based on TRIM simulations, the implantation depth was estimated to be approximately 70 nm, with a peak concentration of 5×10^{19} cm^{-3}. Oxygen co-implantation was also performed at an energy of 50 keV. Following implantation, thermal annealing was carried out at 1200 °C for two minutes in a nitrogen atmosphere using an infrared furnace.

Figure 1 shows the variation in photoluminescence (PL) intensity of Er-implanted GaN as a function of O co-implantation dose. The inset presents the PL spectrum of Er-implanted GaN without O co-implantation. The excitation wavelength was 991 nm, and a long-pass filter with a cutoff at 1400 nm was used to detect Er-related emission only. The PL spectra revealed distinct emission peaks at 1513, 1537, and 1556 nm, which are attributed to crystal field splitting of the $^4I_{13/2}$ to $^4I_{15/2}$ transition within the Er 4f-shell.

Interestingly, the PL intensity decreased with increasing O co-implantation dose. Previous studies have reported that O co-implantation enhanced PL intensity in Er-implanted silicon and silicon carbide, likely due to the formation of Er–O complex defects that increase transition probabilities [2-4]. In GaN, however, such complexes may not form, or they may instead contribute to increased non-radiative transitions. Furthermore, higher implantation doses resulted in more residual damage even after annealing, which likely led to enhanced non-radiative recombination and reduced emission efficiency.

This work was supported by JST FOREST Program (Grant No. JPMJFR203G, Japan), JSPS KAKENHI (Grant Nos. JP18H01483; JP22H03880, Japan).

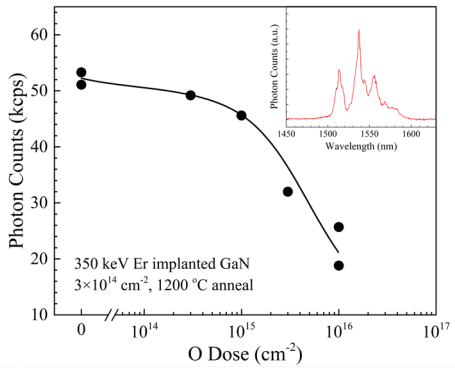

Fig. 1 PL intensity of GaN implanted with 350 keV Er ions (dose: 3×10^{14} cm^{-2}) as a function of co-implantation dose of 50 keV O ions. The inset shows the room-temperature PL spectrum of Er-implanted GaN without O co-implantation, measured under 991 nm excitation.

References

[1] S. Ito *et al.*, Nucl. Instr. Meth. B **547**, 16181 (2024). DOI: 10.1016/j.nimb.2023.165181
[2] R. A. Parker *et al.*, J. Appl. Phys. **130**, 145101 (2021). DOI: 10.1063/5.0055100
[3] J. Bader *et al.*, Nanomaterials **15**, 1499 (2025). DOI: 10.3390/nano15191499
[4] Y. Takahashi *et al.*, e-JSSN **21**, 262 (2023). DOI: 10.1380/ejssnt.2023-041

P1-7 Quantum Materials Ultrafine Fabrication Project

Chief : YAMAMOTO Hiroki
URL: https://www.qst.go.jp/site/euv-fabrication/

Quantum Materials Ultrafine Fabrication Project has been developing the functional inorganic organic hybrid materials and polymer materials for extreme ultraviolet (EUV) and next generation EUV lithography. We have synthesized resist materials such as metal resist and block copolymer with chemical synthesis. We aim to develop resist materials for EUV lithography and conduct fusion between top-down and bottom-up nanofabrication for next generation EUV lithography. We report herein two recent study: study on novel block copolymer via reversible addition-fragmentation chain-transfer (RAFT) polymerization as candidate block copolymers for next generation lithography and development of the inorganic organic hybrid resist materials for EUV lithography.

Synthesis of Polystyrene-block-poly(3-hydroxy-1-methacryloyloxyadamantane) (PS-*b*-PHAdMA) via RAFT Polymerization as Candidate Block Copolymers for Next Generation Lithography [1]

The self-assembly of block copolymers (BCPs) has appeared over the past two decades as a promising method for future patterning techniques for manufacture of integrated circuits and memory devices. However, generation of sub-20 nm feature sizes is challenging using conventional BCPs such as polystyrene-*block*-poly(methyl methacrylate) (PS-*b*-PMMA). The realization of further miniaturization at scales of sub-10 nm in semiconductor devices depends on the design and development of new BCP materials.

In this study, the novel BCPs composed of polystyrene (PS) and polymers of 3-hydroxy-1-methacryloyloxy -adamantane (HAdMA) were synthesized by RAFT. The PHAdMA block has an elevated glass transition temperature (T_g) and is a bulky and sterically hindered segment. We have demonstrated the synthetic conditions to achieve controlled polymer molecular weights and molecular weight dispersity. The physical properties, including solubility, thermal stability, film-forming capacity, self-assembly in solvent annealing and thermal annealing of polystyrene-*block*-poly(3-hydroxy-1-methacryloyloxy-adamantane) (PS-*b*-PHAdMA) are investigated in detail.

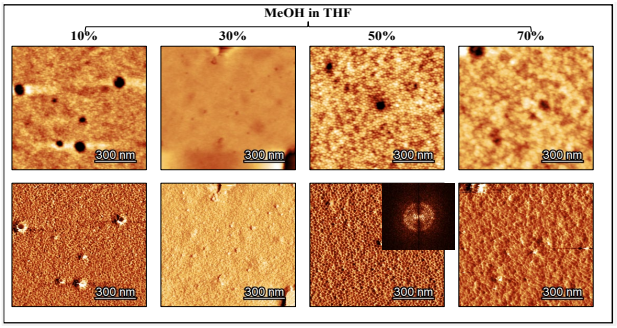

Fig. 1. AFM images of thin films of PS58-b-PHAdMA57 exposed to solvent vapor of differing composition for 6 h, from left to right, MeOH/THF volume ratios of 10 %, 30 %, 50 % and 70 %.

These results indicate that this block copolymer is an excellent candidate for next-generation lithography materials. In particular, the analysis of the microphase morphologies in PS-*b*-PHAdMA thin films using atomic force microscopy (AFM) (as shown in Fig.1) and small angle X-ray scattering (SAXS) showed clear evidence of ordering of the BCPs into cylinders. This study significantly expands the ability of block copolymer lithography for producing patterns needed for nanoscale device fabrication.

Study on Resist Performance of Inorganic-Organic Resist Materials for EUV and EB lithography [2]

Beyond the 16 nm node, EUV lithography has finally applied to mass production line in a portion of advanced lithography. For the advancement of EUV lithography, the resist materials and processes are the most critical issues. The development of resists with less than 10 nm resolution gives rise to important problems such as pattern collapse and poor pattern transfer. Therefore, the development of new resist materials is required to accomplish less than 10 nm patterning instead of chemically amplified resists. Inorganic-organic resist materials are expected as one of material innovation because it can give the possibility of higher resolution, sensitivity and etch durability. In this study, we synthesized three kinds of hybrid inorganic-organic resist materials known as metal-oxo clusters as model compounds and examined the lithographic performances using EUV exposure tool, electron beam (EB) lithography.

In order to investigate the difference in sensitivity and resolution between Ti-based and Zr-based oxo clusters by using EUV and EB exposure, we evaluated their resist performance. Fig. 2 shows SEM micrographs of line & space patterns delineated on (a) Ti-based oxo and (b) Zr-based clusters films. Although the exposure dose was not optimized, the patterns of Ti-based oxo clusters and Zr-based clusters showed a 100 nm and 50nm line and space patterns, respectively. They were obtained at a dose of 250 and 80 μC/cm^2, respectively. We clarified that the sensitivity of Ti-based oxo clusters and Zr-based oxo clusters showed the similar tendency in both EUV and EB.

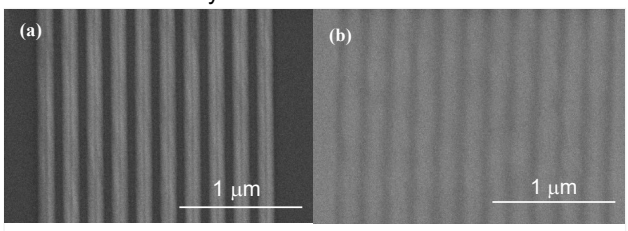

Fig. 2 SEM micrographs of L&S patterns delineated (a) Ti-based and (b) Zr-based oxo clusters by EB lithography system.

References

[1] H. Yamamoto *et al*., Polymer. **318** 127983 (2025). DOI: 10.1016/j.polymer.2024.127983
[2] H. Yamamoto *et al*., Jpn. J. Appl. Phys. **63** 04SP87 (2024). DOI: 10.35848/1347-4065/ad38c5

P2-1 Hydrogen Energy Conversion Device Project

Leader : SAEKI Morihisa
URL: https://www.qst.go.jp/site/adv-catl/

The hydrogen energy market is expanding worldwide, driven by the “Green Growth Strategy towards 2050 Carbon Neutrality”. To meet growing demand, our project focuses on functional materials and devices for hydrogen production, storage, and utilization. One of our key targets is the development of electrocatalysts, which play a crucial role in hydrogen fuel cells. Commercial fuel cells currently use Pt on carbon (Pt/C) as the cathode catalyst for the oxygen reduction reaction. Researchers have also explored silicon carbide (SiC) as a support for Pt catalysts to improve fuel-cell durability. This report investigates the effects of ion-beam irradiation on two support materials – glassy carbon (GC) and SiC nanotubes – examining their microstructural evolution as a function of fluence.

Ion irradiation-induced anomalous structural evolution in GC [1]

The ORR activity of Pt nanoparticles supported on GC was enhanced by introducing defects into the GC support via ion irradiation [2]. To elucidate this effect, we irradiated GC substrates with 380-keV Ar^+ ions at fluences ranging from 1.0×10^{14} to 1.0×10^{16} ions cm^{-2}.

Cross-sectional transmission electron microscopy (TEM) revealed a transformation from turbostratic graphite to amorphous carbon at fluences above 1.0×10^{15} ions cm^{-2}. Figure 1 shows selected-area electron diffraction (SAED) patterns acquired from an ~280-nm near-surface region at fluences of 1.0×10^{15} and 1.0×10^{16} ions cm^{-2}. At 1.0×10^{15} ions cm^{-2}, the pattern exhibited a halo, indicating amorphization. At fluences above 2.5×10^{15} ions cm^{-2}, a disconnected diffraction ring assigned to the (002) reflection was observed. This suggests that the amorphized carbon would slightly orient along a *c*-axis so that *c*-planes of graphite could align parallel to the surface at higher fluences. Because graphite basal planes are chemically more stable than edge planes, such (00*l*)-plane exposure may render the surface more electrochemically inert during operation. Therefore, ion irradiation may offer a route to enhancing the corrosion resistance of carbon supports in catalytic electrodes.

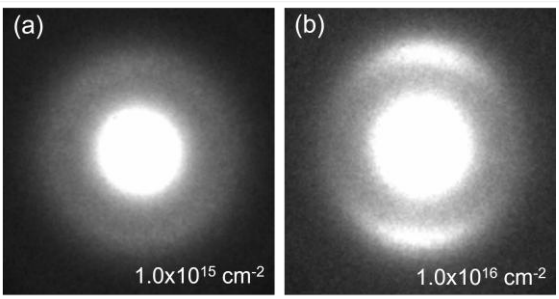

Fig. 1 SAED patterns of the irradiated GC substrates at fluences of (a) 1.0×10^{15} and (b) 1.0×10^{16} ions cm^{-2}.

Ion irradiation induced microstructural development of polycrystalline double-thick-walled SiC nanotubes [3]

Polycrystalline double-thick-walled (DTW) SiC nanotubes were investigated under ion irradiation. In-situ TEM observations were performed on two types of polycrystalline DTW SiC nanotubes with a wide and narrow spacing between the outer and inner nanotubes during irradiation with 200-keV Si^+ ions at room temperature.

The critical doses of amorphization for both DTW SiC nanotubes were higher than those reported for bulk SiC in previous studies because of the increased defect mobility due to a large number of inherent structural defects and to the larger specific surface area arising from their nanoscale size and tubular shape. Even at doses of complete amorphization, the double wall structure in which a thinner nanotube was enclosed within a thicker nanotube was maintained. Namely, amorphous DTW SiC nanotubes were successfully synthesized for the first time via ion irradiation of both polycrystalline DTW SiC nanotubes as shown in Fig. 2. In-situ TEM further indicated that the inner and outer tube diameters and lengths of both inner and outer nanotubes increased with increasing the irradiation dose up to near complete amorphization and then decreased. At doses exceeding 20 displacements per atom, polycrystalline DTW SiC nanotubes with a wide and narrow spacing between the outer and inner nanotubes were transformed into amorphous SiC nanotubes and SiC nanowires, respectively.

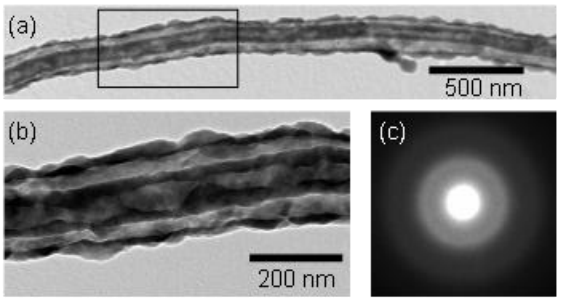

Fig. 2 (a) Low magnification TEM image, (b) middle magnification TEM image and (c) SAED pattern of the amorphous DTW SiC nanotube with a wide spacing between the outer and inner nanotubes.

References

[1] H. Okazaki *et al*., Appl. Surf. Sci. **714**, 164525 (2025). DOI: 10.1016/j.apsusc.2025.164525
[2] T. Kimata *et al*., Phys. Rev. Mater., **6**, 035801 (2022). DOI: 10.1103/PhysRevMaterials.6.035801
[3] T. Taguchi *et al*., e-J. Surf. Sci. Nanotech. **23**, 314 (2025). DOI: 10.1380/ejssnt.2025-040

P2-2 Nanostructured Polymer Materials Project

Leader : ZHAO Yue
URL: https://www.qst.go.jp/site/functional-polymer-research-j/

Nanostructured Polymer Materials Project is developing advanced functional polymer materials for energy devices such as fuel cells, electrolyser and metal-air batteries, by quantum beam technologies. We have synthesized the high-performance proton- and anion-conducting electrolyte membranes using γ-rays and electron beams, and characterized their nanostructures using scattering, imaging and simulation techniques. We report herein our latest research progress on the deep understanding of membranes' structure-property correlations towards Materials Informatics.

Structural factors for the chemical stability of graft-type polymer electrolyte membranes evaluated from the local hydration number [1]

The chemical stability of a polymer electrolyte membrane (PEM) against radicals that generated during the fuel cell operation is a major problem for their applications. To improve chemical stability, two main strategies have been proposed: one is the synthesis of durable polymers, and the other is the use of radical scavengers. However, both strategies require complicated production procedures for new PEMs and have not yet satisfied durability and conductivity requirements for a practical use. In this work, we propose an alternative "third" strategy, that focuses on the structural control, especially ion-channels, with a few nanometer scale, to inhibit chemical degradation in PEMs.

We have made a series of radiation-grafted PEMs, consisting of poly(styrene sulfonic acid) grafted onto poly(ethylene-co-tetrafluoroethylene) (ETFE-g-PSSA) with ion exchange capacities (IECs) ranging from 0.8 to 2.5 mmol/g. Using PSF analysis, we have visualized the detailed ion-channel structure, and experimentally evidenced that their chemical stability (represented by the conductivity loss σ/σ_0 in the Fenton test for 24 h) could be dramatically improved by minimizing radical attack to polymer chains through the control of λ_{local} that is defined as the number of water molecules surrounding sulfonic acid groups in ion-channels (Fig. 1). Good stability can be achieved at IEC < 1.7 mmol/g with spherical ion-channels and λ_{local} ~ 6.5. A further increase in IEC leads to an increase in λ_{local}, resulting in a morphological transition to bicontinuous-shaped ion-channels, and a severe decrease in stability. Therefore, it is one of the inevitable strategies that to suppress the hydration level down to λ_{local} ~ 6.5, for achieving high chemical stability of these grafted PEMs whereas maintaining good conductivity.

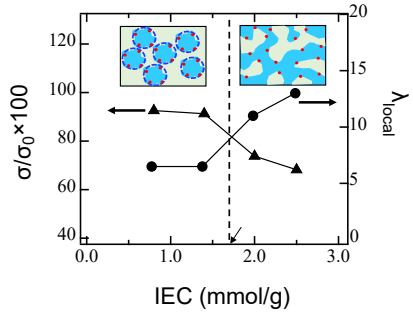

Fig. 1 Plots of σ/σ_0 and λ_{local} as a function of IEC.

Long functional graft polymer induced multiscale morphological inversion and enhanced anion transport efficiency in radiation-grafted anion exchange membranes [2]

To understand the long functional graft polymer induced multiscale morphological inversions and the enhanced anion transport efficiency, we applied PSF analysis to visualize hierarchical structures in radiation-grafted anion-exchange membranes (AEMs), consisting of *p*-(2-imidazoliumyl) styrene graft-polymers onto ETFE films with different grafting degrees (14% for AEM14 and 42% for AEM42), where AEMs are treated as a 3-component system, containing EFTE base polymer (BP), graft polymer (GP) and water (W). The entire structural patterns of AEM14 and AEM42 were illustrated in Fig. 2. The hydrophilic/hydrophobic phase-inversion in tens of nm scale was confirmed in that the GP/W particles dispersing in the BP matrix in AEM14, whereas AEM42 has a network structure of BP domains in GP/W matrix. The bicontinuous ion-channel inversion in a few nm scale from "water-in-polymer" in AEM14 to "polymer-in-water" in AEM42 was also revealed. It is the increase in GD in this type of AEMs that results in the multiscale structural inversions and enhances the ion transport efficiency.

The extraction of these unique structural factors enables the prediction of scattering intensity profiles of AEMs without a real scattering experiment, which is exciting in the era of AI for designing high performance AEMs for a wide range of energy conversion applications.

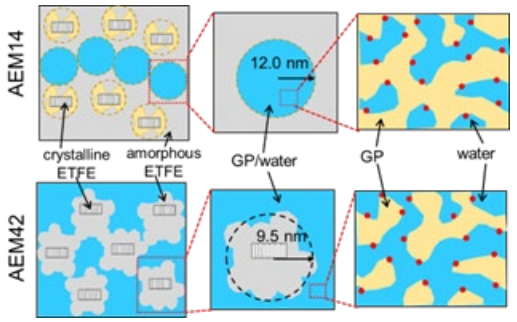

Fig. 1 Schematics of hierarchical structures in AEM14 and AEM42.

References

[1] K. Yoshimura *et al.*, ACS Appl. Polym. Mater. **6**, 13585 (2024). DOI: 10.1021/acsapm.4c02232
[2] Y. Zhao *et al.*, Macromolecules **58**, 663 (2025). DOI: 10.1021/acs.macromol.4c02454

P2-3 Energy Regeneration Materials Project

Leader : SEKO Noriaki
URL:https://www.qst.go.jp/site/kankyou/

In our Project “Energy Regenerative Materials”, we develop high-performance polymer materials using electron beam and gamma-ray irradiation graft polymerization techniques. Specifically, we focus on developing high-performance polymer adsorbents for the removal and recovery of rare metals from industrial wastewater [1]. We also synthesize adsorbents capable of capturing ultra-trace isotopes from seawater, enabling precise analysis and tracking of radioisotope distribution [2].

Development of a bifunctional adsorbent for heavy metal removal from industrial wastewater [1]

In response to the growing environmental concerns over heavy metal contamination in industrial wastewater, this study presents the development and evaluation of a novel bifunctional adsorbent capable of removing both cationic and anionic heavy metals. The adsorbent was synthesized by grafting tertiary amine (NMA) and phosphoric acid (PMA) functional groups onto a polyethylene/polypropylene nonwoven fabric (NF) using electron beam irradiation-induced copolymerization.

Optimal grafting conditions were determined to be 12 wt% NMA, 8 wt% PMA, a radiation dose of 100 kGy, and a reaction time of 30 minutes. Characterization techniques including FTIR, TGA, and SEM/EDS confirmed the successful incorporation of functional groups onto the polymeric material. As shown in Figure 1, the resulting adsorbent, NF-g-Poly(NMA-co-PMA), was immersed in the test solution containing various heavy metal ions for the adsorption. The results demonstrated that most of the heavy metal ions could be adsorbed effectively under weakly acidic conditions (pH 5.0). Furthermore, the adsorbent showed strong selectivity in mixed metal solutions, with the order of adsorption preference being Pb(II) > Cu(II) > Cd(II). The adsorption mechanisms were attributed to ion exchange and electrostatic interactions: protonated tertiary amines facilitated anion adsorption, while deprotonated phosphoric acid groups enabled cation binding.

This bifunctional adsorbent offers a promising solution for simultaneous removal of diverse heavy metals in a single treatment step, making it highly applicable for industrial wastewater management.

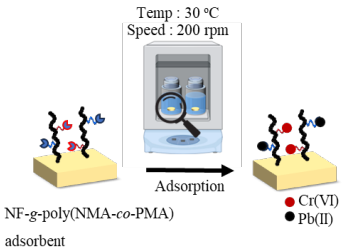

Fig. 1 Adsorption of heavy metal ions by the NF-g-Poly(NMA-co-PMA) fabric adsorbent

Simple and Convenient Preconcentration Method for Uranium Isotopic Analysis in Seawater [2]

Ultra-trace uranium isotopes (^{236}U and ^{233}U) are valuable for radioecological assessments and ocean circulation tracking, but their concentrations in seawater are extremely low. Conventional shipboard pre-concentration methods using iron co-precipitation are labor-intensive, require hazardous reagents, and typically yield only 50% to 80% recoveries. This study developed and optimized a simple and efficient uranium pre-concentration method using a fabric-like amidoxime adsorbent that can be performed in both laboratory and shipboard environments. The adsorbent was prepared by modifying of the commercially available polyethylene/polypropylene nonwoven fabric. Electron beam irradiation generated free radicals on the polymer backbone, followed by graft copolymerization of acrylonitrile and methacrylic acid. Subsequently, an amidoximation reaction converts the cyano groups into amidoxime groups, which are then treated with an alkali to enhance hydrophilicity and form chelating groups. The resulting adsorbent has an amidoxime group density of approximately 4.0 mmol/g.

For a typical adsorption experiment, 5 g of adsorbent was immersed in 500 g natural seawater (pH ~8) for the uranium adsorption. We found that almost 100% of uranium in the seawater was adsorbed. Furthermore, the adsorbed uranium could be easily desorbed by acid. As shown in Figure 2, desorption tests showed that immersing the

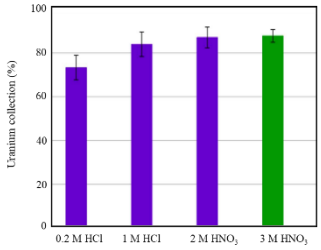

Fig. 2 Percent of uranium collection under various desorption condition

uranium-loaded adsorbent in HCl or HNO_3 for 1 h achieved more than 70% recovery. The collected and pre-concentrated uranium after desorption can be used for further isotopic analysis. This method simplifies uranium isotope preconcentration by eliminating the need for chemical co-precipitation and enabling efficient processing of large seawater volumes both in the lab and on-board vessels. It offers high recovery, reproducibility, and compatibility with downstream isotopic analysis, making it well suited for environmental monitoring of anthropogenic uranium isotopes and for oceanographic tracer studies.

References

[1] Y. Limsuwan *et al.*, *Polymer* **315**, 127792 (2024). DOI: 10.1016/j.polymer.2024.127792
[2] M. Abe *et al.*, *Anal. Methods*, **16**, 2478 (2024). DOI: 10.1039/d3ay01381b

P2-4 Advanced Biodevice Project

Leader : TAGUCHI Mitsumasa

URL: https://www.qst.go.jp/site/biocompatible-materials-j/

Advanced Biodevice Project is developing innovative functional biodevices using quantum beam crosslinking and oxidation reactions. These devices are expected to be applied across medical fields, including diagnostics, therapy, drug discovery, and regenerative medicine.

Slow-twitch muscles characterized aligned myotubes formation

Skeletal muscles are categorized into slow-twitch (type I and IIa fibers, oxidative metabolism) and fast-twitch (type IIx and IIb fibers, glycolytic metabolism). While fiber-type shifts occur with development and aging, the stimuli driving these changes remain unclear.

To investigate this, gelatin solutions were irradiated with γ-rays to generate OH (hydroxyl) radicals, inducing crosslinking and forming gels with tunable elasticity. Unlike physical gels, the chemically crosslinked gel did not dissolve even at 37 °C. Gels with elastic moduli of 10–230 kPa were created by adjusting gelatin concentration (10 or 15 wt%) and irradiation dose (8–30 kGy), covering the physiological range of skeletal muscle (10–100 kPa) (Fig. 1). Microgrooves (3–50 μm width, 2 μm depth) were imprinted using PDMS molds to study the effect of topography.

Using this gel as a cell culture scaffold, we seeded mouse-derived C2C12 myoblasts and analyzed cell morphology and gene expression to assess the effects of mechanical stimulation on myotube formation and the transition to distinct myofibrillar types.

C2C12 myoblasts could differentiate into myotubes on 10-100 kPa gels and detached on 160-230 kPa gels. Thus, we analyzed the fiber type-characterizing gene expression in myotubes cultured on 10-100 kPa gels and the dish (Fig. 2). The expression of marker genes for type I and IIa fibers (MYH7 and MYH2) were increased in myotubes cultured on 10–100 kPa gels compared with that in the dish. The expression of marker genes for oxidative metabolism (GLUT4 and Myoglobin) was also increased in myotubes cultured on 10–100 kPa gels. In particular, myotubes cultured on 10 kPa gels showed the most increase in these expression levels. Additionally, PGC-1α, a transcriptional coactivator that regulates the formation of type I and IIa fibers with high oxidative metabolism, was increased in myotubes cultured on 10 kPa gel. Therefore, mechanical stimulation from low elasticity gels induced myotube shifts toward the genetic characteristics of slow-twitch muscle via upregulation of PGC-1α.

Subsequently, C2C12 myotubes cultured on gels with groove widths ranging from 3 to 50 μm to assess the effect of microgrooves on myotube formation and the transition to distinct myofibrillar types. Myoblasts could differentiate into myotubes on gels with each groove. Microgrooves (3–10 μm) enhanced myoblast differentiation and myotube orientation along the grooves compared to that under the flat condition (Fig. 3). On the other hand, Microgrooves did not affect the gene expressions of characterizing fiber types and PGC-1α, regardless of groove widths. Therefore, mechanical stimulation from small width of microgrooves enhances myoblast differentiation and myotube orientation, without affecting the shift to the genetic characteristics of any fiber types.

This study presents a method to model highly oriented slow-twitch muscle by controlling gelatin gel elasticity and microstructure. These models may help clarify mechanisms behind muscle loss in bedridden or cancer patients, where slow-twitch fibers are preferentially affected.

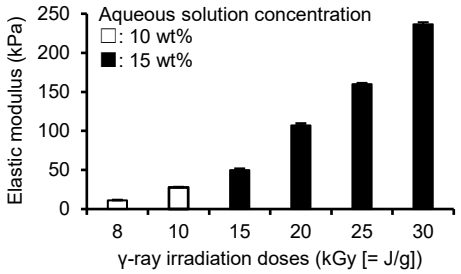

Fig. 1 Crosslinked gel with compressive elastic modulus using a combination of solution concentrations and irradiation dose.

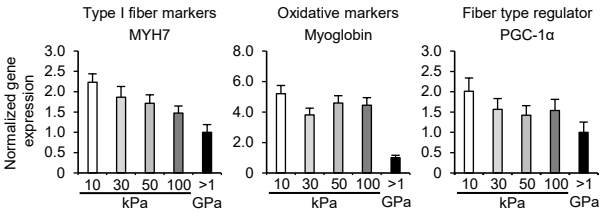

Fig. 2 Representative genes expression of myotubes cultured on crosslinked flat gels.

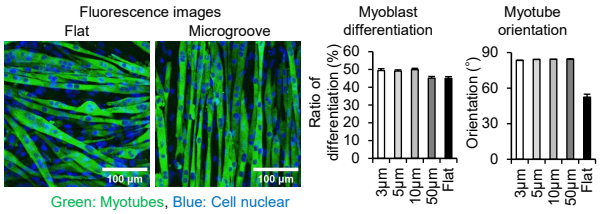

Fig. 3 Representative fluorescence images of myotubes, myoblast differentiation (left), and myotube orientation on gels with flat and microgroove condition (right).

References

[1] H. Hamaguchi *et al.*, Sci. Rep. **15**, 27825 (2025). DOI: 10.1038/s41598-025-12744-7

P3-1 Radiotracer Imaging Project

Leader : NAOKI Kawachi
URL: https://www.qst.go.jp/site/ri-imaging/

The Radiotracer Imaging Project quantitatively acquires and visualizes spatiotemporal distributions of radiotracers to elucidate biological processes and functions, using PETIS (Positron-Emitting Tracer Imaging System), PET, and gamma camera systems. We are developing an integrated platform for live radiotracer imaging that spans isotope production and tracer synthesis, nuclear imaging instrumentation, device-specific acquisition and reconstruction protocols, and quantitative kinetic modeling—including multi-isotope analyses. These capabilities are applied to reveal the transport and transformation of elements and molecules in living systems, with emphasis on plant science, agriculture, environmental resilience, and medical applications.

Sodium excretion mechanism in *V. marina*

In recent years, the over-irrigation farming, sea level rise due to global warming, storm surges and seawater intercept into farmland caused by super typhoons, would expect to affect approximately 50% of the world's farmland with soil salinity by 2050. Domesticated plants are sensitive to salt stress, and they were not bred for salt tolerance, and most of them show salt sensitivity. Consequently, there is a global need to develop salt tolerant crops.

Salt tolerance is an important function as increasing areas of arable land are being degraded by soil salinity. Wild plants in the genus *Vigna* serve as valuable resources of tolerance to various stresses, including salinity. In our previous work, we screened the genetic resources of the genus *Vigna* and identified several accessions that have independently evolved salt tolerance. We investigated the salt tolerance mechanism of *V. marina*, which exhibits high salt tolerance among these accessions. *V. marina* can survive at high salt level similar to seawater and has a mechanism that prevents sodium (Na) accumulation in its leaves, stems and roots (Noda *et al*., 2022). To investigate the detail salt tolerance mechanism in *V. marina,* we used the Positron-Emitting Tracer Imaging System (PETIS) and radioactive sodium (^{22}Na) to measure Na concentration changes with real time in each plant organ and in the hydroponic solution. As a result, it was revealed that ^{22}Na was initially taken up by the roots of *V. marina* and subsequently excreted from the roots (Figure 1), indicated that *V. marina* has the ability of Na excretion. Interestingly, *V. marina* actively excreted ^{22}Na from the roots during the light period but not the dark period, and this cycle was repeated (Figure 2). It was suggested that the Na excretion in *V. marina* is diurnally regulated. Na-22 excretion was also observed in other salt-tolerant accessions, but *V. marina* exhibited the highest excretion activity.

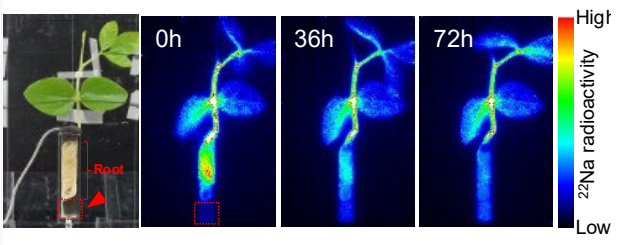

Fig. 1 Visualization of ^{22}Na excretion by PETIS in *V. marina*. Color change from blue to red indicates ^{22}Na accumulation. Red arrow and dot box indicate hydroponic solution area.

To identify the genes involved in Na excretion in *V. marina*, RNA was extracted from root samples taken under light and dark period, and a whole-genome gene expression analysis was performed. As a result, the *SOS1* gene, which encodes a Na transporter that excretes Na ions that have entered the cell, showed consistently high expression levels in *V. marina* compared to other accessions. Furthermore, the expression level of the *SOS2* gene, which activates the *SOS1* gene, exhibited diurnal regulation in *V. marina*, coinciding with ^{22}Na excretion from the roots. Therefore, Na excretion ability could be determined by the *SOS1* gene expression level, while diurnal regulation would be determined by the *SOS2* gene expression pattern (Noda *et al*., 2025).

A key point of this investigation is that the components constituting the salt tolerance mechanism of *V. marina* are common to many plants. Even in crops like rice and soybeans, enhancing the expression of these genes could potentially replicate the salt tolerance mechanism of *V. marina*. Based on these research findings, we anticipate not only the creation of salt-tolerant crops, but also the further contribution to highly sustainable agricultural practices such as seawater agriculture.

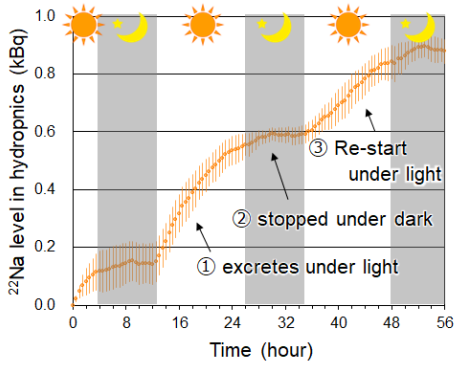

Fig. 2 Indexed amount of ^{22}Na across time in the hydroponic solution. Light and dark periods are indicated as white and grey in the plot, respectively. Error bars indicate standard errors.

References

[1] Y. Noda, *et al*., Breed. Sci. **72 (4)**, 326-331 (2022). DOI: 10.1270/jsbbs.22012
[2] Y. Noda, *et al*., Plant Cell Environ. **48**, 3925-3938 (2025). DOI: 10.1111/pce.15402

P3-2 Environmental-Stress Tolerance Genes Project

Leader : HASE Yoshihiro

URL: https://www.qst.go.jp/site/ion-beam-mutagenesis/

Our project aims to create novel genetic resources associated with environmental-stress tolerances of crops and microorganisms in order to contribute to sustainable agriculture. In particular, our project focuses on the experimental evolution combined with mutagenesis using quantum beams, because appropriately increased mutation frequency is expected to accelerate the adaptation to stress environment and also stimulate the accumulation of beneficial mutations. Here we report our recent achievements regarding the choice of DNA double-strand break (DSB) repair pathways in Arabidopsis [1] and the high-temperature tolerant mutants of rhizobium [2].

Different DSB repair pathways are employed following the irradiation of Arabidopsis seeds and seedlings

Recent comparative genomic analyses suggest that DNA rearrangements such as translocations and large deletions played an important role in adaptation, domestication and improvement of several crop species. Therefore, induction of DNA rearrangements is a potentially effective way to develop novel genetic resources. However, generation of DNA rearrangements were not fully analyzed compared to point mutations because of the difficulty to detect sufficient number of DNA rearrangements in M_2 generation. In this study, for efficient detection of DNA rearrangements, clonal sectors originating from single mutated cells were excised in M_1 plants after Arabidopsis dry seeds or seedlings were irradiated with carbon ions. Whole genome sequencing was performed using the isolated DNA and the feature of the rejoined site of DNA rearrangements were examined. We found that large deletion and insertion were frequently associated with the rejoined site in case of seedling irradiation compared to the case of dry-seed irradiation. This suggests that the broken DSB ends were more extensively processed in the case of seedlings irradiation. Two non-homologous end-joining pathways that are canonical non-homologous end-joining (c-NHEJ) and alternative end-joining (alt-EJ) have been thought to contribute to the generation of DNA rearrangements. The c-NHEJ rejoins DSB ends with minimal processing while alt-EJ rejoins DSB ends after extensive processing. These facts suggest that c-NHEJ is mainly employed in DSB repair in case of dry-seed irradiation, while alt-EJ is mainly employed in case of seedling irradiation (Fig. 1). This study suggests for the first time that the physiological status of irradiated materials affect the choice of DSB repair pathways in plants.

Isolation and characterization of high-temperature-tolerant mutants of *Bradyrhizobium diazoefficiens*

Application of biofertilizers has attracted attention because of the heightened interest in sustainable agriculture. *B. diazoefficiens* is one of the microbial inoculants for biofertilizer, however it is sensitive to temperature increase and their viability and functions could be constrained. In this study, wild-type cells of *B. diazoefficiens* were mutagenized with 220-MeV carbon ions to obtain high-temperature-tolerant mutants. After a three-day heat-shock treatment at 43°C, two mutant strains, designated M10 and M14, were obtained. M14 showed superior growth than M10 at 36°C, at which temperature the wild-type cells grow extremely slowly. In contrast, M14 grew more slowly compared to both M10 and wild type at 32°C. Whole-genome sequencing showed that M10 had 7 point mutations, whereas M14 had 8 point mutations and 1.27 Mb inversion. RNA-sequencing showed that a gene cluster associated with pyruvate metabolism was greatly downregulated in M14, probably due to the disjunction with promoter region after inversion. This was thought to be the cause of slow growth of M14 at 32°C. Thirty-one genes were upregulated in both M10 and M14 by five-fold or more. Notably, eight of 31 genes encode a transmembrane protein including porin, which reportedly confers high-temperature tolerance in *Salmonella typhimurium* and *Escherichia coli*. In addition, we confirmed that M14 retained symbiotic function with soybeans. M14 is not suitable for practical use because of its slow growth at 32°C, however these results suggest that high-temperature tolerance can be conferred by mutagenesis while maintaining the symbiotic functions.

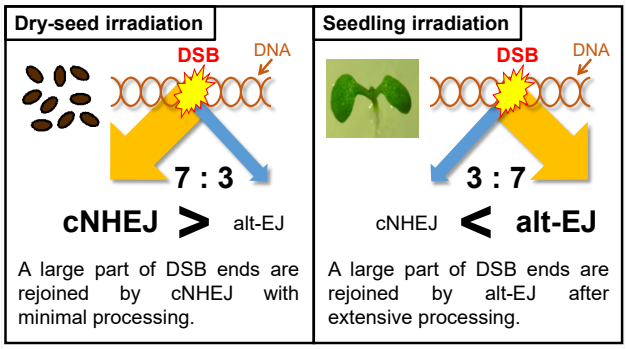

Fig. 1 DSB repair pathways mainly employed in case of dry-seed irradiation and seedling irradiation.

References

[1] S. Kitamura *et al.*, Plant J. **120**, 445 (2024). DOI: 10.1111/tpj.16955

[2] K. Satoh *et al.*, Microorganisms **12**, 1819 (2024). DOI: 10.3390/microorganisms12091819

P3-3 Medical Radioisotope Application Project

Leader : ISHIOKA Noriko

URL: https://www.qst.go.jp/site/medical-ri-application/

Based on various RI manufacturing technologies using quantum beams, we develop basic technologies that contribute to the development of radiopharmaceuticals useful for the diagnosis and treatment of diseases. Our research mainly focuses on the production of the novel RI, development of the novel radiolabeling method, elucidation of the key mechanisms that maximize the therapeutic effect of radiation, and the development of new RI compounds that enhances the cell-killing effect by simultaneously irradiating multiple targets.

Development of Copper-Mediated Astatination of Boronic Acid Precursors.

Targeted alpha therapy (TAT) has emerged as a powerful strategy in nuclear medicine, capitalizing on the high linear energy transfer (LET) of alpha particles, which induce irreparable DNA damage in cancer cells. Among alpha emitters, astatine-211 (^{211}At) is particularly attractive because of its suitable half-life (7.2 h), availability through cyclotron production using inexpensive bismuth targets, and so on. Astatine exhibits chemical properties similar to those of iodine, enabling adaptation of established iodination methods for radiopharmaceutical development. However, conventional astatination via electrophilic destannylation presents major limitations, including toxicity of organotin precursors, poor chemical stability, and reduced radiochemical yields (RCYs) under high radiation doses. To overcome these drawbacks, copper (Cu)-mediated radiohalogenation using boronic acid precursors has been developed for bromine-77 and iodine-125. The present study applies this strategy to ^{211}At, focusing on the synthesis of prostate-specific membrane antigen (PSMA) inhibitors, which are promising therapeutic agents for prostate cancer.

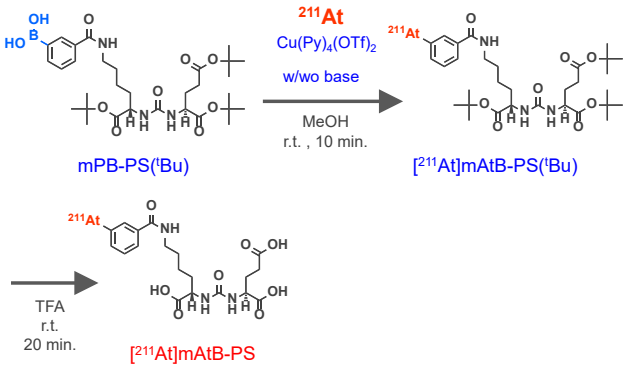

Fig. 1 Synthetic Scheme of ^{211}At labeled PSMA inhibitor

Synthetic scheme was shown in Fig. 1. A boronic acid precursor protected with *tert*-butoxycarbonyl (^{t}Bu) groups was employed and two approaches were investigated in this study; (1) Evaluation of RCYs in the presence or absence of basic salts (NaOH and K_2CO_3); (2) Cu-mediated astatination of the precursor, followed by acidic deprotection. The products were characterized using radio-HPLC in comparison with radioiodinated corresponding PSMA inhibitors. Furthermore, uptake studies were also employed in PSMA-positive and PSMA-negative cell lines as part of the compound characterization.

The astatination step was strongly influenced by reaction conditions. With NaOH, RCYs were low (22.0–31.9%, Entry 1 in Table 1), suggesting the formation of less reactive astatine species. Compensation occurred during the acidic deprotection step, leading to acceptable overall yields. - With K_2CO_3, significantly higher RCYs (69.0–82.3%, Entry 2) were obtained, attributed to stabilization of nucleophilic astatide (At^-). Without base, intermediate RCYs (60.1%, Entry 3) were achieved. However, the study revealed that [^{211}At]mAtB-PS was synthesized in high overall RCYs (64.4–87.3%), demonstrating the feasibility of Cu-mediated astatination for therapeutic radiopharmaceutical development. The uptake study showed that [^{211}At]mAtB-PS selectively accumulated in PSMA-positive LNCap.FGC cells, while uptake in PSMA-negative PC-3 cells was negligible (data not shown), which indicated that ^{211}At labeled PSMA inhibitor was successfully synthesized in this study.

Table 1
RCYs of Cu-mediated astatination under basic salt condition and (2) overall RCYs.

Entry	Base	RCY in (1)	RCY in (2)
1	NaOH	22.0–31.9	64.4–70.0
2	K_2CO_3	69.0–82.3	72.3–87.3
3	None	60.1	76.4–83.2

The results suggest two distinct mechanistic contributions; Cu-mediated astatination under basic conditions, producing At^- intermediates (especially in K_2CO_3) and electrophilic deboronation during acidic deprotection, which compensates for poor yields in the astatination step under certain conditions (e.g., NaOH or no base). These mechanisms enable satisfactory overall RCYs even when the initial astatination efficiency is limited. Importantly, the method avoids the drawbacks associated with organotin precursors, offering a safer and more stable synthetic route. The data also suggest broad applicability of Cu-mediated astatination to other radiopharmaceuticals beyond PSMA inhibitors.

References

[1] S. Watanabe *et al*., Tetrahedron **156**, 133920 (2024). DOI:10.1016/j.tet.2024.133920

P3-4 Quantum-Applied Biotechnology Project

Leader : SUZUKI Michiyo
URL: https://www.qst.go.jp/site/qabiotech/

The 'Quantum-Applied Biotechnology Project' involves researching and developing quantum biotechnology, which will lay the foundations for future advancements in this field. This work is being carried out using the quantum beam facilities at TIAQS. Specifically, we are focusing on incubating and refining the numerous quantum biotechnology 'seeds' created in life science research using quantum beams, particularly in relation to the nematode *Caenorhabditis elegans*. Our ultimate goal is to create technology that is truly 'usable'.

Advances in targeted microbeam irradiation methods for live *Caenorhabditis elegans* [1]

Our project has developed microbeam irradiation technology that uses heavy ions. This technology is now widely used to analyze the effects of radiation on mammalian cancer cells, particularly the bystander effect. During the 2000s, the scope of irradiation expanded from cells to whole animals.

In 2006, the former laboratory of our project successfully conducted the world's first microbeam irradiation of live *C. elegans* using the collimated heavy ion microbeam local irradiation system at TIARA [2]. As shown in Table 1, microbeam irradiation of live *C. elegans* using protons has since been achieved at four sites worldwide: the USA, China, and France. Teams in the USA and China achieved this by the early 2010s, but have not reported any new findings since then. Two French teams, from the University of Bordeaux and IRSN (now ASNR), began working on microbeam irradiation in the late 2010s and achieved the irradiation of live *C. elegans*.

With 302 of its 959 somatic cells being neurons, the nematode *C. elegans* is a highly useful model for analyzing the nervous system. We are investigating the effects of irradiation targeting only the central nervous system (CNS) on biological functions. Our QST facility is unique in its ability to irradiate live *C. elegans* with beams of various diameters and deliver heavy-ion irradiation (see Figure 1). The other four global teams are unable to perform single-cell or tissue-shaped irradiation on live *C. elegans*.

In order to investigate behavior immediately after irradiation, we have developed a on-chip immobilization method for *C. elegans* that inhibits movement during irradiation without anaesthetizing the animals [3]. This technique is becoming essential for microbeam irradiation intended to analyze neural functions in irradiated animals. This is evidenced by attempts by a French team to adopt it.

Experiments using accelerators offer limited opportunities and require long periods to obtain quantitative data. Therefore, it is crucial to share globally applicable technologies, reduce the development costs and timelines of irradiation techniques and biological experimental systems, and establish a framework that enables significant biological experiments to be executed more efficiently. This includes the need for the international standardisation of microbeam biological irradiation technology, as well as strengthening international collaboration in this area.

As pioneers in the field of microbeam irradiation of live *C. elegans*, we are accelerating our efforts towards the international standardisation of *C. elegans* microbeam irradiation technology. Specifically, through the European accelerator network project PIANOFORTE, we are fostering close collaboration with teams such as the Portuguese team, which is commencing microbeam biology studies, and the French team.

Table 1
Overview of live *C. elegans* irradiation with microbeams.

Country	Research Institution	Facility	Ion	Publication Year		
Japan	**JAEA**	**Collimated microbeam device of TIARA**	**$^{12}C^{5+}$**	**2006**		
U.S.A	Columbia Univ.	RARAF microbeam	H^+	2009	2013	
China	CAS-LIBB	CPM at the AIFIRA facility	H^+	2013	2016	
Japan	**QST**	**Collimated microbeam device of TIARA**	**$^{12}C^{5+}$**	**2017**	**2020**	**2021**
France	CNRS/IN2P3 and The Univ. of Bordeaux	CPM at the AIFIRA facility	H^+	2019	2023	
Japan	**QST**	**Focused microbeam device of TIARA**	**$^{12}C^{6+}$**	**2020**	**2023**	
France	IRSN	MIRCOM facility	H^+	2023		

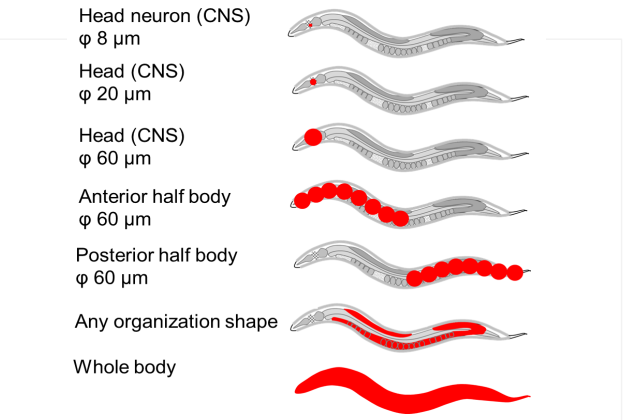

Fig. 1 Body regions irradiated with microbeams on live *C. elegans* at TIARA. Red area represents irradiated region.

References

[1] M. Suzuki, Biology **13**, 864 (2024).
DOI: 10.3390/biology13110864
[2] T. Sugimoto *et al.*, Int. J. Radiat. Biol. **82**, 31 (2006).
DOI: 10.1080/09553000600577821
[3] M. Suzuki *et al.*, J. Neurosci. Methods **306**, 32 (2018).
DOI: 10.1016/j.jneumeth.2018.05.025

P4-1 Beam Engineering Section

Leader : ISHII Yasuyuki
URL: https://www.qst.go.jp/site/beam-engineering-e/

The research objectives in our section are the development of various accelerator-related techniques including beam-irradiation-techniques and beam-analyses. Each member has been engaged in individual research more than one. Recent remarkable study is “Upgrade of Hevey Ion Microbeam System”.

Upgrade of Hevey Ion Microbeam System

The Heavy ion microbeam system (H-MB), operational for about 30 years, was TIARA’s inaugural ion microbeam system equipped with a double quadruple magnet configuration (doublet). The H-MB was used a lot of studies, specifically which could produce a single-ion for studies of the single event upset for semiconductors. This upgrade involved a near-total replacement of the H-MB components to achieve submicron ion beam capabilities. Initially, the H-MB offered demagnification of 4.6 and 28 along the x- and y- axes, respectively, producing a 1 x 1 μm^2 H-MB. However, the aging infrastructure resulted in reduced beam current and inability to maintain microbeam sizes. Critical applications, such as the fabrication of Nitrogen Vacancy Centers, necessitate submicron ion beams to induce quantum effects, prompting a comprehensive overhaul of the H-MB.

The demagnification of the H-MB was inadequate for generating submicron ion beams. This redevelopment aimed to achieve submicron beam formation without requiring a vibration insulating mount, as illustrated in Fig.1.

The upgrade system incorporates a series of focusing lenses composed of four quadrupole magnets mounted on a linear stage. This configuration allows for various combinations of magnets, such as a doublet, a triplet, and two-stage double magnets with separate doublets, to be structured based on experimental requirements.

Magnet positioning was optimized through numerical simulations using the ion microbeam trajectory code. Calculations were performed for both doublet and a triplet configuration under the following conditions: ion species Si^{4+}, beam energy 15 MeV, object sizes 25.0 × 10.0 and 25.0 × 5.0 μm^2 for the doublet and the triplet, respectively. These results indicate that those spot sizes are almost same, thereby aberration effects are small for the doublet. The minimum beam sizes achieved with double and triple magnet configurations are 470 × 520 nm^2 and 403 × 458 nm^2, respectively with a consistent working distance of 280 mm and 320 fort the doublet and the triplet, respectively. The demagnifications for the doublet and the triplet are 62 and 2.6 on the x- and y- axes, and 32 and 172 on the x- and y- axes, respectively. The enhanced demagnifications for both magnet configurations are attributed to the elongation of the object length from 3.8 m to 6 m, spanning form the object slits to the magnets.

In Fig.1 downstream of the quadrupole magnets, a beam scanner and a vacuum chamber have been positioned. The beam scanner, comprising two pairs of electrostatic parallel plates for the x- and y-axes, allows scanning over 500 × 500 μm^2 area. The vacuum chamber, connected to a turbo molecular vacuum pump, houses the irradiation sample and a Cu mash, enabling simultaneous beam size evaluation and irradiation by moving the sample and mesh relative to each other.

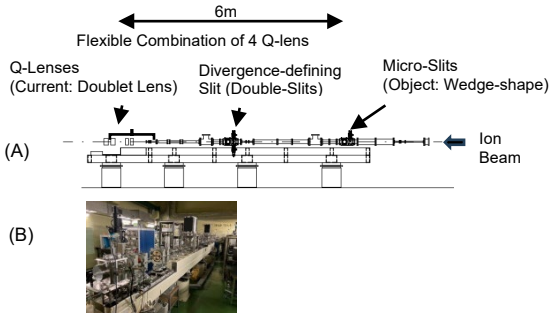

Fig.1 Schematics of H-MB and a photograph. (A) is Schematic of the upgraded H-MB with component parts. (B) is the photograph of H-MB.

As shown in Fig. 2, an ion microbeam device control system developed by Tohoku University and adapted for this project was installed in the H-MB. This system enables beam focusing by adjusting the divergence-defining slit and magnetic lens and the strengths through varying electric coil currents, thereby determining the beam size.

In Fig. 2, the control system facilitates automatic ion beam focusing by manipulating the electric coil currents of the magnets based on the analysis of secondary electron image emitted from a Cu mesh during ion beam irradiation and enhancing the clarity of the control system’s display image.

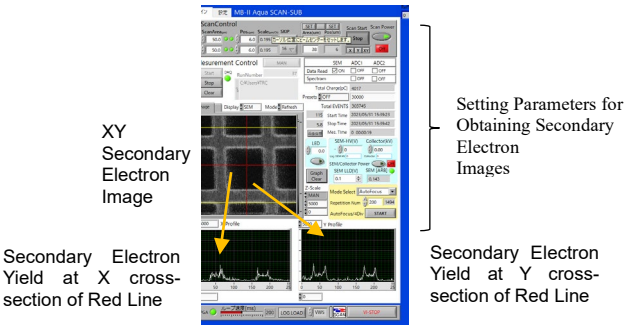

Fig. 2 The picture of display when the auto beam focusing system is worked. The red cross-lines in XY secondary electron image shows the electron yields at X and Y cross-sections of red cross-lines.

References

[1] Y. Ishii *et al*. Nucl. Instr. Meth. in Phy. B **557**, 165539 (2024). doi: 10.1016/j.nimb.2024.165539

Part II

1 - 01 Synthesis of graphene-based materials using high-energy ion irradiation

S. Entani [a)], M. Honda [b)] and M. Kohda [a,c)]

[a)] Quantum Materials and Applications Research Center, QST
[b)] Honda's Lab for Development of Future Clay Materials Reserach, JAEA
[c)]School of Engineering, Tohoku University

Introduction

Heteroatom doping in graphene has attracted significant interest as a strategy to tune its electronic, physical, and chemical properties. For practical applications of doped graphene, it is crucial to employ large-area films with a well-controlled number of layers. Thus, a method enabling direct heteroatom doping into CVD-grown large-area graphene films is highly desirable. While extensive research has been conducted on the synthesis and characterization of graphene hydrides (graphane) and fluorographene, reports on graphene functionalized with heavier halogens, such as bromine and iodine, remain scarce due to their chemical instability. In this study, we demonstrate the doping of Br atoms into CVD-grown graphene via high-energy ion irradiation, using a KBr/graphene/Si heterostructure [1].

Experimental

Graphene was synthesized on polycrystalline copper foil via thermal CVD and transferred onto a Si(100) substrate by etching the copper with $FeCl_3$ solution [2]. A 100 nm-thick KBr film was then deposited on the graphene surface at room temperature in an ultrahigh vacuum chamber. The sample was irradiated with 9.0 MeV Ni^{2+} ions at Takasaki Ion Accelerators for Advanced Radiation Application (TIARA), with fluence ranging from 10^{13} to 10^{16} ions·cm^{-2}, all at room temperature. After the irradiation, the KBr over layer was removed by water-rinsing. The atomic and electronic structure of ion-irradiated KBr/graphene/Si were characterized using Raman spectroscopy, X-ray absorption fine structure (XAFS) and X-ray photoelectron spectroscopy (XPS). XAFS measurements were performed at the BL-27B station of KEK-PF.

Results and Discussion

Figure 1 shows the core level XPS spectra of C 1*s* and B 3*d* for KBr/graphene/Si samples irradiated with ion fluences of 10^{15} and 10^{16} ions·cm^{-2}. It is important to emphasize that no detectable signal corresponding to Br 3*d* was observed at ion fluences of 10^{14} or lower, indicating that bromine doping into graphene does not occur significantly at these lower fluences. At the ion fluence of 10^{16} ions·cm^{-2}, quantitative analysis based on the peak intensity ratio between C 1*s* and Br 3*d* reveals that ion irradiation induces bromine doping in graphene at a concentration of approximately 3.7 ± 0.8 atom%. This doping level is notably lower than that of chlorin (10.2 atom%), which has been previously achieved through high-energy ion irradiation techniques [1]. The reduced bromine doping may be attributed to steric hindrance effects associated with the large atomic radius or bonding characteristics of bromine compared to chlorine. In the C 1*s* spectrum corresponding to the 10^{16} ions·cm^{-2} irradiation condition, a prominent peak appears at 285.3 eV, which is consistent with the presence of sp^3-hybridized carbon atoms [1]. Furthermore, a broad spectral feature is observed around 288 eV, which can be assigned to oxidized carbon species such as carbonyl groups and also to the formation of C-Br bonds [3]. In the Br 3*d* spectra shown in Fig. 1 (b), the main peak at 70.2 eV is accompanied by a shoulder at approximately 68.5 eV. The dominant peak is attributed to the formation of covalent Br-C bonds, while the shoulder structure may originate from Br-Si interactions and/or the presence of bromine anions [3]. Taking into account complementary analyses performed using XAFS and Raman spectroscopy, we conclude that high-energy ion irradiation of KBr/graphene/Si effectively facilitates the formation of C-Br bonds. These findings suggest that ion-irradiation is a promising and versatile method for the controlled synthesis of novel graphene-based compounds with tailored chemical functionalities, it holds potential for the fabrication of large-area films of graphene compounds.

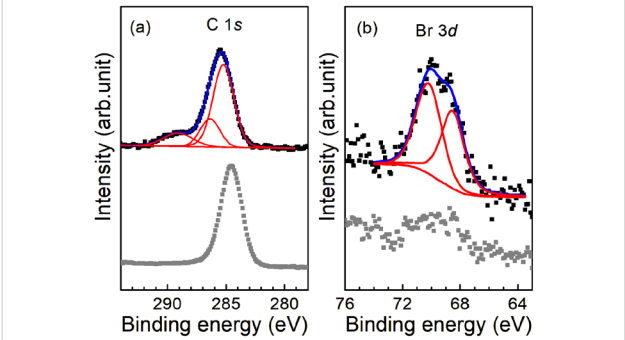

Fig. 1 Core level (a) C 1*s* and (b) Br 3*d* XPS spectra of 10^{16} and 10^{15} ions·cm^{-2} irradiated KBr/graphene/Si (black and gray). Blue and red lines are fitted and separated spectra.

References

[1] S. Entani *et al.*, RSC Adv. **6**, 68525 (2016). DOI: 10.1039/c6ra09631j, S. Entani *et al.*, ACS Omega **10**, 21537 (2025). DOI: 10.1021/acsomega.5c00580
[2] S. Entani *et al.*, Surf. Sci. **704**, 121749 (2021). DOI: 10.1016/j.susc.2020.121749
[3] X.-L. Zhou, *et al.*, Surf. Sci. **219**, 294 (1989). DOI: 10.1016/0039-6028(89)90214-8

1 - 02 Columnar excitation fluorescence microscope for accurate evaluation of quantum properties of NV centers in millimeter-scale diamonds

Y. Masuyama [a)], C. Shinei [b, d)], H. Abe [a)], M. Miyakawa [c)], T. Taniguchi [c)] and T. Teraji [b)]

[a)] Quantum Materials and Applications Research Center, QST
[b)] Research Center for Electronic and Optical Materials, NIMS
[c)] Research Center for Materials Nanoarchitectonics, NIMS
[d)] Department of Applied Physics, University of Tsukuba

Introduction

Diamond quantum sensors are expected to become highly sensitive sensors that have the potential to change fields from biomagnetism to materials science dramatically. Their excellent quantum properties at room temperature and atmospheric pressure enable their high sensitivity. However, achieving femtotesla-level sensitivity requires large, uniform, high-quality diamond crystals with superior quantum properties, such as long coherence times [1]. A major bottleneck in developing such materials has been the lack of an appropriate evaluation methodology. To address this challenge, we have developed a new microscopy system, the Columnar Excitation Fluorescence Microscope (CEFM) [2]. This system is specifically designed for the rapid and accurate evaluation of the spatial distribution of quantum properties across entire bulk diamond samples, thereby accelerating the feedback loop for material synthesis and sensor development.

Experimental

CEFM uses an objective lens with a long Rayleigh length to match the sample's thickness to maximize the fluorescence signal from spin-polarized NV centers [Fig. 1]. The lens for CEFM creates a uniform, columnar excitation volume (approximately 20 μm in diameter, 500 μm along the sample thickness) that efficiently excites a large number of NV centers, significantly improving the signal-to-noise ratio. This enhancement allows the CEFM setup to perform rapid quantum property evaluations, such as coherence time measurements (T_2, T_2*), across an entire millimeter-scale diamond by scanning the sample stage. The sample used for the measurements was a {111}-oriented, ^{12}C isotopically enriched diamond crystal made by the high-pressure, high-temperature (HPHT) method [3]. The NV centers in the diamond were uniformly created at a concentration of approximately 0.5 ppb by irradiation of a 2 MeV electron beam, followed by a high-temperature annealing process in a vacuum.

Results and Discussion

We performed a spatial distribution evaluation of quantum properties over a wide area of the diamond sample. Figure 1 (b) shows the spatial distribution of the Rabi contrast over a 1 mm × 1 mm area. The Rabi contrast is an index of the efficiency of quantum state manipulation and a critical parameter of the sensor's magnetic sensitivity. Our measurements confirmed that the Rabi contrast was high and uniform over a large area, demonstrating that high-quality, uniform quantum manipulation is possible for this sample. The CEFM is also possible to perform comprehensively and quantitatively map multiple quantum properties (T_1, T_2, T_2*) on a millimeter scale. It achieved wide-area quality evaluation, a task difficult for conventional methods, in a practical amount of time. The rapid feedback provided by CEFM will accelerate the optimization of material synthesis processes and become an indispensable foundational technology for the development of future ultra-sensitive diamond quantum sensors.

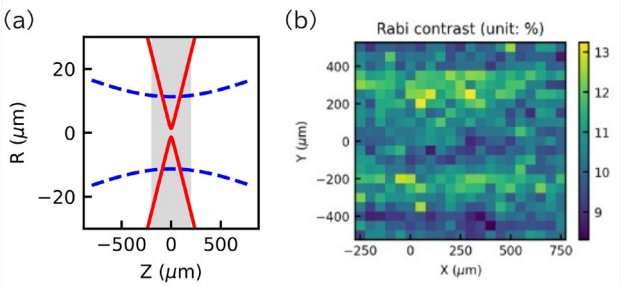

Fig. 1 (a) Laser beam shape along the optical axis of the CEFM objective lens (dashed line) and the confocal microscope objective lens (solid line). The gray area indicates the typical thickness of a diamond sample. Note that the R and Z scales are different. (b) Spatial distribution of the Rabi contrast measured over a millimeter-scale area of the diamond sample.

Acknowledgments

This work was supported by MEXT Q-LEAP (JPMXS0118067395 and JPMXS0118068379). YM acknowledges the support of JSPS KAKENHI (JP24K169972). T.T. acknowledges the support of JST Moonshot R&D (JPMJMS2062), MIC R&D for construction of a global quantum cryptography network.

References

[1] J. F. Barry *et al.*, Rev. Mod. Phys. **92**, 015004 (2020). DOI: 10.1103/RevModPhys.92.015004
[2] Y. Masuyama *et al.*, Sci. Rep. **14**, 18135 (2024). DOI: 10.1038/s41598-024-68610-5
[3] M. Miyakawa *et al.*, Jpn. J. Appl. Phys. **61**, 045507 (2022). DOI: 10.35848/1347-4065/ac5d7f

1 - 03 Light soaking recovery of proton-irradiated CIGSSe solar cells

T. Nakamura [a)], H. Sugimoto[b)], T. Yagioka [b)], Y. Murakami [a)], T. Aihara [a)], T. Okumura[a)], S.-I. Sato[c)] and T. Oshima[c)]

[a)] Research and Development Directorate, JAXA,
[b)] PXP Corporation,
[c)] Quantum Materials and Applications Research Center, QST

Chalcopyrite Cu(In, Ga)(Se, S)$_2$ (CIGSSe) solar cells have been known to have strong radiation hardness. Almost no degradation has been observed against electron irradiation up to a fluence of 10^{16} cm^{-2}. However, with regard to proton irradiation, conventional CIGSSe solar cells generally exhibit significant degradation due to severe defect introduction caused by the proton irradiation. Recently, proton degradation-free CIGSSe solar cells without cover glass and adhesive have been reported by using remarkable CIGSSe absorber layer with Ga-less and Cu-poor compositions in the depletion layer [1]. This full-recovery characteristic is considered to be delivered from the passivation of the antisite defects, such as In$_{Cu}$ and Ga$_{Cu}$ defects, by the thermally migrated V$_{Cu}$ as well as the restriction of Ga$_{Cu}$ defects by the Ga-less composition. However, previous studies have shown that the full-recovery from the proton-induced degradation was only observed under the condition of the heat light soaking (LS) at 150°C. To determine whether the LS recovery is possible under realistic operating conditions in space, we investigate the temperature dependence of LS recovery [2]. In addition, the spectrum dependence of LS recovery investigated by using GaAs wafers as optical filters, which was supposed to the multijunction solar cells with the GaAs-based top cells and the CIGSSe bottom cells.

The CIGSSe solar cells were irradiated with protons at TIARA/QST. Fig 1 shows remaining factors of conversion efficiency (Eff), open-circuit voltage (V$_{oc}$) and short-circuit current (J$_{sc}$) after 300 keV proton irradiation with a fluence of 10^{13} cm^{-2} as a function of LS time at temperatures of 80°C, 100°C and 150°C, respectively. Circle and cross marks show without and with GaAs filter, respectively. Although the samples showed significant degradation immediately after irradiation, all electrical parameters were subsequently recovered by the heat LS. Especially, the J$_{sc}$ of all samples was completely recovered within just 4 hours under the heat LS from 80°C to 150°C, whereas V$_{oc}$ and FF recovered relatively slowly. Though lower temperature LS showed lower annealing rate, comparable annealing effect was obtained even at the lower temperature over a long period of time. Regarding spectrum dependence, the GaAs-filtered samples also showed the comparable annealing effect, however, the annealing rate was slightly slow. These results indicate that the LS recovery is available even in the actual operating conditions and for multijunction solar cells.

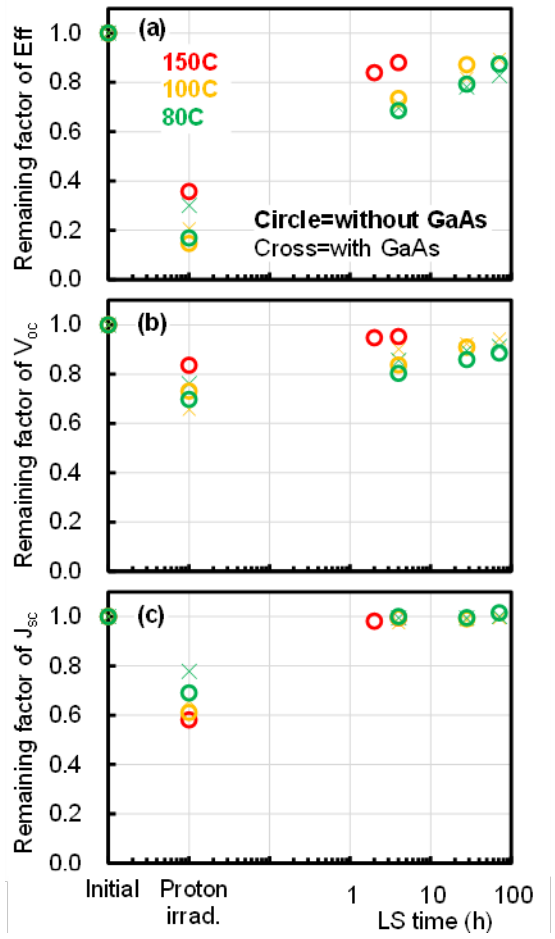

Fig. 1 Remaining factor of (a) Eff, (b) V$_{oc}$ and (c) J$_{sc}$ after 300keV proton irradiation with a fluence of 1 x 10^{13} cm^{-2} as a function of LS time at temperatures of 80C (green), 100C (orange) and 150C (red), respectively. Circle and cross marks show without and with GaAs filter, respectively.

Acknowledgments

The authors thank the kind assistance of R. Tanaka and Y. Mori of the AES Corporation.

References

[1] H. Sugimoto *et al.*, IEEE 50th PVSC, pp. 1-4 (2023). DOI: 10.1109/PVSC48320.2023.10359816.
[2] H. Sugimoto *et al.*, IEEE 52nd PVSC, pp. 1659-1663 (2024). DOI: 10.1109/PVSC57443.2024.10749255.

1 - 04 Quantum orbital-state control of a neutral nitrogen-vacancy center at millikelvin temperatures

H. Kurokawa [a)], S.Nakazato [b)], T. Makino [a,c)], H. Kato [a,c)], K. Takenaka [d)], S. Onoda [a,d)], Y. Sekiguchi [a)], and H. Kosaka [a,b)]

[a)]Quantum Information Research Center, Institute of Advanced Sciences, Yokohama National University
[b)]Department of Physics, Graduate School of Engineering Science, Yokohama National University
[c)]Advanced Power Electronics Research Center, AIST
[d)]Quantum Materials and Applications Research Center, QST

Introduction

Color centers in diamond are leading platforms for quantum sensing, photonics, and quantum networking. While the negatively charged NV^- center is standard, the neutral NV^0 offers a powerful advantage: a ground-state orbital doublet with ~10 GHz splitting and a vastly larger electric-field susceptibility, making it attractive for microwave control and cavity QED. At a few kelvin, however, phonon-assisted orbital relaxation is rapid and has limited coherence and coherent control [1]. This paper [2] demonstrates quantum control of a single NV^0 at millikelvin temperatures, quantifies the suppression of phonon-induced relaxation, and extends orbital coherence via dynamical decoupling. These results position NV^0 as an optically addressable defect suitable for microwave cavity QED and for hybrid interfaces bridging microwave photons, phonons, and optical photons in future quantum networks.

Experimental

Experiments were performed using a confocal microscope integrated with a dilution refrigerator (mixing-chamber temperature of ~15 mK). For sample preparation, the diamond was irradiated with an electron beam (2 MeV, 1e14/cm2), followed by annealing (1000 ◦C, 2h) to increase the density of NV centers. A 10-μm solid-immersion lens on the surface improved photon-collection efficiency. Patterned Au/Ti electrodes were used to apply microwave electric fields to NV^0. A 637-nm laser pulse initialized the charge state to the NV^0 state. Photoluminescence-excitation spectroscopy at 575 nm identified the two optical transitions from the orbital ground states, whose separation yielded the ground-state splitting $\Delta_{gs} \approx 13$ GHz. Microwave pulses were applied to observe optically detected electrical resonance, Rabi oscillations, and Ramsey interference.

Results and Discussion

Cooling to millikelvin temperatures dramatically suppresses phonon-assisted orbital relaxation. The orbital T_1 increases from ~150 ns at ~8 K to ~4.7 μs at ~10–15 mK, consistent with a single-phonon process. Microwave driving produces clear Rabi oscillations with maximum Rabi frequency around a few-tens of megahertz and a decay time T_2^{Rabi} ~ 46 ns. Ramsey measurements yield T_2^* ~ 54 ns at millikelvin temperatures, which is only modestly larger than at a few kelvin. Applying dynamical decoupling

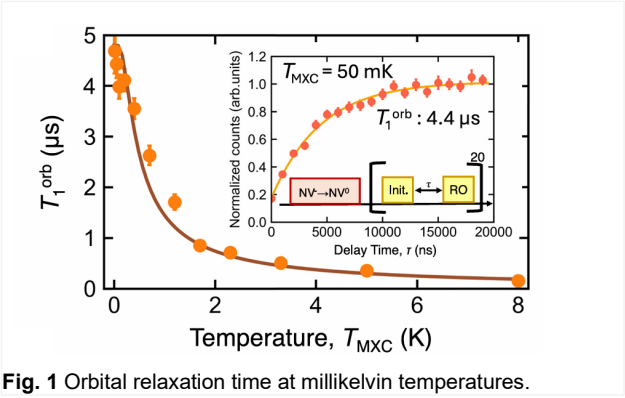

Fig. 1 Orbital relaxation time at millikelvin temperatures.

substantially extends coherence: Hahn-echo gives T_2^{echo} ~ 1.6 μs, and CPMG pushes T_2 up to ~2.0 μs, representing more than a 30× enhancement over T_2^*. The improvement saturates as pulse number increases because microwave-induced heating shortens T_1 toward ~1.3–1.8 μs, ultimately capping echo times near the $2T_1$ limit. This indicates that residual dephasing at millikelvin temperatures is dominated by low-frequency, non-Markovian noise such as spectral diffusion rather than thermal phonons alone. Using these measured parameters, we estimate strong coupling between a single NV^0 and a high-impedance superconducting resonator. These results open a path to microwave cavity QED with an optically readable single defect and suggest hybrid, phonon-assisted interfaces linking microwave and optical domains.

Acknowledgments

H. Kosaka acknowledges the funding support from Japan Science and Technology Agency (JST) Moonshot R&D Grant No. JPMJMS2062 and JST CREST Grant No. JPMJCR1773. H. Kosaka also acknowledges the Ministry of Internal Affairs and Communications (MIC) for funding, research and development for construction of global quantum cryptography network (JPMI00316), and the Japan Society for the Promotion of Science (JSPS) Grants-in-Aid for Scientific Research (20H05661, 20K20441).

References

[1] H. Kurokawa *et al.*, Nat. Commun. **15**, 4039 (2024). DOI: 10.1038/s41467-024-47973-3
[2] H. Kurokawa *et al.*, Phys. Rev. Lett. **135**, 016902 (2025). DOI: 10.1103/m1qx-xlpd

1 - 05 Physics-based ion track structure model for Single-Event Effect simulations on SiC power devices

M. Iwata [a)], S. Kuboyama [b)], A. Michez [c)], A. Makihara [b)], M. Takahashi [a)], N. Nemoto [a)], M. Midorikawa [b)], J. Boch [c)], F. Saigné [c)], F. Wrobel [c)], T. Makino [d)], T. Ohshima [d)], and H. Shindou [a)]

[a)] Japan Aerospace Exploration Agency (JAXA)
[b)] High-Reliability Engineering & Components Corporation (HIREC)
[c)] Institut d'Electronique et des Systèmes, UMR-CNRS
[d)] Quantum Materials and Applications Research Center, QST

Introduction

Silicon carbide (SiC) devices are not only promising candidates for space applications due to their excellent performance but also attract strong interest as potential platforms for quantum devices. For both quantum applications and practical use in space systems, the reliability of SiC technology is of paramount importance. In particular, it is essential to understand the physics of single-event effects (SEEs) in SiC devices in detail to ensure their reliability. However, SiC devices exhibit high susceptibility to heavy ions, which induces abnormal charge collection, leakage current, and destructive single-event burnout (SEB) [1,2]. The underlying mechanisms remain insufficiently understood, as conventional device simulation models cannot fully account for these phenomena. To address this issue, this study aims to establish a physics-based ion track structure model that enhances the accuracy of single-event effect simulations in power devices.

Experimental

Geant4 simulations with the MicroElec extension were performed to evaluate radial dose distributions, enabling the tracking of low-energy electrons down to 16.7 eV [3]. From these results, a power-law radial profile was derived, eliminating the need for arbitrary fitting parameters. A composite model was then developed to overcome numerical instabilities near the track core. The model was implemented in the ECORCE device simulator [4] and calibrated against experimental data obtained from SiC Schottky barrier diodes (SBDs) and junction barrier Schottky (JBS) diodes under low bias conditions.

Results and Discussion

The proposed composite model successfully reproduced the experimental charge collection behavior, including the saturation trend observed at high LET values, a feature that conventional Gaussian models failed to capture. This saturation was attributed to Auger recombination, consistent with phenomena previously reported in Si, SiC, and diamond devices. Furthermore, both 600 V SBDs and 1200 V JBS diodes were accurately reproduced using the same parameter set, demonstrating the robustness and versatility of the model.

Conclusion

A physics-based ion track structure model for power device simulations has thus been developed and validated. Compared with conventional Gaussian models, it provides improved quantitative accuracy in predicting ion-induced effects. Future studies will aim to refine the model for devices with thick epitaxial layers and for higher LET regimes, thereby further enhancing its predictive capability.

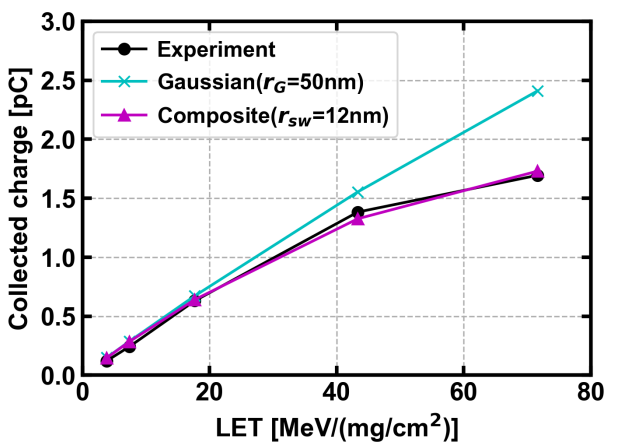

Fig. 1 Comparison of experimental and simulated collected charge in a 600 V SiC SBD under reverse bias. The composite model reproduces the saturation trend, while the Gaussian model overestimates charge collection.

References

[1] S. Kuboyama *et al.*, IEEE Trans. Nucl. Sci., **53**, no. 6, pp. 3343–3348, Dec. 2006. DOI: 10.1109/TNS.2006.885165
[2] A. F. Witulski *et al.*, IEEE Trans. Nucl. Sci., **65**, no. 1, pp. 256–261, Jan. 2018. DOI: 10.1109/TNS.2017.2782227
[3] M. Raine *et al.*, IEEE Trans. Nucl. Sci., **57**, no. 4, pp. 1892–1899, Aug. 2010. DOI: 10.1109/TNS.2010.2048926
[4] A. Michez *et al.*, IEEE Trans. Nucl. Sci., **62**, no. 4, pp. 1516–1527, Aug. 2015. DOI: 10.1109/TNS.2015.2449281

2 - 01 Solvent extraction of astatine by DIPE and attempt to identify the extracted species by thin layer chromatography

T. Taniguchi [a], S. Maruyama [a], K. Aoi [a], Y. Nagai [a], K. Washiyama [b], I. Nishinaka [c], Y. Wang [d], H. Haba [d] and A. Yokoyama [e]

[a] Graduate School of Natural Science and Technology, Kanazawa University
[b] Advanced Clinical Research Center, Fukushima Medical University
[c] Department of Quantum-Applied Biosciences, QST
[d] Nishina Center for Accelerator-Based Science, RIKEN
[e] Institute for Science and Engineering, Kanazawa University

Introduction

Among various α emitters, ^{211}At is a promising nuclide expected to enable targeted α therapy for the treatment of cancer. Extraction with diisopropyl ether (DIPE) has been recognized as a method for separating At from irradiated Bi targets using an accelerator. However, the mechanism underlying its solvent extraction is still not fully understood. This study conducts experiments with the objective of improving our understanding of chemical properties of At by elucidating the extraction mechanism in the DIPE-hydrochloric acid (HCl) system [1].

Experimental

^{211}At was produced through two distinct processes: the ^{209}Bi(α,2n) reaction and the milking of ^{211}Rn generated in the ^{209}Bi(^{7}Li,5n) reaction. In the former case, the ^{209}Bi target was subjected to irradiation with 40 MeV α ions at an average current of 1.0–1.2 μA for 2–3 h, using the AVF cyclotron at the Research Center for Nuclear Physics, Osaka University, or RIKEN AVF cyclotron. In the latter case, a stack of four ^{209}Bi targets was irradiated with 60 MeV $^{7}Li^{3+}$ ions at a current of 0.15–0.2 μA for 2–3 h. using the JAEA tandem accelerator.

A dry distillation method was used for separating At from an irradiated Bi target and preparing an At solution [2].

The solvent extraction experiments employed a solution of At. HCl was added to a plastic centrifuge tube along with an At solution to adjust acid concentration. A 5 mL volume of DIPE was added and stirred for 5 min. 4 mL of each phase containing At was extracted. The concentration of At radioactivity in each phase was determined by γ-ray measurement using Ge semiconductor detector and α-ray measurement using a liquid scintillation counter.

Thin layer chromatography (TLC) was conducted for a 10 μL volume of organic phase on a 10 × 2 cm silica gel TLC plate with the mobile phase of ethanol/water (1:1, v/v). After developing and drying the plate, they were placed in contact with an imaging plate. The distributions of At radioactivity on the plates were visualized by a bioimaging analyzer (BAS-1800II).

Results and Discussion

As shown in Fig.1, solvent extraction behavior on HCl concentration remained unaffected by the presence of a reducing agent, however, distinct extraction behavior was observed at elevated concentrations of HCl with the addition of an oxidizing agent.

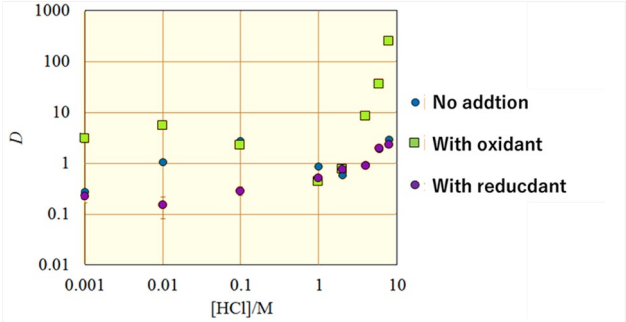

Fig. 1 At distribution ratio dependency on HCl concentration in DIEP-HCl extraction without and with addition of oxidant or reductant

Fig. 2 shows the TLC results obtained under Ar. The increase in extraction rate with HCl concentration shows good correlation with the increasing abundance of the At cationic species $(At)^{x+}$ (green bars).

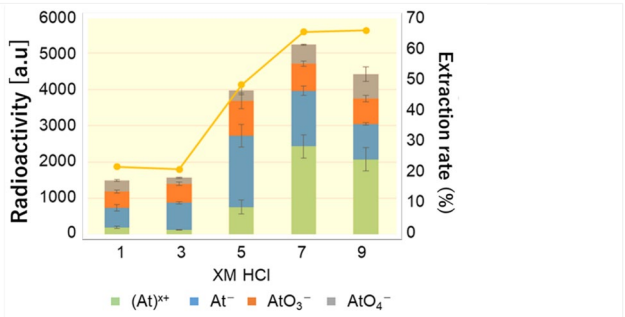

Fig. 2 Radioactivity of each chemical species in DIPE (bars) and the At extraction ratio (yellow symbol) in an Ar gas phase

Based on these findings, we proposed equations for the extraction of At in oxidized and reduced states for the extraction mechanism of At in DIPE-HCl solvent extraction.

References

[1] T. Taniguchi *et al.*, J. Radioanal. Nucl. Chem. **333**, 3937 (2024). DOI: 10.1007/s10967-024-09547-x
[2] I. Nishinaka *et al.*, J. Radioanal. Nucl. Chem. **326**, 743 (2020). DOI: 10.1007/s10967-020-07308-0

2 - 02

Utilities of ionic extraction with astatine ions and its extraction mechanism

A. Yokoyama [a)], K. Kawasaki [b)], Y. Nagai [b)], H. Tazuru [b)], Y. Shimizu [b)], K. Ganaha [b)], K. Washiyama [c)], I. Nishinaka [d)], Y. Wang [e)], X. Yin [e)], N. Sato [e)], A. Nambu [e)], Y. Shigekawa [e)], and H. Haba [e)]

[a)] College and Institute for Science and Engineering, Kanazawa University
[b)] Graduate School of Natural Science and Technology, Kanazawa University
[c)] Advanced Clinical Research Center, Fukushima Medical University
[d)] Department of Quantum-Applied Biosciences, QST
[e)] Nishina Center for Accelerator-Based Science, RIKEN

Introduction

^{211}At has garnered the greatest interest with regard to the utilization of α-radionuclides in isotope therapy. Purification for ^{211}At utilization is typically performed using solvent extraction with organic solvents in wet chemical separation. Organic solvents have the advantage of being inexpensive and readily available, but many of them are volatile and flammable, and there are concerns about environmental contamination and handling of hazardous materials. We have focused on ionic liquids (IL) as an alternative to organic solvents. This study is the first attempt on the application of IL for the extraction of ^{211}At [1].

Experimental

^{211}At was produced through two distinct processes: the ^{209}Bi(α,2n) reaction and the milking of ^{211}Rn generated in the ^{209}Bi(^{7}Li,5n) reaction. In the former case, the ^{209}Bi target was subjected to irradiation with 40 MeV α ions at an average current of about 1 μA for several hours, using the AVF cyclotron at the Research Center for Nuclear Physics, Osaka University, RIKEN AVF cyclotron, or a medium-sized cyclotron at Fukushima Medical University. In the latter case, a stack of four ^{209}Bi targets was irradiated with 60 MeV $^{7}Li^{3+}$ ions at a current of about 0.15 μA for 0.5–3 h, using the JAEA tandem accelerator.

A dry distillation method was used for separating At from an irradiated Bi target and preparing an At solution [2].

The solvent extraction behavior of At was investigated using the At solution and several ILs, namely, [C_4mim][Tf_2N], [C_6mim][Tf_2N], [C_8mim][Tf_2N], [C_8mim][PF_6], and [C_8mim][BF_4] for practical application of a ^{211}Rn–^{211}At generator from the following perspectives: 1) investigation of liquid-liquid extraction rate using IL, 2) back-extraction from ILs, 3) effects of IL species on extraction rates, 4) IL solvent extraction using ^{211}At from the decay of ^{211}Rn through wet separation process, 5) effects of oxidizing and reducing agents on back-extraction from dodecane, 6) effects of oxidizing, reducing agents, and $NaPF_6$ addition on extraction and back-extraction, 7) extraction distribution dependence on radioactivity concentration, and 8) extraction distribution dependence on dose adsorbed by extraction solvent.

Results and Discussion

As an illustrative case, the results of At extraction (from acidic aqueous phase to IL) and back-extraction (from IL to alkaline aqueous phase) using five ILs with different combinations of cations and anions are shown in Figs. 1 and 2, focusing on extraction efficiency and its dependence on the physicochemical properties of the ILs.

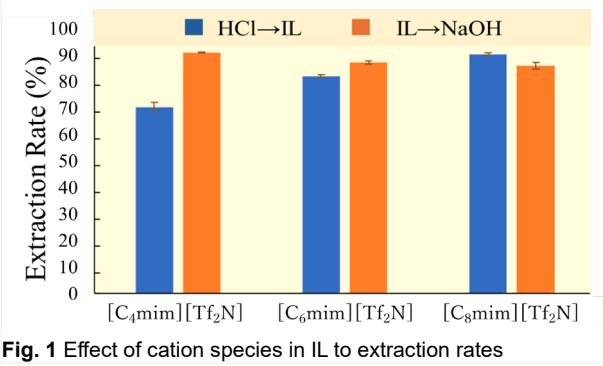

Fig. 1 Effect of cation species in IL to extraction rates

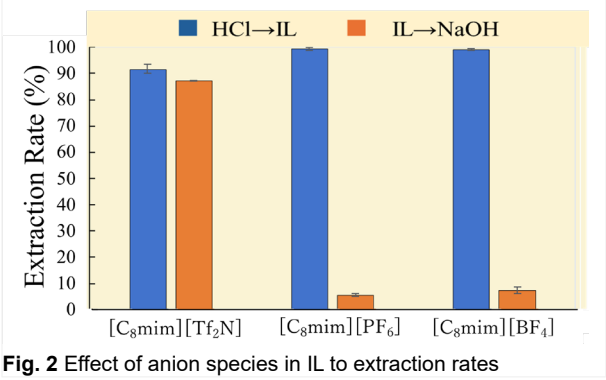

Fig. 2 Effect of anion species in IL to extraction rates

Based on the extraction rates of the IL cations (Fig. 1) and anions (Fig. 2) in At extraction and back-extraction, [C_8mim][Tf_2N] was identified as the most suitable IL for use in a ^{211}Rn–^{211}At generator.

References

[1] A. Yokoyama *et al.*, Radiochim. Acta **113**, 373 (2025). DOI: 10.1515/ract-2024-0357
[2] T. Taniguchi *et al.*, J. Radioanal. Nucl. Chem. **333**, 3937 (2024). DOI: 10.1007/s10967-024-09547-x

2 - 03 Irradiation tests of radiation-hard components and materials for ITER blanket remote handling system

M. Saito [a)], Y. Kawai [a)], K. Nakata [a)], T. Ito [a)], T. Fujiwara [a)], T. Tanaka [a)], S. Kodama [a)] Y. Noguchi [a)] and N. Takeda [a)]

[a)] Department of ITER Project, QST

Introduction

The ITER blanket remote handling system (BRHS) will replace the First Walls, which face high-temperature plasma, in a high level γ-ray radiation environment under a time constraint. To increase the availability of the system, a radiation hardness of 1 MGy is required for the BRHS components. Moreover, to improve the safety and efficiency of BRHS operations, a radiation hardness target value of 2 MGy was set for these irradiation tests. The BRHS requires many sensors for detecting position and movement limits. This report shows the irradiation test results of the contact sensors for the BRHS.

Irradiation tests

The sample contact sensors (GN-BP5MA, METROL Co., Ltd.) were irradiated at 530–1610 Gy/h up to 2 MGy in a γ-ray irradiation facility. The samples were packed in polyimide sheets, as shown in Fig. 1, to prevent contamination, such as from dust. After irradiation, the samples underwent testing, the test items of which are shown in Table 1. The samples were also disassembled to check their individual parts.

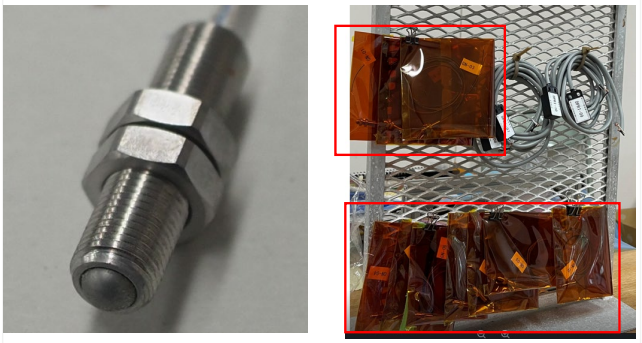

Fig. 1 The appearance of the contact sensor sample and packing appearance for irradiation

Results and Discussion

The contact sensors were irradiated up to 2 MGy. After irradiation, their functions were tested, the results of which are shown in Table 2. All samples satisfied the acceptance criteria for all test items after 1 MGy of irradiation. After 2 MGy of irradiation, however, the contact part of the sensors did not function, thus the test items could not be tested (Stroke distance was measured from the edge of the contact to the edge of the sensor body, as shown in Fig. 2.). After disassembling the samples for visual inspection, it was discovered that the sensor body and contacts had changed color. This result suggests that the contacts corroded due to irradiation and adhered to the sensor body. In our future work, the contacts of the sensors will be observed by SEM-EDS elemental analysis to identify the causes of the corrosion.

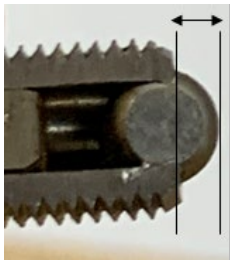

Fig. 2 Stroke measurement points (Cross section of the sensor).

Table 1
Test items for contact sensors

Test item	Criteria
Contact force	1.0N±20%
Stroke	1.0mm±0.15mm
Pretravel	0.3mm±0.1mm
Repeat accuracy	0.01mm (2 σ)
Insulation resistance test	Min 100 MΩ at DC 250 V
Disassembly and inspection	Observation

Table 2
Test results of irradiated contact sensors

Test item	1 MGy	2 MGy
Contact force	Pass	Unmeasurable
Stroke	Pass	Pass
Pretravel	Pass	Unmeasurable
Repeat accuracy	Pass	Unmeasurable
Insulation resistance test	Pass	Pass

Acknowledgments

The authors would like to acknowledge Beam Operation Co., Ltd. and the Takasaki Institute for Advanced Quantum Science's Irradiation Facilities Section who supported these irradiation experiments.

2 - 04 Development of low-viscosity silicone rubber with variable hardness for precise microfabrication

Y. Kimura [a)], K. Yoshimura [a)], M. Omichi [a)], T. G. Oyama [a)], K. Oyama [a)], H. Hoshina [a)], N. Seko [a)], A. Kimura [a)] and M. Taguchi [a)]

[a)] Department of Advanced Functional Materials Research, QST

Introduction

Silicone rubbers, such as polydimethylsiloxane (PDMS), are widely used in biotechnology and medical science because of their excellent properties [1]. However, microfabrication of silicone rubbers remains to be challenging because of their high viscosity and adhesiveness (tackiness), making it difficult to fill molds and accurately reproduce shapes during soft lithography. In addition, structures made of soft silicone rubber are prone to collapse. To address these issues, we designed radiation-modifiable molecules whose hardness can be adjusted after microfabrication [2].

Experimental

Silicone oil KF-99 (molecular weight (Mw) =1600, Shin-Etsu Chemical) and silicone rubbers (HMS-993, HMS-082, HMS-053, and HMS-064; Mw=2300–55000, Gelest) were used as base materials. DMS-V05 (Shin-Etsu Chemical, Mw=800), DMS-V21, DMS-V35R, DMS-V25R, and DMS-V41 (Gelest, Mw=6000–62700) were used as crosslinking agents. 2,4,6,8-Tetramethyl-2,4,6,8-tetravinyl-1,3,5,7,2,4,6,8-tetroxatetrasilocane platinum (Sigma-Aldrich) was used as the hydrosilyl catalyst. The base materials, crosslinking agents, and catalysts were mixed at a weight ratio of 2:1:0.1. To modify the developed silicone rubber, electron beam (EB) irradiation was performed using a dual-beam electron accelerator at the Takasaki Institute for Advanced Quantum Science. The sheets were irradiated by EBs at 1 MeV, 1 mA at absorbed doses ranging from 0.2 to 4 MGy. The rubber properties were evaluated by compressive modulus testing, adhesiveness testing and surface microstructure observation.

Results and Discussion

The viscosities of developed low viscosity silicone (LVS) and Sylgard 184, conventional silicone rubber, were measured using a viscometer. LVS exhibited viscosities below 1000 mPa·s, approximately one-third that of Sylgard 184. On the other hand, the elastic modulus of silicone rubber sheets of LVS was 2.0 MPa, which limits their use in biodevices. To address this limitation, EB irradiation was applied to enhance the elastic modulus. The elastic modulus increased with EB dose, reaching 5 MPa at 0.5 MGy and 20 MPa at 4.0 MGy, exceeding that of Sylgard 184 (Fig. 1).

The adhesiveness of LVS was significantly lower than that of Sylgard 184, as shown in Fig. 2. High adhesiveness poses challenges during microfabrication using soft lithography, where the flexible PDMS can deform during mold release, causing the adjacent patterns to stick together. This improved fabricability makes LVS advantageous for detailed microfabrication.

Transfer tests were conducted on the micropillar structures to evaluate the processability of the LVS sheets. The LVS reproduced <1 μm uniform and sharp pillar structures. In contrast, Sylgard 184, with its higher viscosity and adhesiveness, failed to reliably reproduce 1 μm pillar structure. This result demonstrates that LVS is highly suitable for fabricating precise and stable microstructures.

In conclusion, this new LVS is applicable as a material for precise and high-performance biodevices and is expected to contribute to future innovations in medical technology.

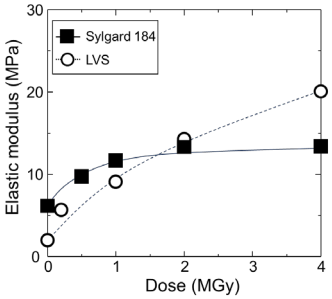

Fig. 1 Elastic modulus of Sylgard 184 and LVS sheets as a function of absorbed dose of 1 MeV EB.

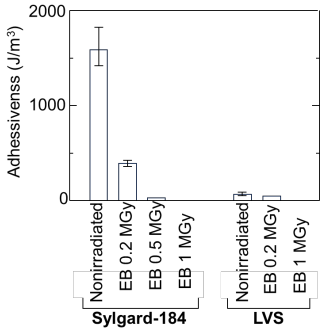

Fig. 2 Adhesiveness of Sylgard 184 and LVS sheets as a function of the absorbed dose. N = 3. Error bars, standard error of the mean.

Acknowledgments

This research was partially supported by the Innovative Science and Technology Initiative for Security (Grant Number JPJ004596, ATLA, Japan), and KAKENHI (Grant Number 22H05054, JSPS, Japan)

References

[1] Sutthiwanjampa C *et al*., *Adv Mater Interfaces*. **10,** 2202333 (2023). DOI: 10.1002/admi.202202333

[2] Kimura Y *et al*., *Polymers for Advanced Technologies*. **36**, 70089 (2025). DOI: 10.1002/pat.70089

2 - 05 Colour imaging of carbon ion beams using k-carrageenan hydrogel dosimeters based on oxidation coupling reactions

T. Tachikawa, and S. Mishima

Faculty of Engineering, Graduate School of Science and Engineering, Saitama University

Introduction

The color formers have been developed [1-2] to visually detect radiation that is harmful to the human body but cannot be detected by the human senses. In this study, the dye forming reactions via oxidative coupling [3] of *N,N*-diethyl-*p*-phenylene diamine nitrate **1** and 4-chloro-1-naphthol **2** (scheme 1 A), and of 4-aminoantipyrine **3** and the aniline derivative **4** (scheme 1 B), were applied to the colour imaging of carbon ion beams. Colour imaging of carbon ion beams using k-carrageenan hydrogel dosimeters based on oxidation coupling reactions will prove useful in particle beam therapy. These hydrogel dosimeters incorporate peroxidase (POD) to ensure stable progression of the coupling reaction.

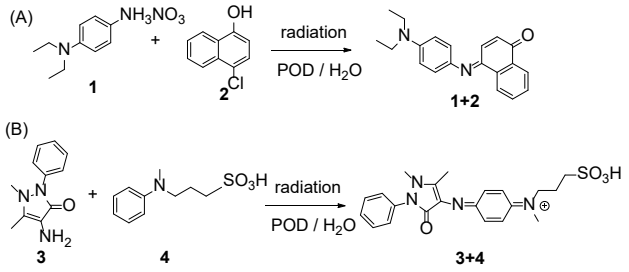

Scheme 1 Dye formation of (A) *N,N*-diethyl-*p*-phenylene diamine nitrate **1** with 4-chloro-1-naphthol **2,** and of (B) 4-aminoantipyrine **3** and the aniline derivative **4** by irradiation.

Experimental

Each reagent was weighed to achieve the final concentrations specified in the captions of Figures 1 and 2. Distilled water was then added to the weighed reagents to prepare aqueous solutions. This solution was added to κ-carrageenan which was weighed to achieve the final concentration of 15 gL^{-1}, heated to dissolve, and cooled to form the gel dosimeter.

Irradiation of carbon ion beam to the dye gel dosimeter was carried out at TIARA. 220 MeV carbon ions ($^{12}C^{+5}$) were irradiated to the dosimeters at 4 pnA for the exposure time of 30 s and 60 s with scanning the beam over the area of 7.5 cm x 7.5 cm under normal temperature and ambient pressure.

Results and Discussion

The image of hydrogel dosimeters containing **1** and **2** after a carbon ion beam irradiation is shown in Figure 1 and that of hydrogel dosimeters containing **3** and **4** is shown in Figure 2. The beam was irradiated through polyimide film from above the Petri dish.

As shown at 0 s in Figure 1, the **1**+**2** k-carrageenan hydrogel dosimeter exhibited colour development over time. Conversely, as shown at 0 s in Figure 2, the **3**+**4** hydrogel dosimeter was colourless prior to irradiation. Both dosimeters exhibited colour development after carbon ion beam irradiation. The **3**+**4** dosimeter, which had shown little colour development even at 70 Gy by the gamma-ray irradiation experiment conducted prior to the heavy-ion beam irradiation experiment, exhibited stronger colour development. While many dosimeters exhibit good colouration by gamma rays but poor colouration by heavy-ion beams, the **3**+**4** dosimeter became a rare example which exhibited poor colouration with gamma rays but very pronounced colouration with heavy-ion beams.

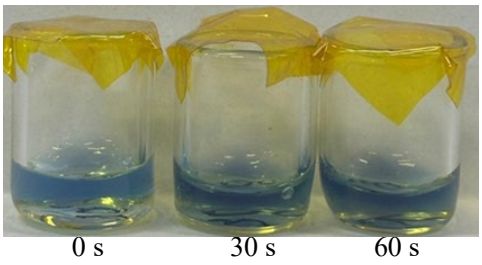

Figure 1 Images of κ-carrageenan gel of **1**+**2** after $^{12}C^{5+}$ beam irradiation ([**1**]$_0$ = 0.72 mM, [**2**]$_0$ = 0.32 mM, [POD]$_0$ = 0.40 μM, [Na_2SO_3]$_0$ = 0.02 μM, [*κ*-carrageenan]$_0$ = 15 gL^{-1}).

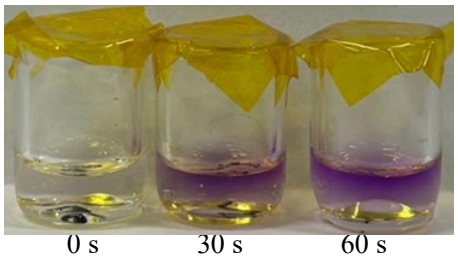

Figure 2 Images of κ-carrageenan gel of **3**+**4** after $^{12}C^{5+}$ beam irradiation ([**3**]$_0$ = 0.72 mM, [**4**]$_0$ = 0.32 mM, [POD]$_0$ = 0.40 μM, [NaOH]$_0$ = 10 μM , [*κ*-carrageenan]$_0$ = 15 gL^{-1}).

References

[1] H. Itoi, *et. al.,* Chem. Lett., **38**, 1002 (2009). DOI: 10.1246/cl.2009.1002

[2] T. Tachikawa, *et. al.,* Isotope News, **731**, 7(2015).

[3] T. Tachikawa and M Yoshioka, QST Takasaki Annual Report 2022, **66**, (2023).

2 - 06 Effects of irradiation parameters on α’ phase precipitation in FeCrAl alloys

S.Yamashita [a)], Y. Abe [a)], N. Okubo [a)], S. Ukai [a)] and T. Sasaki [b)]

[a)] Nuclear Science and Engineering Center, JAEA
[b)] Research Center for Structural Materials, NIMS

Introduction

This study continues our investigation of FeCrAl alloys, promising candidates for accident-tolerant fuel cladding materials, aiming to clarify the precipitation behavior of the embrittlement phase (α' phase) and to contribute to the development of a predictive model. In FY2024, the irradiation dose was increased from the previously achieved 0.3 dpa, and data up to 0.64 dpa (partially 1.44 dpa) were obtained. This enabled the development of an α' phase precipitation map using chemical composition, damage rate, and damage dose as parameters.

Experimental

Multiple types of strip-shaped specimens of Fe-*x*Cr-*y*Al model alloys (x = 10–21, y = 0–8 wt%) were prepared and subjected to ion irradiation testing. Ion irradiation was mainly performed at 350°C with 10.5 MeV Fe ions. Three different damage rates ranging from 8×10^{-6} to 8×10^{-4} dpa/s were applied to achieve irradiation doses of 0.24, 0.64, and 1.44 dpa.

After ion irradiation testing, the samples were processed using a focused ion beam (FIB) system to prepare specimens for three-dimensional atom probe (3DAP) and transmission electron microscopy (TEM) analyses.

Figure 1 shows a representative 3DAP reconstruction of the α' phase obtained from the ion-irradiated Fe-*x*Cr-*y*Al alloys. The 3DAP measurements in Figure 1 were obtained under the following conditions: irradiation temperature: 350°C; damage rate: 8×10^{-6} to 8×10^{-4} dpa/s; irradiation dose: 0.24, 0.64 dpa; chemical composition range: 15Cr, 15Cr-4Al, 15Cr-8Al, 17.5Cr, 17.5Cr-3Al, and 17.5Cr-8Al. Systematic comparison of the 3DAP data reveals distinct differences in the size and distribution of theα' phase depending on the damage rate, chemical composition, and damage dose.

Multiple regression analysis quantitatively demonstrated that a decrease in damage rate, along with increases in Cr concentration and damage dose, tends to increase precipitation volume fraction. Notably, Al addition was found to suppresses α' phase precipitation, providing important insights for alloy design.

References

[1] Y. Abe, *et. al.,* J. Nucl. Mater., **600**,155271 (2024).

Results and Discussion

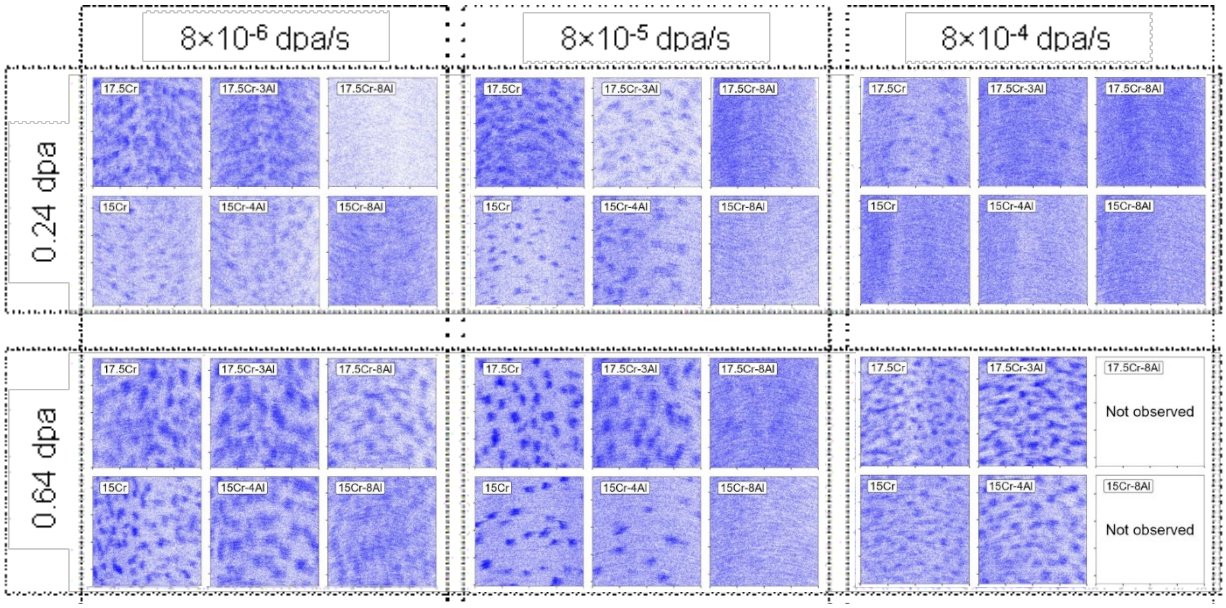

Fig.1 Three-dimensional atom probe images showing the α' phase in Fe-*x*Cr-*y*Al alloys obtained from systematic ion irradiation experiments. Damage rate (indicated at top): 8×10^{-6} to 8×10^{-4} dpa/s; irradiation dose (indicated at left): 0.24, 0.64 dpa. Chemical composition (displayed upper left of each image): 15Cr, 15Cr-4Al, 15Cr-8Al, 17.5Cr, 17.5Cr-3Al, 17.5Cr-8Al.

2 - 07 Superconducting properties of $GdBa_2Cu_3O_y$ thin films irradiated with 300 keV He-ions

T. Ozaki[a)], H. Okazaki[b)], H. Koshikawa[b)], S. Yamamoto[b)] and T. Yamaki[b)]

[a)]School of Engineering, Kwansei Gakuin University,
[b)]Department of Advanced Functional Materials Research, QST

Introduction

High-temperature superconductors (HTS) based on $REBa_2Cu_3O_y$ (REBCO, RE = rare earth) are powerful materials to operate high field applications such as medical imaging machines, magnetically-levitated trains and compact nuclear fusion reactors. For these applications, it is crucial to raise the critical current density J_c in magnetic fields. The high in-field J_c performance could be obtained by introducing precipitates and defects with nano-meter size, which can pin the vortices. The desirable vortex-pinning defects can be provided by ion irradiation, which enables the creation of various structural defects in REBCO films.[1,2] In this work, we present superconducting properties in GdBCO thin films irradiated with 300 keV He-ions.

Experimental

The samples were 400 nm thick GdBCO superconducting layers on clad-type textured metal substrates deposited by a pulsed laser deposition (PLD) method. The irradiation experiment was performed using 400 kV ion implanter at TIARA. A beam of 300 keV He-ions was directed to the film surface at normal incidence with 1.7×10^{14} – 3.5×10^{15} ions/cm^2 dose. The superconducting properties were measured using a Quantum Design superconducting quantum interference device (SQUID) magnetometer.

Results and Discussion

Fig. 1 shows superconducting transition temperature T_c obtained from magnetization measurement as a function of fluence for GdBCO thin films irradiated with 300 keV He-ions. We found that the T_c's of the irradiated GdBCO thin films decreased gradually with increasing fluence up to around 5.8×10^{14} ions/cm^2 (corresponding to 0.0020 dpa) and then significantly started to drop.

Fig. 2 shows J_c enhancement as a function of magnetic field for the irradiated GdBCO thin films at different doses at 5 K, where J_c enhancement is defined as (J_c of irradiated film – J_c of pristine film) / J_c of pristine film. We found that the 300 keV He-ion irradiations yielded up to ~20% J_c enhancement in the magnetic field over 5 T. These results indicate that 300 keV He-ions irradiation would be less effective to provide strong pinning defects in high-T_c GdBCO superconducting films.

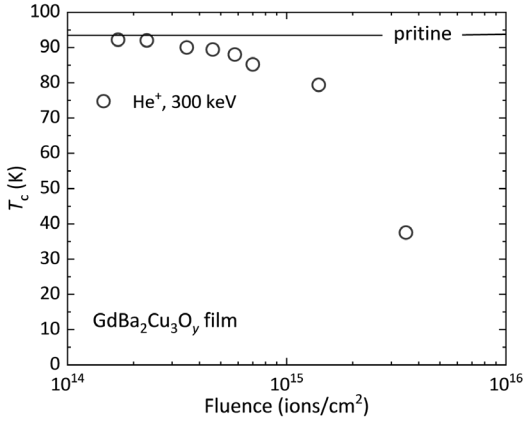

Fig. 1 Superconducting transition temperature T_c as a function of fluence for irradiated GdBCO thin films.

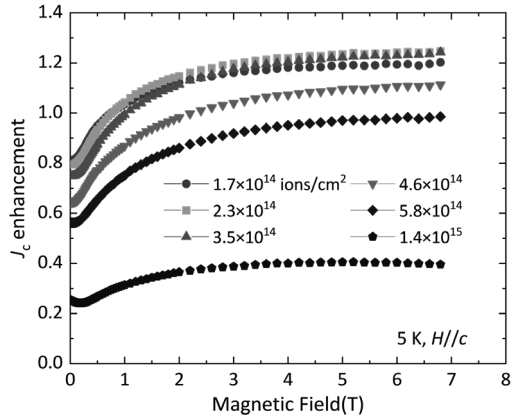

Fig. 2 Calculated J_c enhancement as a function of magnetic field at 5 K for GdBCO thin films irradiated with 300 keV He-ions.

References

[1] W. K. Kwok *et al*., Rep. Prog. Phys. 79, **116501** (2016). DOI: 10.1088/0034-4885/79/11/116501

[2] T. Ozaki *et al*., Supercond. Sci. Technol., **33** 094008 (2020). DOI: 10.1088/1361-6668/ab9f66

2 - 08 Preparation of Rh-doped TiO_2 films by reactive co-sputtering deposition

S. Yamamoto, A. Idesaki, T. Taguchi, and M. Saeki

Department of Advanced Functional Materials Research, QST

Introduction

Polymer electrolyte membrane fuel cells (PEMFCs) have attracted significant attention due to their high energy density and zero pollutant emissions. The current operating temperature of PEMFCs is approximately 80°C; however, next-generation PEMFCs require operation at around 130°C to improve power generation efficiency. Carbon-supported platinum (Pt) nanoparticles are currently the most promising catalysts for the oxygen reduction reaction (ORR). Nevertheless, these catalysts suffer from poor durability at temperatures above 100°C. Therefore, it is essential to develop electrode materials that exhibit both high durability and high catalytic activity for ORR under elevated temperature conditions. In this study, we investigated the effect of post-annealing on the microstructure of rhodium-doped titanium dioxide (Rh-doped TiO_2) films. The films were prepared by reactive co-sputtering deposition onto sapphire substrates.

Experimental

The Rh-doped TiO_2 films were grown by rf magnetron sputtering, which was performed using metallic Ti and Rh targets in an Ar and O_2 gas mixture. The single crystal sapphire substrates (α-Al_2O_3) of c-plane were used. Simultaneous deposition was performed at a substrate temperature of 500°C and sputtering power of 50 W for Ti and 5 W for Rh, respectively. The post-annealing treatment was carried out at 1000°C for 1 h in air using an electric furnace. The crystallographic structure of the films was determined by XRD. The composition and crystallinity of the films were determined by RBS/channeling measurements carried out using a 2.0 MeV $^4He^+$ beam from a 3 MV single-stage accelerator at QST/Takasaki. The microstructure of films was characterized by transmission electron microscope (TEM) operating at 200 kV, Cross-sectional TEM samples were prepared with ion slicer (IB-090600CIS, JEOL) using Ar ion.

Results and Discussion

The results of XRD measurements indicated that rutile-type (100) oriented TiO_2 films were grown on c-plane sapphire substrates both the as-deposited and the post-annealed films. Figure 1 shows the RBS spectra of the Rh-doped TiO_2 (100) films on the c-plane sapphire substrates (a) as-deposited at 500°C and (b) post-annealed at 1000°C taken under the random and the TiO_2<100> aligned conditions. The peaks at 1.72, 1.44 and 1.11 MeV correspond to the Rh and Ti components in the Rh-doped TiO_2 film and the Al component in the sapphire substrate, respectively. The atomic ratio of Rh to Ti was 2.4% as determined by RBS. The reduction of the normalized yields of Ti and Al and Rh in the aligned conditions reveal the TiO_2 <100> crystallographic axis is parallel to the sapphire <0001> axis and doped Rh atoms were substituted into the TiO_2 lattice sites. Furthermore, it can be confirmed that the doped Rh atoms are further substituted into the titanium lattice by post-annealing treatment at 1000°C for 1 h in air.

Figure 2 shows a cross-sectional TEM image of the Rh-doped TiO_2 film grown on the c-plane sapphire substrate (post-annealed at 1000°C). As can be seen, the Rh-doped TiO_2 film (129 nm thick) deposited onto the sapphire substrate shows no precipitation of Rh nanoparticles was observed within the film. STEM-EDS elemental mapping confirmed that Rh atoms were uniformly distributed throughout the TiO_2 matrix. Results from RBS and TEM revealed that Rh atoms were incorporated into the TiO_2 crystal lattice sites.

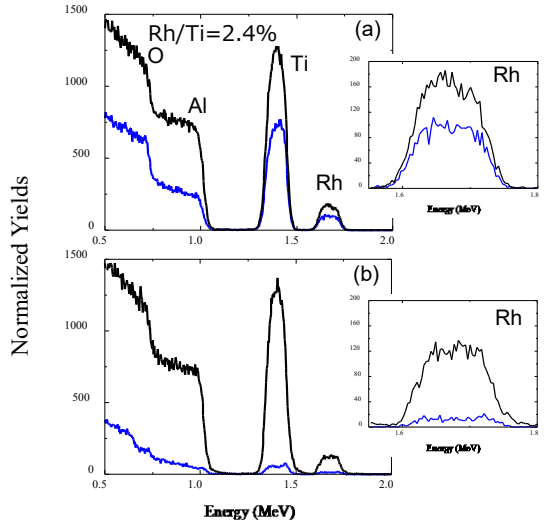

Fig. 1 RBS/channeling spectra of a Rh-doped TiO_2 film on c-plane sapphire substrate (a) as-deposited at 500°C and (b) post-annealed at 1000°C for 1 h in air.

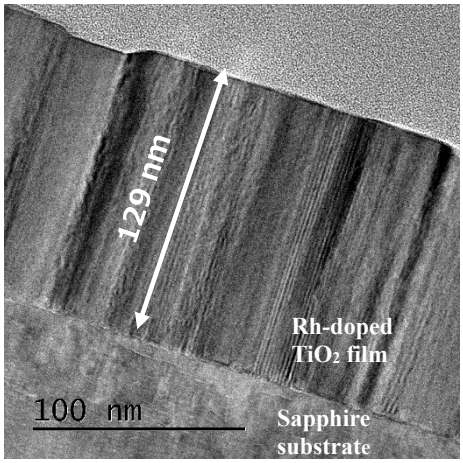

Fig. 2 Cross-sectional TEM image of a Rh-doped TiO_2 film grown on the c-plane sapphire substrate with post-annealed at 1000°C for 1 h in air.

2 - 09 Flexural properties of impregnation resins for superconducting magnets before and after gamma-ray irradiation

X. Wang [a)], A. Kikuchi [b)], M. Takeuchi [c)], H. Murakami [d)], S. Sonoda [d)], and K. Hamada [d)]

[a)] Accelerator Laboratory, KEK
[b)] Research Center for Energy and Environmental Materials, NIMS
[c)] RIMTEC Corporation
[d)] Department of Tokamak System Technology, QST

Introduction

The radiation resistance and mechanical properties of impregnation resins are important for superconducting magnets [1-4]. In this study, an organic olefin-based thermosetting dicyclopentadiene resin, commercially available as TELENE® from RIMTEC Corporation, and an epoxy resin, CTD-101K, were irradiated to approximately 20 MGy at room temperature using a Cobalt-60 source at the Takasaki Advanced Radiation Research Institute. Three-point bending tests were carried out to measure the flexural properties of these resins.

Experimental

Three types of resins were prepared for irradiation and three-point bending tests: TELENE®, a mixture of TELENE® and Gd_2O_2S powder, and CTD-101K. The diameter and mixing ratio of the Gd_2O_2S powder were about 10 μm and 43 wt%, respectively. The resin samples were 80 mm long, 8 mm wide, and 4 mm thick. The resin samples were inserted into glass tubes as shown in Fig. 1, and evacuated to below 10^{-2} Pa for irradiation tests under high vacuum conditions. Before the three-month irradiation, the dose rate was measured using polymethyl methacrylate dosimeters. The absorbed dose for each resin sample was calculated as the product of dose rate and irradiation time. Three-point bending tests were conducted at room temperature before and after irradiation when the sample doses reached approximately 1 MGy, 5–6 MGy, 9–10 MGy, and 17–19 MGy. A 1 kgN load cell was attached to the SHIMADZU AG-5000C and used to press the center of the resin sample to measure its bending properties. The test parameters conformed to JIS K7171 and ISO 178. The flexural stress (σ_f) and flexural strain (ε_f) are defined from the measured force (F) and deflection (s) as $\sigma_f=3Fd/2wt^2$ and $\varepsilon_f=6st/d^2$, where d, w, and t are the span between specimen supports of 64 mm, the sample width of 8 mm, and the sample thickness of 4 mm.

Results and Discussion

The dose rate varied from 6 kGy/h to 8.5 kGy/h depending on the distance from the radiation source. Based on the maximum dose rate, the sample temperature could increase by 2 K/h. None of the three resin samples appeared to melt or deform after irradiation. The measured flexural stress and flexural strain before and after irradiation are shown in Fig. 2. The pure and mixed TELENE® exhibited plastic deformation and tolerated larger strains than CTD-101K without fracture before irradiation and after 1 MGy irradiation, but their allowable strain before fracture decreased at doses above 5 MGy. The improved flexural properties of CTD-101K after 5 MGy irradiation may caused by the absence of oxygen and the cross-linking reaction induced by irradiation [1].

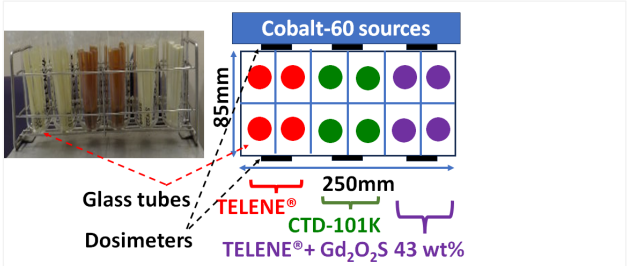

Fig. 1 The arrangement of the resin samples for irradiation tests.

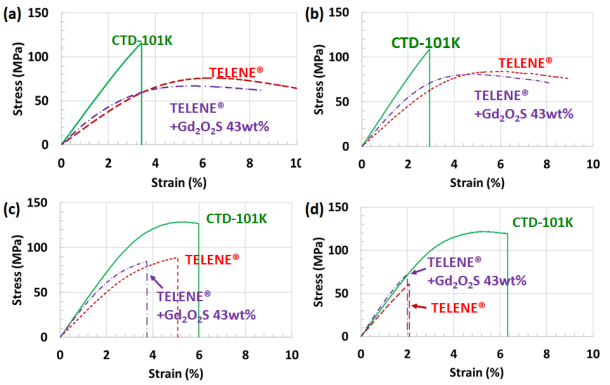

Fig. 2 The flexural stress and flexural strain of the three resins: (a) before gamma-ray irradiation, (b) 1 MGy, (c) 5–6 MGy, and (d) 17–19 MGy.

Acknowledgments

A part of this work was supported by the U.S.-Japan Science and Technology Cooperation Program in high energy physics operated by MEXT in Japan and DOE in the U.S.

References

[1] D. M. Parragh *et al.*, Polymers **16**, 407 (2024). DOI: 10.3390/polym16030407
[2] E. Barzi *et al.*, Supercond. Sci. Technol. **37**, 045008 (2024). DOI: 10.1088/1361-6668/ad2c25
[3] A. Musso *et al.*, IEEE Trans. Appl. Supercond. **32**, 7700405 (2022). DOI: 10.1109/TASC.2022.3157255
[4] X. Wang *et al.*, IEEE Trans. Appl. Supercond. **35**, 7700405 (2025). DOI: 10.1109/TASC.2025.3537947

2 - 10 Development of polymeric sealing materials utilizing radiation technique (2)

A. Idesaki, S. Hasegawa, K. Yoshimura, A. Hiroki, and Y. Maekawa

Department of Advanced Functional Materials Research, QST

Utilization of hydrogen is one of the most promising solutions to realize the carbon neutrality. So far, manufacture and sales of fuel cell vehicles (FCVs) and construction of hydrogen refueling stations (HRSs) have been strongly progressing in Japan: number of FCVs sold is about 8,000 and number of HRSs installed is about 150, as of 2024. The number of installations of HRSs in one of the most important issues; it should be increased to promote the popularization of FCVs.

On the other hand, application of fuel cells for heavy duty vehicles (HDVs) such as trucks, trains, ships, and so on, has been considered recently. Since the instruments and specifications of current HRSs are for light duty vehicles (LDVs), it is necessary to develop HRSs with updated specifications for the HDVs. For example, mounting amount of hydrogen for HDVs is expected to be 400 kg, although the mounting amount of hydrogen for LDVs is about 6 kg. It would be indispensable to greatly increase the flow rate of hydrogen for refilling the tank in reasonably short time. To achieve such specifications, instruments of compressors and accumulators with high performance should be developed. These instruments include some parts made of polymeric materials as hoses, sealings, and so on. We aim at the development of sealing parts with high performance through modification of polymeric materials utilizing radiation technique.

The polymeric materials are used as dynamic sealings in the compressors and accumulators, therefore, the properties of sliding property, airtightness for hydrogen and abrasion resistance are required. The abrasion resistance relates closely to surface hardness of materials; the abrasion resistance generally become high as the surface hardness is high. In the previous report, change of surface hardness of high-density polyethylene (HDPE), as a model material, by gamma-ray irradiation was investigated, and it was found that the surface hardness increased after the irradiation with dose of above 50 kGy at room temperature in air (Fig. 1) [1]. On the other hand, it is well-known that elongation at break of HDPE in tensile test decreases after the gamma-ray irradiation in air. Then, the tensile tests of irradiated HDPE were conducted at room temperature (Fig. 2). While the initial value of the elongation at break was 286%, it was slightly increased after the irradiation. This result suggests that the surface hardness can be improved without decreasing in the elongation, that is, abrasion resistance of HDPE can be modified with retaining its flexibility.

In order to optimize the irradiation conditions, relationship between the irradiation conditions of gamma-rays and abrasion resistance will be investigated.

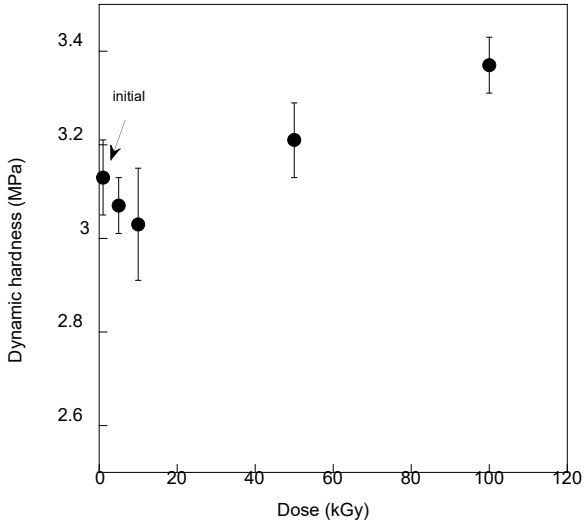

Fig. 1 Change of surface hardness of HDPE after gamma-ray irradiation at room temperature in air.

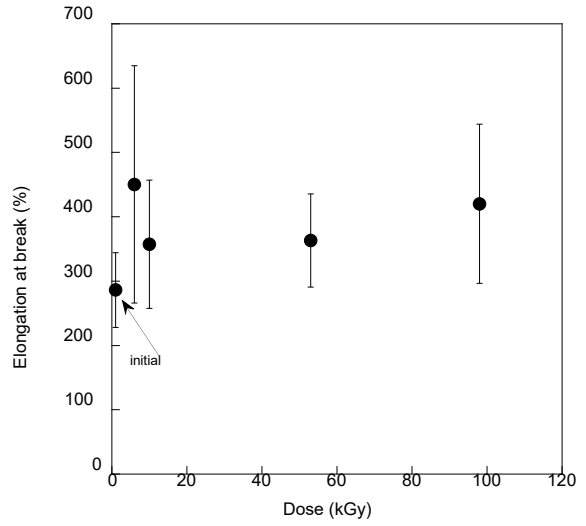

Fig. 2 Change of elongation at break of HDPE in tensile test after gamma-ray irradiation at room temperature in air.

Acknowledgments

This work is based on results obtained from a project, JPNP23004, commissioned by the New Energy and Industrial Technology Development Organization (NEDO).

References

[1] A. Idesaki *et al*., QST Takasaki Annu. Rep. 2023, **QST-M-52** 36 (2025).

2 - 11 Modification of polymeric materials by quantum beam irradiation (5)

A. Idesaki, A. Hiroki, S. Hasegawa, and Y. Maekawa

Department of Advanced Functional Materials Research, QST

According to the Basic Hydrogen Strategy, revised in June 2023, efforts for popularization of fuel cell vehicles (FCVs) and hydrogen (H_2) refueling stations (HRSs) are positioned as one of the most important issues in the field of mobilities. Especially, the costs of FCVs should be reduced to realize the popularization. For example, the cost of current high pressure-H_2 tank for the FCVs is ¥700,000; the cost is required to be reduced to around ¥300,000. The common high pressure-H_2 tank for FCVs, type IV tank, is composed of plastic liners and carbon fiber reinforced plastics (CFRPs). It is effective to reduce the amount of expensive carbon fiber to realize the low cost-tank, therefore, novel high performance-polymeric materials which can be alternative to the CFRPs have been strongly desired.

The materials in the type IV tank are exposed repeatedly to severe conditions such as high pressure of 70 MPa, wide temperature range of -40°C to 85°C. Especially, the materials must retain sufficient durability against the high pressure-H_2; the materials with low H_2 gas permeability and high mechanical properties are desirable as shown as "TARGET ZONE" in Figure 1. Referring to the Fig. 1, we have been examined radiation crosslinking of polymeric materials such as polyethylene (PE), polyamides (PA), and their polymer blends [1-4]. In this work, PA/PE (80/20 in wt%) with 5 phr of compatibilizer was irradiated by gamma-rays at room temperature under vacuum. After the irradiation with dose of 75 kGy, the gel fraction of PA/PE was 13%, indicating that the PA/PE blend was crosslinked by the irradiation. The irradiated PA/PE blend was exposed to 90 MPa H_2 gas at 30°C for 24h. After the exposure, the samples were kept at ambient pressure for 24h, and then the extent of destruction was evaluated by light transmission method [5]. Figure 2 shows destruction level of PA/PE blend: red color indicates untransmit light and severe destruction, blue color, transmit light and mild destruction. The destruction is attributed by generation of voids and/or cracks after H_2-exposing test. Although the destruction was very severe in the case of unirradiated sample, the destruction became milder as the dose increased.

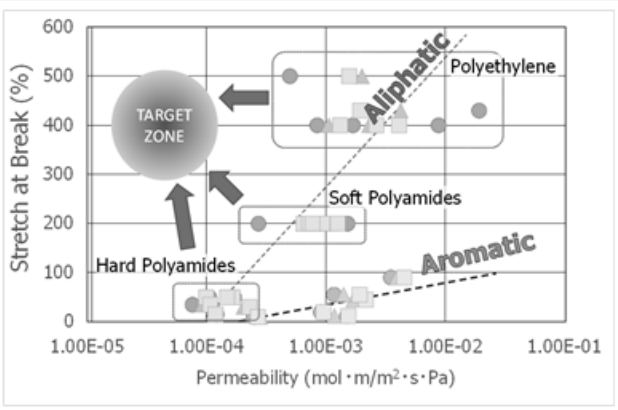

Fig. 1 Relationship between H_2 permeability and tensile property for various polymeric materials presented by Prof. Nishimura at Kyushu University.

According to the results above, it was found that the resistance for high pressure H_2 gas of PA/PE can be modified greatly by the radiation crosslinking.

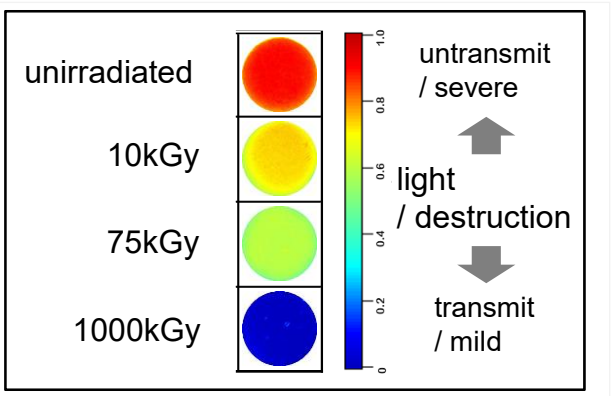

Fig. 2 Destruction level of PA/PE (80/20) blends in the high pressure-H_2 exposing test after gamma-ray irradiation.

Acknowledgments

This work is based on results obtained from a project, JPNP20003, commissioned by the New Energy and Industrial Technology Development Organization (NEDO). This is a collaboration work with Prof. Shin Nishimura at Kyushu University and Prof. Katsuhisa Tokumitsu at The University of Shiga Prefecture.

References

[1] A. Idesaki *et al.*, QST Takasaki Annu. Rep. 2020, **QST-M-33** 27 (2022).
[2] A. Idesaki *et al.*, QST Takasaki Annu. Rep. 2021, **QST-M-39** 34 (2023).
[3] A. Idesaki *et al.*, QST Takasaki Annu. Rep. 2022, **QST-M-47** 42 (2024).
[4] A. Idesaki *et al.*, QST Takasaki Annu. Rep. 2023, **QST-M-52** 35 (2025).
[5] H. Fujiwara *et al.*, **Int J Hydrogen Energy** 46 11831 (2021).

2 - 12 Poly(methyl methacrylate) cylindrical microstructures created using proton beam writing for microstructure-assisted microscopy

T. Sano [a], K. Tobe [a], A. Tsuji [b], K. Kosumsupamala [a], N. Puttaraksa [a], H. Seki [a], Y. Ishii [c], T. Matsui [b], and H. Nishikawa [a]

[a] Shibaura Institute of Technology
[b] Mie University
[c] Department of Advanced Quantum Beam Technology, QST

Introduction

A typical optical microscope encounters a diffraction limit of ~200–250 nm resolution[1], making nanoscale imaging challenging. Existing super-resolution methods can solve this issue. However, those techniques are costly and require labeling.[2] We presented a simple and label-free approach using poly(methyl methacrylate) or PMMA cylindrical microstructures to aid in Blu-ray disc nanopattern imaging.[3]

Experimental

Proton beam writing (PBW) at TIARA (3 MV Single-Ended Accelerator) with a 1 MeV proton beam was used to fabricate PMMA cylindrical microstructures on a ~5×5 mm size of cut Blu-ray discs. The PMMA layers on the Blu-ray disc substrates were made by a spin-coating method (500 rpm for 10 s at the first step and 2000 rpm for 60 s for the second step), followed by soft-baking. A proton microbeam (~1 μm beam spot) was utilized to irradiate selected regions outside the desired microstructure regions. The PMMA cylindrical microstructures were created on the Blu-ray discs by developing in a 7 (isopropanol): 3 (DI water) for ~20 mins. A laser confocal microscope (Olympus LEXT OLS 4000) was employed to obtain images of Blu-ray disc nanopatterns aided by PMMA cylindrical microstructures using a laser confocal mode at 405 nm wavelength.

Results and Discussion

In our study[3], the PMMA cylindrical microstructures were produced with different diameters of 3–9 μm with an increment of 2 μm. The images were taken using the laser confocal microscope at 20x objective lenses (0.6 numerical aperture, NA). As one example, the laser confocal microscope image of 5 μm-diameter PMMA microstructures on the Blu-ray disc substrate is shown in Fig. 1(a). When zoomed in the microstructure, the Blu-ray disc nanopatterns were perceived in the microstructure. We could not observe the nanopatterns without assisting by the PMMA cylindrical microstructures using the 20x objective lens. According to the results in our publication[3], it was demonstrated that a higher contrast and sharp edge of the image could be achieved by a smaller microstructure diameter for the case of PMMA cylindrical microstructure-assisted microscopy. Details of this investigation can be found elsewhere.[3]

Although, the mechanism of microstructure-assisted microscopy is still unclear. The solid immersion lens and photonic nanojet (PNJ), which is the highly confined and intense focusing light beam, may influence in the help in nanoimaging by the microstructures.[3] Nonetheless, theoretical study is further required to understand how the microstructure could aid in nanoimaging.

In summary, we presented the PMMA cylindrical microstructures produced by the PBW method. The assistance of PMMA microstructures in imaging of Blu-ray disc nanopatterns was also demonstrated.

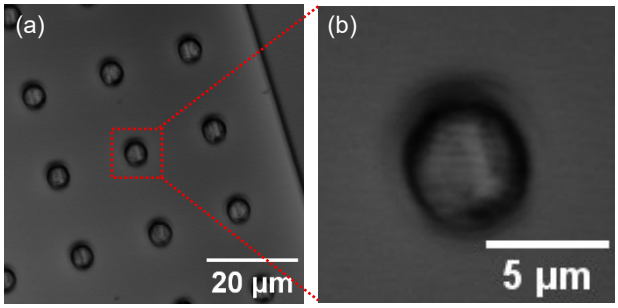

Fig.1 (a) Laser confocal microscope image of PMMA cylindrical microstructures of 5 μm diameters on Blu-ray disc, taken with a 20×/0.6 NA. (b) Nanopatterns of Blu-ray disc observed assisted by the PMMA microstructure as marked in (a).

Acknowledgments

This work was supported by JSPS KAKENHI Grant No. JP23K04558.

References

[1] A. Darafsheh, J. Appl. Phys. **131**, 031102 (2022). DOI: 10.1063/5.0068263
[2] G. Huszka, and M. A.M. Gijs, Micro and Nano Engineering **2**, 7-28 (2019). DOI: 10.1016/j.mne.2018.11.005
[3] T. Sano *et al.*, Jpn. J. Appl. Phys. **64**, 03SP44 (2025). DOI: 10.35848/1347-4065/adba6a

2 - 13 Evaluation of materials for a new individual dosemeter using electron spin resonance spectroscopy

T. Oka [a], H. Seito [b], E. Yokozuka [b], Y. Kumagai [a], and N. Nagasawa [b]

[a] Nuclear Science and Engineering Center, JAEA
[b] Department of Advanced Quantum Beam Technology, QST

Introduction

Alanine ($C_3H_7O_2N$) dosimeters using electron spin resonance (ESR) are recognized as standard methods employed in various applications of radiation dosimetry [1] for measuring high doses (0.1–100 kGy) and has limited sensitivity <10 Gy [2]. Thus, measuring doses as low as the mGy order becomes difficult. As a clue to new candidate materials that can evaluate mGy order of radiation, this study focused on ESR biological dosimetry using teeth. The estimated lower detection limit using Japanese wild macaque tooth enamel is 33.5 mGy [3], indicating that this method can accurately assess doses <1 Gy. In this work, we investigated the applicability of commercially available synthesized apatite as the new solid dosimeter material instead of biological enamel, from the viewpoint of estimation of low-dose radiation <1 Gy.

Experimental

A commercially available synthesized apatite, namely, HAP-200 (Taihei Chemical Industry, Osaka, Japan), was used. Samples were irradiated with ^{60}Co gamma rays from 100 mGy to 75 Gy at the gamma-ray irradiation facility of the QST Takasaki Institute for Advanced Quantum Science in air at room temperature. After irradiation, samples were transferred to quartz tubes for ESR measurement. Unirradiated samples were also measured for spectral evaluation before irradiation. The peak height of the radiation-induced radical was defined as the radical intensity (Figure 1) and the relationship between the radical intensity and the absorbed dose (dose–response curve) was observed.

Results and Discussion

Figure 1 shows the ESR spectra obtained from HAP-200 and biological hydroxyapatite in tooth enamel. HAP-200 showed a typical ESR signal shape attributed to the CO_2^- radical as obtained in the tooth enamel and other radiation-induced radicals around 334.9 mT maybe due to the CO_3^- radicals.

Figure 2 shows the dose–response curve at low doses. Considering the 90 % upper and lower prediction lines, the lower detection limit of HAP-200 was ~100 mGy. There are several detectors which can detect mGy order irradiation, such as ionization chamber, pocket dosimeter, and so on, however, they have a fixed direction to detect the radiation, the size of these detectors is relatively large to put it next to the small sample to evaluate the absorbed dose. Although HAP-200 would need to be mold into an appropriate shape of a few-mm-sized tablet/rod as alanine dosimeter, HAP-200 can be a good candidate sample for the disposable solid dosimeter without any directional characteristics to use in reproduction/simulation of radiation effects caused by low-dose radiation such as expected in the FNPP accident, evaluate the absorbed dose of a mm-sized small sample, etc.

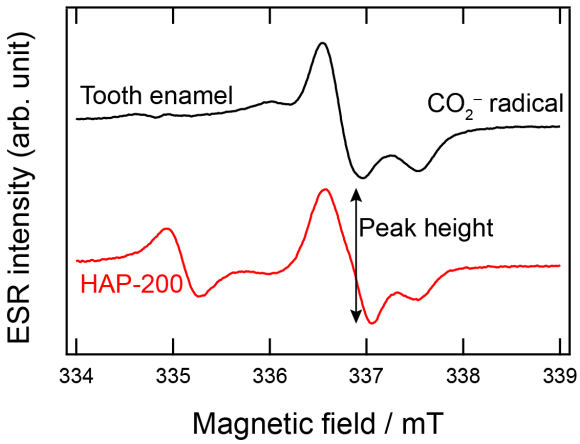

Fig. 1 ESR spectra of tooth enamel and HAP-200. Radical intensity was determined from the peak height of the signal.

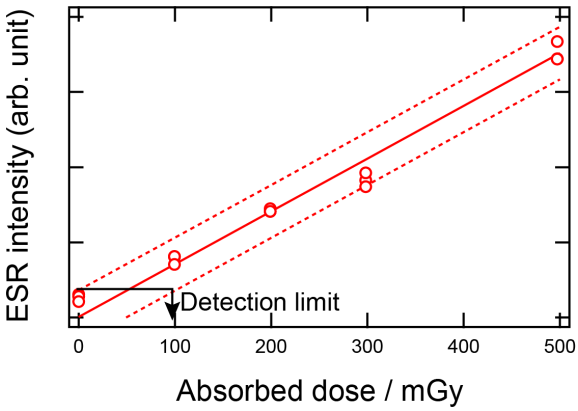

Fig. 2 Dose–response curve for HAP-200 at a lower dose. The solid line represents the linear least squares fit, the dashed lines represent the 90 % prediction bands, and the solid arrow represents the lower limit of the detection dose.

References

[1] ISO/ASTM 51607:2013.
[2] Y. Kitamura, *et al*., Radiat. prot. dosim. **200**, 1660 (2024). DOI: 10.1093/rpd/ncae194
[3] T. Oka *et al*., Radiat. Meas. **134**, 106315 (2020). DOI: 10.1016/j.radmeas.2020.106315

2 - 14 Development of novel dosimetry based on the cellulose pyrolysis behavior

S. Hosoi [a),b)], M. Omichi [b)], H. Hoshina [b)], N. Seko [a),b)], N. Nagasawa [b)], H. Seito [b)], S. Yamasaki [b)], H. Morishima [c)], and K. Ohshima [c)]

[a)] Graduate School of Science and Technology, Gunma University
[b)] Department of Advanced Functional Materials Research, QST
[c)] Technical Research Laboratory, Kurabo Industries Ltd.

Introduction

Electron beam (EB) induced graft polymerization is used as a method to add new functions to polymers. In the EB induced graft polymerization, it is important that the cellulose fibers are uniformly irradiated. This is because homogeneous irradiation leads to uniform graft polymerization [1]. In general, it is confirmed whether the absorbed dose of the polymer substrate is uniform by measuring the absorbed dose on the front and back surfaces of the substrate using radio chromic films such as cellulose triacetate (CTA) dosimeter. However, in the CTA dosimeter, it is known there is a discrepancy between the measured absorbed dose and the actual absorbed dose for low acceleration voltages, because the CTA dosimeter causes dose decay within the dosimeter when irradiated to electron beam [2]. We focused on the radiolysis and pyrolysis of paper (cellulose sheet). Irradiated cellulose is known to decrease in molecular weight depending on the absorbed dose, and its pyrolysis behavior changes. In this study, we propose a novel dosimetry determined from the pyrolysis behavior of cellulose.

Experimental

Paper wipes (Kimwipes®) were used as cellulose sheets in this study. The cutting paper wipes (average size: 2 x 2 cm, wight: ~8 mg) were packed into a gas barrier bag, which was sealed under a vacuum and then irradiated by an electron beam an acceleration voltage of 250 keV in a nitrogen atmosphere for an irradiation dose of 10-60 kGy. Thermogravimetric analysis was performed on the irradiated paper wipes under nitrogen flow (400 mL/min) at a heating rate of 40°C/min to 300°C. Furthermore, the 20 layers of paper wipes were packed into a gas barrier bag, which was sealed under a vacuum and then irradiated by an electron beam an acceleration voltage of 150 keV in a nitrogen atmosphere for an irradiation dose of 50 kGy. Paper wipes were evaluated for adsorbed dose by the thermogravimetric analysis.

Results and Discussion

Fig. 1(a) shows DTG curves of irradiated paper wipes at irradiation doses of 10-60 kGy. The DTG value increased with the irradiation dose between 250°C and 300°C. This result suggests that electron irradiation accelerates the pyrolysis of cellulose depending on the adsorbed dose. By using this correlation between adsorbed doses and DTG values, it is possible to measure local adsorbed dose. We used the correlation to examine whether the local absorbed dose measured from DTG values at 280°C. Fig. 1(b) shows the absorbed doses distribution for irradiated paper wipes with an acceleration voltage of 150 keV and irradiation dose of 50 kGy by using the correlation. The absorbed dose of paper wipe was significantly lower than the irradiated dose. The reason why is that electron beams at 150 keV have a short penetration depth. By using CTA dosimeters, the adsorbed dose on the back side of the vacuum pack was 7.9 kGy. In contrast, the adsorbed dose measured from DTG value of paper wipe was 29.0 kGy. This result indicates that paper wipe can measure local absorbed dose with higher resolution than CTA film with 125 μm thickness. Paper wipe is thinner and has a much higher porosity than CTA film (Paper wipe: 60-70 μm, CTA film: 125 μm). CTA film must be less than 15μm thick to achieve the same resolution as a paper wipe. Therefore, paper wipes are less sensitive to the decay of the EB. The proposed method can be expected to measure the local absorbed doses with high resolution without using a specialized radio chromic film.

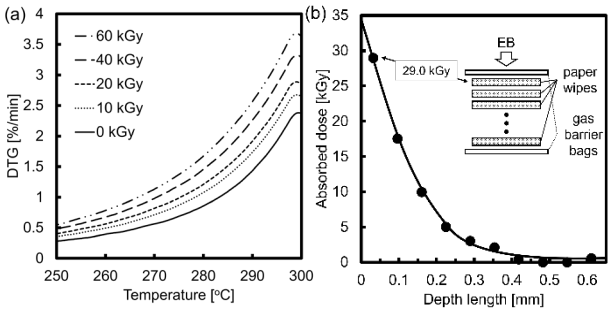

Fig.1 (a) DTG curves of irradiated paper wipes at 10-60 kGy. (b) Absorbed dose distribution for irradiated paper wipes at acceleration voltages of 150 keV.

Acknowledgments

This work was supported by JSPS KAKENHI Grant Number JP23K04430.

References

[1] M. Omichi *et al*., Polym. Degrad. Stab., **231**, 111087 (2025). DOI:10.1016/j.polymdegradstab.2024.111087
[2] K. Matsuda *et al*., Int. J. Appl. Radiat. Isot., **42**, 235, (1991). DOI:10.1016/0883-2889(91)90082-C

2 - 15 Synthesis of superacidic polymer materials through post-modification strategies

M. Kuroiwa [a)], M. Omichi [b)], N. Seko [b)] and R. Kakuchi [a)]

[a)] Division of Molecular Science, Faculty of Science and Technology, Gunma University
[b)] Department of Advanced Functional Materials Research, QST

Introduction

Polymers with strong acid functionalities are widely applied as polyelectrolytes, ion-exchange and proton-conducting membranes, and immobilized catalysts. Among them, sulfonic acid–containing polymers are most common due to their strong acidity and established commercial availability. However, the identical acidity and high ionic nature of sulfonic acids limit their physicochemical tunability. To expand polymer acid chemistry, superacid derivatives such as bis(trifluoromethane)sulfonimide (Tf_2NH) have been introduced, offering distinct structural and chemical properties compared with sulfonic acids. Another promising class is bis[(trifluoromethyl)sulfonyl]methane (Tf_2CH_2) derivatives, whose central carbon atom enables substitution, generating highly acidic carbon acids with stable conjugate bases. Despite their potential, synthetic challenges have restricted their use in materials science. Recently, a zwitterionic reagent, 2-(2-fluoropyridin-1-ium-1-yl)-1,1-bis(trifluoromethylsulfonyl)ethan-1-ide ($2FPy^+$-CH_2-C^-Tf_2), was developed to generate reactive 1,1-bis[(trifluoromethyl)sulfonyl]ethylene ($Tf_2C{=}CH_2$) in situ [1]. This intermediate rapidly reacts with nucleophiles, allowing facile incorporation of Tf_2CH groups into small molecules. Although previously limited to small-molecule chemistry, its broader potential remains unexplored. This study applies $2FPy^+$-CH_2-C^-Tf_2 to polymer and material sciences through postpolymerization modification and radiation-induced graft polymerization, enabling the introduction of Tf_2CH_2 moieties onto polymer backbones and surfaces.

Experimental

Non-woven polyethylene/polypropylene (PE/PP) fabrics (1.4 × 2.8 cm) were first irradiated with 200 kGy electron beams under air-free condition to create radicals on the surface. These activated substrates were immersed in a degassed solution of styrene and 4-acetoxystyrene and reacted at 60 °C for 3 h, giving PE/PP-*g*-P(St-*co*-StOAc) with a grafting degree of 233%. The acetoxy groups were then deprotected by sequential treatment with TBAOH/MeOH and HCl/EtOH, affording PE/PP-*g*-P(St-*co*-StOH). Finally, surface modification was achieved by immersion in a mixed solvent of MeCN/$CHCl_3$ containing $2FPy^+$-CH_2-C^-Tf_2 at room temperature for 24 h, yielding PE/PP-*g*-P(St-*co*-StOH-CH_2CTf_2H). The obtained membranes were subsequently analyzed by FT-IR, optical microscopy, and SEM-EDX to evaluate surface functionalization and morphological stability.

Results and Discussion

After graft polymerization and acetyl deprotection, PE/PP-*g*-P(St-*co*-StOH) was obtained and reacted with $2FPy^+$-CH_2-C^-Tf_2. FT-IR analysis clearly showed the emergence of a sulfonyl absorption peak at 1102 cm^{-1}, indicating the anchoring of Tf_2CH units on the membrane surface. To evaluate the structural integrity of the modified material, optical microscopy and SEM (Fig. 1) were performed. These observations confirmed that the fibrous morphology and overall shape of the PE/PP membrane remained intact, even after incorporation of bulky fluorinated segments. Moreover, SEM-EDX elemental mapping revealed uniform distribution of signals corresponding to Tf_2CH units along the fibers, supporting efficient and homogeneous surface modification. Taken together, these results demonstrate that the surface reaction with $2FPy^+$-CH_2-C^-Tf_2 proceeded smoothly and selectively, producing PE/PP membranes coated with strong carbon acid functionalities. This study highlights the potential of the method as a versatile and mild strategy for introducing unique chemical moieties into membrane materials without impairing their structural features, opening opportunities for applications in functional membranes and advanced material design.

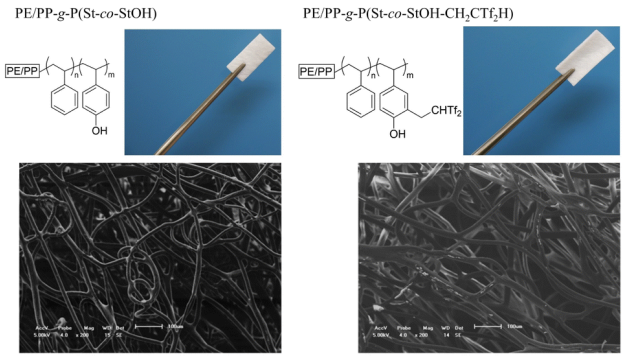

Fig. 1 Optical (top) and SEM (bottom) images of PE/PP-*g*-P(St-*co*-StOH) membranes before and after surface functionalization with $2FPy^+$-CH_2-C^-Tf_2.

Acknowledgments

R. K. gratefully acknowledges the S-Membrane Project at Gunma University for the financial support.

References

[1] H. Yanai *et al.*, Chem. Commun., **49**, 10091-10093 (2013).

2 - 16 Development of anionic polymer electrolyte membranes using aromatic hydrocarbon polymers by radiation-induced graft polymerization and their alkaline resistance.

S. Hasegawa, K. Yoshimura, A. Hiroki, Y. Zhao and Y. Maekawa

Department of Advanced Functional Materials Research, QST

Anion exchange membranes (AEMs) play a crucial role in energy conversion devices such as fuel cells (FCs) and electrolyzers to separate reactants while transporting anions essential for the cell operation. At the current state of AEM research, high conductivity and alkaline durability have become a main concern, because these properties control power generation efficiency and durability under operating conditions. One solution for high conductivity is to increase the ion exchange capacity (IEC), however, AEMs with higher IEC exhibit critical issues of insufficient durability and severe damage in a hydrated state under flooding conditions.

Radiation-grafted AEMs are a promising candidate to overcome the abovementioned trade-off problem because these AEMs comprise semicrystalline base polymers that are thermally and mechanically robust, and functionalized graft polymers that can easily tune the IEC for high conductivity by controlling the grafting degree (GD). In our previous work, we have successfully made AEMs using poly(ethylene-co-tetrafluoroethylene) (ETFE) as base polymer with functionalized graft with ionic groups, that exhibited excellent power density of ~710 mW/cm^2 and durability up to ~670 h, which is one of the most durable alkaline-type FC so far reported [1]. To further improve durability, we recently targeted on poly(ether ether ketone) (PEEK), one of hydrocarbon “super engineering plastics” as base polymer, which has higher mechanical/thermal stability than ETFE, and most importantly fluorine-free. However, PEEK is too chemical-resistant to proceed polymerization, and few examples reported radiation grafting onto PEEK. Most lately, we have overcome synthesis difficulties and successfully made PEEK-based AEMs with ammonium grafts (see Fig. 1), which show super-balanced FC properties over ETFE-based AEMs [2].

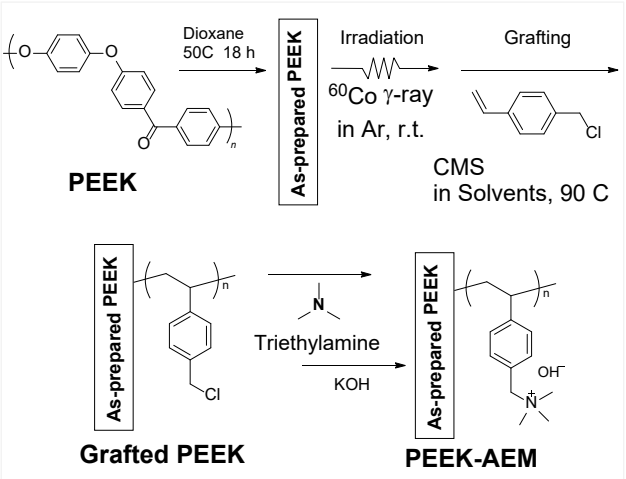

Fig. 1 Synthesis scheme of PEEK grafted CMS by RGP and subsequent quaternization reaction

Specifically, PEEK base films (Victrex Inc.) with a thickness of 16 μm and crystallinity degree of 11% were firstly annealed in dioxane (DOX) at 50°C for 18 hours. Then, the annealed films were irradiated with ^{60}Co γ-ray @ Takasaki irradiation facility at room temperature in Ar with absorbed dose of 160-640 kGy. Next, the films were immersed in chloromethyl styrene (CMS)/solvent (1/1 v/v) at 90°C for a certain time to proceed graft polymerization and obtain grafted-PEEK membrane. The GD was determined by the weight increase of the membrane and plotted in Fig. 2. It shows that GD reaches > 80% when tetraethylene glycol was used as a solvent, which is much higher than the case of using DOX. This result indicates solvent-induced conformational change in the membrane is crucial for achieving high GD and consequently a high IEC, the phenomenon of which is worthy for further study in future.

The grafted-PEEK membranes were finally converted to PEEK-based AEMs by reacting with triethylamine and N-alkylation. The obtained AEMs possess a high IEC of ~1.7 mmol/g and excellent anion conductivity of 128 mS/cm at 60°C [2].

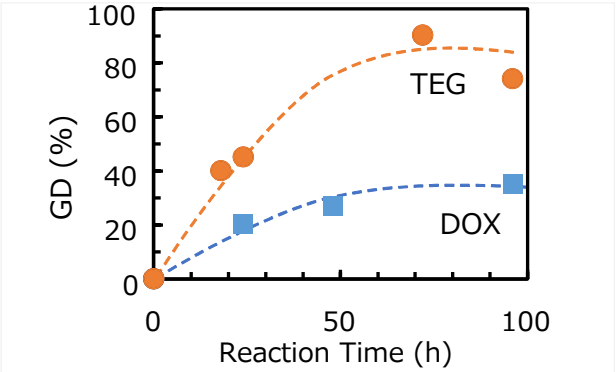

Fig. 2 Plots of GDs as a function of reaction time using (■) DOX, (●) Tetraethylene glycol (TEG) as a solvent.

Acknowledgments

This work was supported by JSPS KAKENHI Grant Number JP 20K05625

References

[1] Zhao, Y., *et al*., Macromolecules, **57**, 1998-2007 (2024).
[2] Hasegawa, S. *et al*., Patent PCT/JP2024/033579.

2 - 17 Microstructure characterization of latest ITER-grade CuCrZr alloy

D. Hamaguchi, S. Kano and M. Ando

Department of Fusion Reactor Material Research, QST

The divertor is one of the key components in tokamak-type fusion devices. Its most important role is to remove impurities from the plasma, contributing to stable operation of the reactor. However, to achieve this, the divertor must simultaneously withstand high thermal loads and neutron loads. Therefore, most required performance for materials are good heat removal capability and endurance to neutron irradiation. For such reasons, copper is selected as the heat sink material for the divertor because copper has one of the highest thermal conductivity among all metals. Furthermore, CuCrZr was selected among many Cu alloys because it exhibits a smaller decrease in thermal conductivity compared to other alloys while showing sufficient strength and moderate fracture toughness. CuCrZr is known as precipitation-hardened alloy with many types of precipitates being formed after certain processing. However, the strengthen mechanism associated with these precipitates in CuCrZr are not yet well understood, and the same applies to the irradiation effects. Therefore, this study is aimed to investigate the stability of the precipitates in this alloy under irradiation and the impact of the precipitates on defect formation under the presence of helium using TIARA's multiple ion beam irradiation facility. Irradiation tests are currently in progress, but this report presents the characterization study of the precipitates conducted prior to the testing.

Fig. 1 shows the microstructure of ITER-grade CuCrZr at three different scales. Left picture shows an optical image representing the grain structure, middle picture shows a SEM image and right picture shows TEM image that represent precipitates morphology. Many types of precipitates are densely formed in this alloy from micrometer sized Cr-rich and Zr-rich precipitates to nanometer sized Cr-rich precipitates. To evaluate the thermal stability of these precipitates and to understand the role on the strengthen mechanism, isothermal annealing experiment from 473K to 873K with 100K intervals were conducted. The holding time for each temperature was 2 hours. Fig. 2 and Fig. 3 show the TEM image and EDS chemical mapping results representing coarse and fine precipitates morphology after 473K and 873K annealing. Fig.4 shows the temperature dependence of hardness change while annealing. From the results, it was confirmed that the coarse precipitates are rather stable even at 873K and no big changes were observed in morphology after 2h annealing. On the other hand, in case of the fine precipitates, coarsening was observed at 873K and was also confirmed the coarsening start at around 773K while no explicit changes were observed up to that temperature. Meanwhile, decrease in hardness (softening) while annealing also starts at around 773K, as is shown in Fig. 4, confirming that the type of precipitates contributes to the hardening is mostly the nanometer sized fine Cr-rich precipitates. The result well explains the strengthen mechanism of this alloy since it goes through aging process at around 750K for strengthening and suggesting that the irradiation resistance of these precipitates is one of the key issues for using CuCrZr under fusion reactor environments.

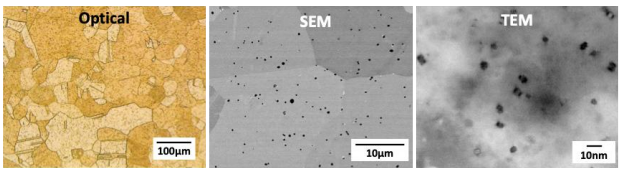

Fig. 1 Grain structure and precipitate morphology of ITER-grade CuCrZr.

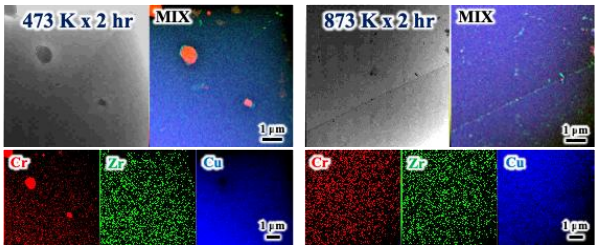

Fig. 2 TEM image and EDS chemical mapping results representing coarse precipitates after 473K and 873K 2h annealing.

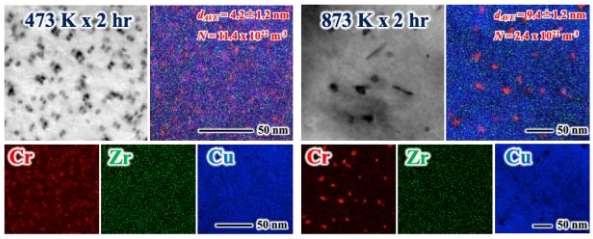

Fig. 3 TEM image and EDS chemical mapping results representing fine precipitates after 473K and 873K 2h annealing.

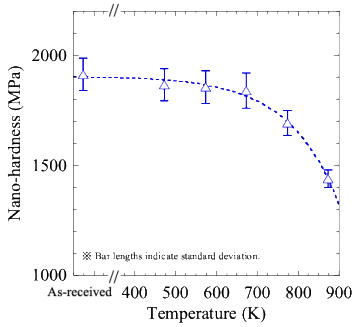

Fig. 4 Temperature dependence of the hardness change.

3 - 01 Extracellular ATP release triggered by ^{131}I-trastuzumab mitigates radiation-induced reduction in cell viability through the P2Y$_6$ receptor in SKOV3 cells

Y. Ohshima [a)], M. Tsukimoto [b)], S. Watanabe [a)], Y. Tsushima [c)] and N.S. Ishioka [a)]

[a)] Department of Quantum-Applied Biosciences, QST
[b)] Faculty of Pharmaceutical Sciences, Tokyo University of Science
[c)] Gunma University Graduate School of Medicine

Introduction

Targeted radionuclide therapy (TRT) irradiates cancer cells by administering a radioisotope or a drug that combines a radioisotope with a cancer-directed drug delivery system into the body. Unlike external beam radiation therapy, TRT is effective even for cancer that has spread throughout the body. However, some patients do not respond to TRT, and the mechanism behind this remains unclear.

Intracellular ATP is released extracellularly by various stimuli and activates ATP-selective receptors (P2 receptors) expressed on the cell membrane. Extracellular ATP is known to be involved in therapeutic resistance in the tumor microenvironment. For example, activation of the P2Y$_2$ or P2Y$_6$ receptor promotes DNA repair, cancer cell growth, and metastasis. Therefore, the extracellular nucleotide signaling in the tumor microenvironment has become a new target for cancer therapy. However, it remains unclear whether TRT induces extracellular ATP release and activates P2 receptors. Therefore, in this study, we prepared β-emitting ^{131}I-labeled trastuzumab (^{131}I-trastuzumab) and examined extracellular ATP release and its roles in TRT [1].

Experimental

Trastuzumab was labeled with ^{131}I using the chloramine-T method. The radiochemical yield was 77.04 ± 16.14% (n=5) and the specific activity was 344.6 MBq/mg. The binding of ^{131}I-trastuzumab to cells was investigated using human epidermal growth factor receptor 2 (HER2)-positive cells (SKOV3) and HER2-negative cells (MCF7). Extracellular ATP was determined by measuring chemiluminescence using a luciferin–luciferase reagent. The growth inhibitory effects of ^{131}I-trastuzumab were investigated by colony formation assay. To investigate the effect of ecto-ATPase, apyrase was added 30 min before treatment with ^{131}I-trastuzumab. To investigate the effects of P2 receptor agonists or antagonists, cells were incubated in the presence or absence of UTP (100 μM), UDP (100 μM), PPADS (10 μM), suramin (10 μM), and MRS2578 (1 μM) for 30 min before treatment with ^{131}I-trastuzumab.

Results and Discussion

^{131}I-trastuzumab bound exclusively to SKOV3 cells. Treatment with ^{131}I-trastuzumab at 4 MBq/mL and higher concentrations significantly increased extracellular ATP levels, whereas non-radioactive trastuzumab didn't (Fig. 1). These results suggest that ATP release was specifically induced by radiation derived from ^{131}I. The growth inhibitory effects of ^{131}I-trastuzumab were significantly enhanced by pretreatment with apyrase (ecto-ATPase) or MRS2578 (a P2Y$_6$-selective antagonist), whereas they were significantly reduced by treatment with a P2Y$_6$-selective agonist (UDP) (Fig. 2).

In conclusion, ^{131}I-trastuzumab induced extracellular ATP release, and the released ATP was shown to be involved in mitigating radiation-induced reduction in cell viability through P2Y$_6$ receptor.

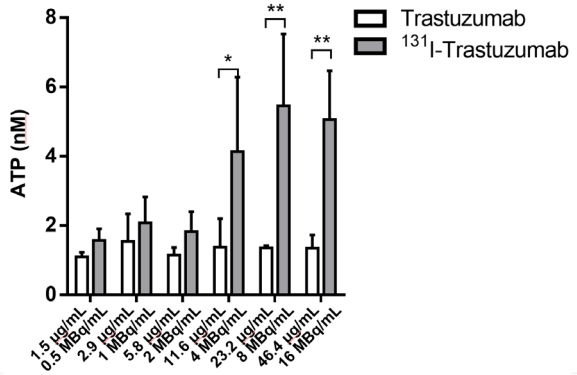

Fig. 1 Extracellular ATP release from SKOV3 at 20 min after treatment with ^{131}I-trastuzumab or non-radioactive trastuzumab (n=4-12). A statistically significant difference is indicated by * ($p < 0.05$) or ** ($p < 0.01$).

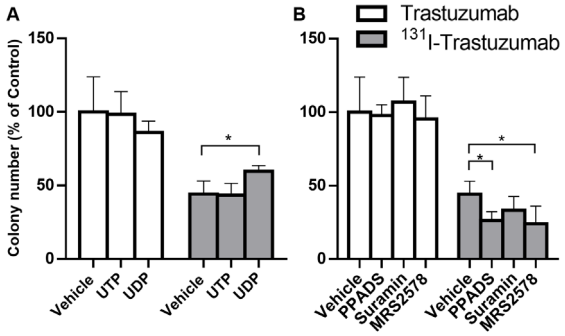

Fig. 2 Effects of P2 receptor agonists (A, n=4) or antagonists (B, n=4) on clonogenic growth after ^{131}I-trastuzumab treatment. A statistically significant difference is indicated by * ($p < 0.05$).

References

[1] Y. Ohshima *et al.*, Biol. Pharm. Bull. **47**, 1868 (2024). DOI: 10.1248/bpb.b24-00427

3 - 02 Exploration of High-LET ionizing radiation- specific DNA lesions using $^{40}Ar^{13+}$ beam around the track end

K. Akamatsu [a)], N. Shikazono [a)] and K. Satoh [b)]

[a)] Department of Quantum Applied Photonics, QST
[b)] Quantum Materials and Applications Research Center, QST

Introduction

Ionizing radiation-induced DNA damage can cause mutation and carcinogenesis. In particular, “clustered damage”, that is a DNA region with two or more lesions within a few helical turns, is believed to be hardly repaired. This damage would be induced around high-LET ionizing radiation tracks. However, detail of the damage is unknown. We have already developed some methods for estimating localization of apurinic/apyrimidinic sites (APs) on DNA using fluorescence resonance energy transfer (FRET) between Alexa dye- labeled APs [1,2]. By means of the FRET methods, we found that the higher LET radiation produces more clustered damaged sites by the direct [3] and indirect effects [4]. However, FRET signals from clustered damaged sites are almost hidden in the intense fluorescence from numerous amounts of isolated lesions. In a high-LET ionizing radiation, an isolated lesion would be produced by a diffusible radical such as •OH apart from the radiation track. We hypothesize that a high-LET radiation track on DNA produces “crushed” low molecular weight DNA fragments and simultaneous two or more dsb in a DNA molecule. The “direct” dsb site could have a few base lesions around the DNA end. Using supercoiled pUC19 DNA, we explore high-LET radiation- specific DNA damage using Ar ion beam at the track end.

Experimental

●Aqueous DNA sample preparation and irradiation

PUC19 was used for DNA samples to be irradiated. The DNA was dissolved in pure water to be ~4 μg/μL. Two hundred microliters of the DNA solution was injected into a closed chamber (16mm ϕ x 1mm, in air or in N_2) with a Kapton film (7.5μm) and was irradiated with TIARA 460MeV $^{40}Ar^{13+}$ beam of AVF cyclotron. The LET at the surface of the DNA solution was approximately 18 MeV•cm^2/mg. The dose was ca. 10 kGy (fluence: 2 x 10^{10} /cm^2). It is noted that the beam does not penetrate the aqueous sample.

●Dry DNA sample preparation and irradiation

Two hundred microliters of the DNA solution (~4 μg/μL in water) was mounted on a glass plate (10mmϕ x 1mm) and was dried to be a thin film (~1 mg/cm^2). The plate with DNA was put into the chamber. Ar irradiation was performed at a dose of 77 kGy (LET: 24 MeV•cm^2/mg, fluence: 2 x 10^{10} /cm^2). The irradiated DNA was re-dissolved in 200μL of deionized water.

●Ultrafiltration of irradiated DNA sample

The irradiated aqueous DNA samples were ultrafiltrated using MWCO 5,000 spin column. The filtrate was concentrated for chemical analyses (e.g., HPLC, LC/MS). The residue on the filter membrane was re-dissolved to deionized water.

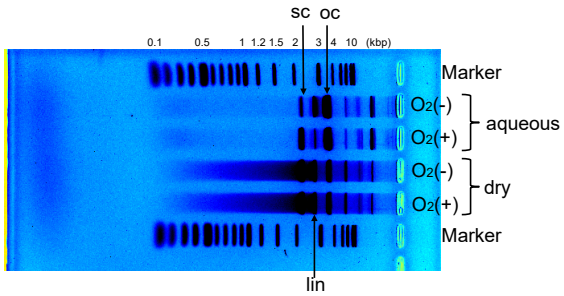

Fig. 1 Agarose gel electrophoretic analysis of Ar-irradiated pUC19 in aerobic or anaerobic condition. Sc: supercoiled-, oc: open circular-, lin: linear form- plasmid DNA.

Results and Discussion

Figure 1 shows an image of agarose gel electrophoretic analysis of Ar-irradiated pUC19. Interestingly, in the aqueous DNA samples, considerably short DNA fragments with Mw of 0.1~0.5 bp were found even though a lot of sc-, oc-, lin- formed DNA with the original base pairs (2686 bp) remained. Such short DNA fragments can be produced near the radiation track. Moreover, strand break yield for aqueous DNA in an anaerobic condition seems to be higher than that for in aerobic one. On the other hand, in the case of dry DNA, no significant difference was seen between the two. Short DNA fragments were also found as seen in the case of aqueous DNA. However, distributions of the DNA fragments were significantly different between dry and aqueous DNA samples. In any case, such a gel image is not obtained in an experiment using low-LET radiation, e.g., γ- or X-rays. More analyses of the short fragments should be needed. Fragments with Mw < 5,000 are now not found except for released unaltered bases (cytosine, guanine, thymine, adenine) from DNA strands.

References

[1] K. Akamatsu *et al.*, Anal. Biochem. **433**, 171 (2013). DOI: 10.1016/j.ab.2012.10.004
[2] K. Akamatsu *et al.*, Anal. Biochem. **536**, 78 (2017). DOI: 10.1016/j.ab.2017.08.007
[3] K. Akamatsu *et al.*, Anal. Bioanal. Chem. **413**, 1185 (2021). DOI: 10.1007/s00216-020-03082-w
[4] K. Akamatsu *et al.*, Radiat. Res. **201**, 150 (2024). DOI: 10.1667/RADE-23-00145.1

3 - 03 Lethal effects of gamma rays and helium ion beam radiations in *Bradyrhizobium ottawaense*

K. Satoh and Y. Hase

Department of Quantum-Applied Biosciences, QST

Introduction

The increase in agricultural production due to population growth has been supported by the excessive use of chemical fertilizers. However, the release of nitrous oxide (N_2O) into the atmosphere from excess nitrogen poses a significant environmental burden on the nitrogen cycle, causing a greenhouse effect approximately 300 times stronger than CO_2 and contributing to ozone layer depletion. N_2O emissions account for 5% of greenhouse gases and continue to increase year by year. Moreover, 52% of anthropogenic N_2O emissions originate from agricultural activities using high amounts of nitrogen chemical fertilizers. Therefore, to maintain sustainable agricultural production systems, it is necessary to develop technologies that reduce the usage of nitrogen chemical fertilizer and restore the nitrogen cycle.

Bradyrhizobium ottawaense is a nitrogen-fixing bacterium isolated from soybean nodules in Ottawa, Canada, in 2014 [1]. The complete genome sequence of the type strain, *B. ottawaense* OO99, was published in 2018 [2]. *B. ottawaense* OO99 possesses not only the nitrogen-fixing ability but also the N_2O-reducing ability, raising expectations for its use in N_2O reduction [3]. In this study, to generate strains with an enhanced N_2O-reducing ability using quantum beam breeding technology, we investigated the lethal effects of gamma rays and helium ion beam radiations in strain OO99.

Experimental

B. ottawaense OO99 was kindly provided by Dr. S. Okazaki (Tokyo University of Agriculture and Technology, Japan). *B. ottawaense* OO99 cells were cultivated at 28 ºC in modified HM broth (mHM, HM broth [4] supplemented with 0.5% mannitol, 0.025% yeast extract and 0.05% L-arabinose) with agitation for 3 days. Cells were harvested and washed in 10 mM sodium phosphate buffer (pH 7.0, PB). Cells were resuspended in 1% skim-milk/1.5% sodium glutamate solution. Aliquots (0.1 mL) of the cell suspensions were dropped onto cellulose membrane set on mHM agar plate. Cells were irradiated with helium ion beam ($^4He^{2+}$ [50 MeV; 16 keV/μm]) accelerated by an AVF cyclotron at the TIARA or with ^{60}Co gamma rays (0.2 keV/μm) at the Gamma-ray Irradiation Facility, QST. The irradiation dose ranged from 50 to 300 Gy. Irradiated cells were harvested, diluted appropriately with PB, and dropped onto mHM agar plate. Cells were incubated at 28 ºC for 5 days prior to the enumeration of colonies under a stereomicroscope. The surviving fraction was determined by calculating the number of surviving colonies divided by the total number of viable colonies. The survival data were fitted to the single-hit multi-target survival model. D_{10} is the dose quantity necessary for decreasing the survival fraction to 10%.

Results and Discussion

B. ottawaense OO99 cells showed sensitivities to both radiations depending on radiation dose. The helium ion beam-irradiated cells showed a slightly higher sensitivity than that of the gamma-irradiated cells (Fig. 1), although there were no significant differences. The D_{10} values of helium ion beam and gamma rays radiation were 74 and 90 Gy, respectively. These results suggest that helium ion beams had a higher lethal effect on *B. ottawaense* OO99 cells than gamma rays.

Further analysis will investigate the irradiation doses required to induce an efficient mutagenic effect using acquisition of antibiotic resistance in *B. ottawaense* OO99.

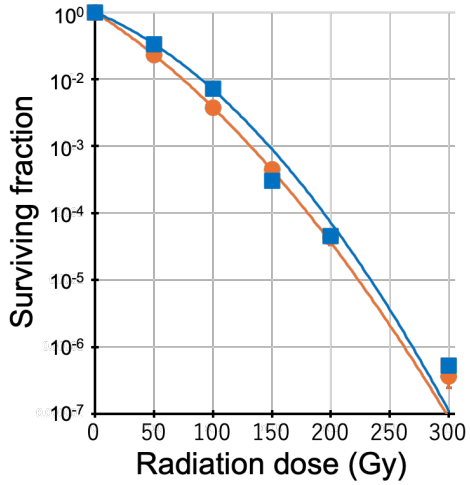

Fig. 1 Survival curves of *B. ottawaense* OO99 exposed to gamma rays and helium ion beams. Symbols: closed squares, gamma rays; closed circles, helium ion beams.

References

[1] X. Yu *et al.*, Int. J. Syst. Evol. Microbiol. **64**, 3202 (2014). DOI: 10.1099/ijs.0.065540-0

[2] H.D. Nguyen *et al.*, Microbiol. Resour. Announc. **7**, e01477-18 (2018). DOI: 10.1128/MRA.01477-18

[3] S. Wasai-Hara *et al.*, Microbes Environ. **35**, ME19102 (2000). DOI: 10.1264/jsme2.ME19102

[4] M.A. Cole and G.H. Elkan, Antimicrob Agents Chemother **4**, 248 (1973). DOI: 10.1128/AAC.4.3.248.

3 - 04 Breeding of Antarctic oleaginous yeast by ion beam irradiation

M. Tsuji [a, b], S. Kudoh [b], K. Satoh [c] and Y. Hase [c]

[a] Department of Material Science, NIT Asahikawa College
[b] Bioscience Group, NIPR
[c] Department of Quantum-Applied Biosciences, QST

Introduction

Oleaginous yeasts are a group of yeasts capable of producing and accumulating lipids from carbon sources such as sugars. These yeasts play a significant role in biotechnology, especially in the production of biofuels and bioplastics. Many oleaginous yeasts can efficiently produce lipids under various environmental conditions, making them promising candidates for sustainable resource utilization [1].

Oleaginous yeasts have advantages over oilseed plants and microalgae because they grow much faster (doubling time is usually less than an hour), accumulate cell mass to much higher densities, and are less affected by seasonal or weather conditions. However, cold environments cover a large portion of our planet. Approximately 85% of the biosphere is permanently exposed to temperatures below 5 °C [2]. In general, most of the oleaginous yeasts can grow at intermediate temperatures around 30 °C. However, as the temperature decreases, the production of fatty acids by these yeasts also decreases. For this reason, it is expected that microorganisms capable of growing at cold temperatures will be used to increase the production of microbial fatty acids in the cold temperature region. This study investigates the fatty acid production capabilities of Antarctic yeast *Cystobasidium ongulense* using glucose as carbon sources. The aim is to investigate the potential of irradiated *C. ongulense* for biofuel production by evaluating yeast growth, fatty acid content in the dry cell wight and composition under different temperature conditions.

Experimental

C. ongulense 9A-2 cells were irradiated with ion beams ($^{12}C^{5+}$ [220 MeV; 107 keV/μm]) accelerated by an AVF cyclotron at TIARA, QST. The irradiation dose ranged from 10 to 200 Gy. Production of fatty acids from glucose in irradiated cells was performed in YPD liquid medium (2 % glucose, 1% yeast extract and 2% peptone) at 5° to 15 °C. This experiment was performed in triplicate.

Whole-cell lipid content was calculated as total fatty acids. Accumulated lipids were extracted from 100 mg lyophilized cells using a hydrochloric acid-catalyzed methylation method. Briefly, following cultivation, the cells were centrifuged, lyophilized, and weighed. The lyophilized cells were then dissolved in a mixture of methanol with toluene and subjected to direct transmethylation with 8% (v/v) methanolic HCl at 105 °C for over 1 hour. The obtained fatty acid methyl esters were extracted with n-hexane and analyzed by gas chromatography equipped with a flame ionization detector (model GC353, GL Science, Japan) at an initial temperature of 140 °C for 15 min. Temperature was then increased to 240 °C at a rate of 4 °C min^{-1}. Fatty acids were identified by comparison using fatty acid methyl ester (FAME) mix as a standard (Supelco 37 component FAME mix).

Results and Discussion

The original 9A-2 strain exhibited a yield of 0.39 g/L at 15 °C. This accounted for approximately 11.7% of the dry cell weight (DCW), Linoleic acid accounted for 78.0% of DCW. On the other hand, extraction of lipid from irradiated *C. ongulense* cells at 15°C yielded 1.55 g/L. This constituted about 33% of DCW. Linoleic acid was the most predominant fatty acid in the cells at 83.4% when cultured at 15°C in YPD liquid medium. Elaidic acid also accounted for 6.6% of the total of fatty acids.

Lipid extraction from irradiated *C. ongulense* cells cultured at 5 °C yielded 9.9 g/L, accounting for approximately 88% of DCW. The major component of fatty acids in the cells at 5 °C was linoleic acid (C18:2), which accounted for 92.4% (Table 1).

The results of this study will contribute to the production of biofuels in cold environments using irradiated Antarctic yeast.

Table 1
Fatty acid composition of irradiated *Cystobasidium ongulense* and the concentration in DCW cultured at 15 °C and 5 °C by YPD liquid medium.

	15 °C	**5** °C	Original 9A-2 at 15 °C
Linoleic acid (C18:2)	83.4	92.4	78.0
Elaidic acid (C18:1 - trans (n9))	6.6	7.6	6.4
DCW (g/L)	4.69	5.63	3.33
Lipid (g/L)	1.55	4.95	0.39
Lipid content (w/w %)[a]	33.0	88.0	11.7
Lipid yield (w/w %)[b]	6.25	19.57	2.08

*ND = not detected, a: lipid (g/L) / DCW (g/L) × 100, b: lipid (g/L) / total sugar consumed (g/L) × 100

References

[1] S. Papanikolaou *et al.*, Eur. J. Lipid Sci. Technol. **113**, 1052 (2011). DOI: 10.1002/ejlt.201100015
[2] G. Felloer *et al.*, Nat. Rev. Microbiol. **1**, 200 (2003). DOI: 10.1038/nrmicro773

3 - 05 Role of the DR0041 and DR0042 proteins in DNA repair of the radioresistant bacterium *Deinococcus radiodurans*

K. Inoue [a)], K. Satoh [b)] and I. Narumi [a)]

[a)] Graduate School of Life Sciences, Toyo University
[b)] Department of Quantum-Applied Biosciences, QST

Introduction

Deinococcus radiodurans is a radiation-resistant bacterium capable of surviving exposure to high doses of gamma rays. The radiation resistance of *D. radiodurans* is due to its superior DNA repair mechanisms in response to DNA damage [1]. *D. radiodurans* possesses two orthologs of the homologous recombination repair protein Rad52, which is found in eukaryotes. One is DdrA, which is also present in closely related *Thermus* bacteria [2], and the other is DR0041, which is found only in *Deinococcus* species [3, 4]. The gene *dr0041*, which encodes the DR0041 protein, forms an operon with the downstream gene, *dr0042* (Fig. 1). This suggested that DR0042 may also be involved in DNA repair. Therefore, in this study, we conducted deletion analysis of DR0041 and DR0042 proteins.

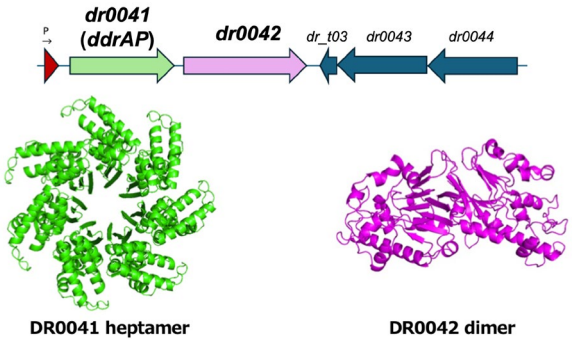

Fig.1 The *dr0041-dr0042* operon structure (upper) and the predicted structure of DR0041 and DR0042 proteins (bottom)

Experimental

Gene deletion mutants were generated from the wild-type strain (R1) of *D. radiodurans*: Δ*dr0041*, Δ*dr0041R*, Δ*dr0042*, and Δ*dr0041-dr0042* strains. In the Δ*dr0041* strain, the promoter of the antibiotic resistance gene marker is oriented in the same direction as the *dr0042* gene; therefore, the downstream *dr0042* gene is expressed via transcriptional read-through in this mutant. In contrast, in the Δ*dr0041R* strain, the promoter is oriented opposite to the *dr0042* gene; therefore, the downstream *dr0042* gene is not expressed. Therefore, strains Δ*dr0041R* and Δ*dr0041-dr0042* were expected to exhibit the same phenotype.

Results and Discussion

The results of the stress tolerance tests are shown in Fig. 2. All deletion mutants showed greater resistance to bleomycin (Bm) than the wild type. Additionally, the strain Δ*dr0041* was more sensitive to mitomycin C (MMC) than the wild type, whereas the Δdr0041R and Δdr0041-dr0042 strains showed similar levels of resistance as the wild type, and the strain Δ*dr0042* exhibited greater resistance than the wild type. Furthermore, strains Δ*dr0041*, Δ*dr0041R*, and Δ*dr0041-dr0042* were resistant to novobiocin (NB).

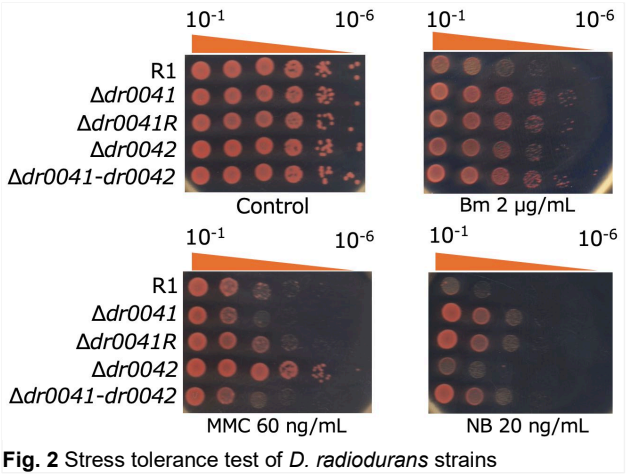

Fig. 2 Stress tolerance test of *D. radiodurans* strains

These differences in resistance to DNA-damaging agents suggest that DR0041 and DR0042 proteins work together in DNA repair. In addition, because novobiocin is an inhibitor of the B subunit of DNA gyrase, it is suggested that the DR0041 and DR0042 proteins may interact with the B subunit of DNA gyrase, distorting its three-dimensional protein structure, thereby weakening the binding of novobiocin to the B subunit. Because all deletion mutants showed resistance to bleomycin, we plan to test whether they also exhibit similar resistance to gamma rays in future studies.

Acknowledgments

A part of this research was supported by a Grant-in-Aid for Scientific Research (23K05015) and a fund from the Toyo University Priority Research Promotion Program.

References

[1] Y. Ishino and I. Narumi. Curr. Opin. Microbiol. **25**, 103 (2015). DOI: 10.1016/j.mib.2015.05.010.
[2] D. R. Harris *et al.*, PLOS Biol. **2**, 1629 (2004). DOI: 10.1371/journal.pbio.0020304.
[3] Y. Futami *et al.*, QST Takasaki Annu. Rep. 2019, **QST-M-29**, 97 (2021).
[4] A. K. Ujaoney *et al.*, Int. J. Biol. Macromol. **248**, 125885 (2023). DOI: 10.1016/j.ijbiomac.2023.125885.

3 - 06 A low-cost and simple hydroponic system to cultivate hundreds of rice plants

Y. Hase, N. Suzui, Y.−G. Yin and N. Kawachi

Department of Quantum-Applied Biosciences, QST

Rapid generation advancement is essential to research and breeding of rice. A simple hydroponic system, namely single-tube hydroponics, has been developed to cultivate dozens of rice plants using a plant incubator [1]. However, this system is practically difficult to apply for a large-scale cultivation. Mutation breeding of rice requires hundreds to thousands of mutagenized plants to obtain useful mutant lines. It will be useful not only for generation advancement but also mutant screening if hundreds of rice plants can be uniformly cultivated with a hydroponic system. To this end, while referring to the single-tube hydroponics, we developed a low-cost and simple hydroponic system to cultivate hundreds of rice plants.

Uniform cultivation is very difficult when many plants are cultivated with high density, because plants located in the center of a population cannot get enough light to grow. To overcome this problem, we used a growth retardant to reduce the plant height and also optimized the arrangement of plants.

A test cultivation system is composed of two plastic trays and a reservoir tank connected each other, and 100 liters of hydroponic solution was circulated using a water pump (Fig. 1A). The 1/80 strength of Murashige & Skoog basal salts supplemented with microelements and ferric ions were used as a culture solution. Initial pH value was adjusted to around 4.5 with hydrochloric acid. The uniconazole-P, a gibberellin biosynthesis inhibitor, was added with a concentration of 1.7×10^{-6} % to reduce the plant height. Deionized water was added to the reservoir tank basically once a week. In order to hold 15-ml plastic tubes with the bottoms cut off, in which seedlings were inserted, a rigid polyurethane foam (510-mm wide × 610-mm length × 15-mm thickness) with 180 holes was placed on the top of plastic trays. Two-week-old seedlings of cv. Nipponbare were inserted into the 15-ml tubes. At this time, it is not necessary to pull out the roots from the bottom of 15-ml tube, because many new roots will soon develop from basal nodes (Fig. 1B). The cultivation system was placed in a room controlled around 27°C. Plants were grown under short-day conditions (10-h light /14-h dark) with white LED lights (150 ~ 200 μmol /m^2 /s).

Fig. 1C shows the change of pH value throughout the growth period. The culture solution contains both ammonium ions and nitrate ions. The pH value once decreases as the rice plants preferentially absorb ammonium ions, and then pH value increases after the plants start to absorb nitrate ions. Nutrients corresponding to 100 liters of culture solution was added when the pH value reached above 5.0 (Fig. 1C). By this way, pH values were kept around 4.0 to 5.0 without any manual adjustment. The plants started heading 60 days after seed sowing and seeds matured before 90 days after seed sowing (Fig.1 D). The plant height was 25.6 ± 1.8 cm (mean ± SD) and the number of seeds per plants was 6.9 ± 2.9. In this hydroponic system, additional plastic trays can be easily connected to increase the total number of plants. These results indicate that this hydroponic system can be used to grow hundreds of rice plants with simple management.

Reference

[1] M. Kuroda *et al.*, Biosci. Biotechnol. Biochem. **79**, 63 (2015). DOI: 10.1080/09168451.2014.951026

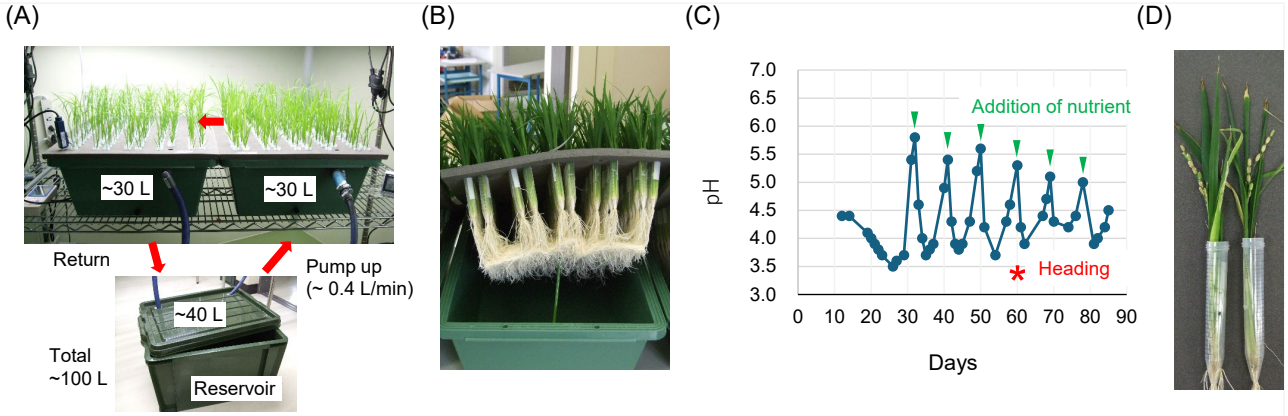

Fig. 1 A low-cost and simple hydroponic system to cultivate hundreds of rice plants. (A) A hydroponic system made by using commercially available materials. Red arrows indicate the flow of hydroponic solution. (B) Plants at 30 days after seed sowing. (C) Changes in pH value of hydroponic solution. Green triangles indicate the day in which nutrient was added. A red asterisk indicates the heading date. (D) Representative plants at the maturity stage.

3 - 07 Mutant analysis for DNA double-strand break repair genes in ion-beam-irradiated *Arabidopsis* seeds and seedlings

S. Kitamura [a)], K. Satoh [a)], R. Yoshihara [b)], N. Shikazono [c)] and Y. Hase [a)]

[a)] Department of Quantum-Applied Biosciences, QST
[b)] Department of Regulatory Biology, Saitama University
[c)] Department of Quantum Applied Photonics, QST

Introduction

Mutations are fundamental for evolution and biodiversity in all organisms. Artificial mutagenesis has been conducted to generate novel genetic lineages showing desirable characteristics in plants and microorganisms. Ionizing radiations effectively induce DNA double-strand breaks (DSBs). DSBs in plants are repaired via several independent pathways, including canonical non-homologous end joining (c-NHEJ) and alternative end-joining (alt-EJ), each of which has low and high mutability, respecitvely. In this study, knockout mutants for c-NHEJ and alt-EJ pathways were used for elucidating contributions of the two pathways in physiologically different materials to genome integrity after ion beam irradiation.

Materials and methods

Arabidopsis thaliana wild-type Columbia-0, was used in this study. Seeds of *ku70* and *lig4*, which are c-NHEJ deficient mutants, and *teb*, which is an alt-EJ deficient mutant, were obtained by Arabidopsis Biological Resource Center and propagated in our laboratory. Dry seeds and 1-day-old seedlings of wild-type and the mutants were irradiated with 17.3 MeV/u carbon ions ($^{12}C^{5+}$; LET = 107 keV/μm) accelerated by the AVF cyclotron at TIARA, QST, using a wide range of doses. The irradiated samples were grown in a growth chamber. Plants with greenish true leaves at 4 weeks after the irradiation were considered to have survived. The sensitivities of four lines were estimated as survival rates (average ± SEM among three biological replicates). Statical analysis was conducted with one-way ANOVA with post hoc Tukey HSD test.

Results and Discussion

The *ku70*, *lig4*, and *teb* seeds and seedlings were grown normaly as like the wile-type plants when they were non-irradiated. The $^{12}C^{5+}$ irradiation decreased the survival rates of the dry seeds of two c-NHEJ deficient mutants *ku70* and *lig4*. Half of the shoulder dose (Dq) values for the two lines were approximately 30–40% of the wild-type Dq value (Fig. 1A) (p = 0.001 for both mutants at 100 Gy irradiation). The *ku70* and *lig4* seedlings were also sensitive to the irradiation more than the wild-type seedlings (Fig. 1B) (p = 0.005 and 0.011 for *ku70* and *lig4*, respectively, at 30 Gy irradiation). However, the Dq values of the *ku70* and *lig4* seedlings after $^{12}C^{5+}$ irradiation were approximately 75–80% of the wild-type Dq value, which was not as extensive as those detected for the seeds. These results suggest that c-NHEJ was more critical for seeds than for seedlings after $^{12}C^{5+}$ irradiation.

The estimated Dq values of alt-EJ deficient mutant *teb* seeds and seedlings were approximately 70 and 9 Gy, respectively (blue in Fig. 1A and 1B). These Dq values were ~30 and ~25% of the wild-type Dq values for seeds and seedlings, respectively. Thus, disruption of the alt-EJ pathway showed more impact on the seedling survival than that of the c-NHEJ pathway (Fig. 2). This is consistent with the previous suggestion that carbon-ion-induced DSBs in seedlings are repaired mainly by alt-EJ [1]. These results suggest that, regardless of the same $^{12}C^{5+}$ irradiation, plants use distinct DSB repair pathways according to the physiological status of the irradiated materials.

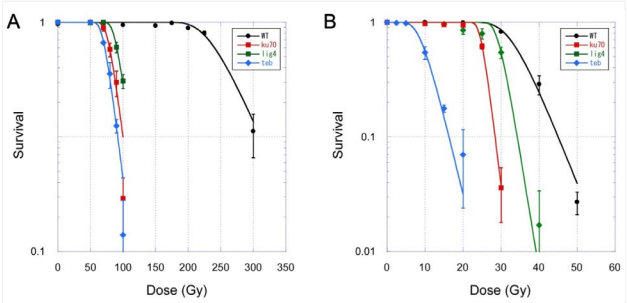

Fig. 1 Involvement of DNA double-strand break repair genes in survival after the irradiation of seed and seedlings.
Sensitivity of the seeds (A) and seedlings (B) to $^{12}C^{5+}$ ion beams are shown for wild-type (WT), *ku70*, *lig4*, and *teb*.

Fig. 2 Seedling-irradiated *ku70* (top) and *teb* (bottom) plants after 20 Gy irradiation of $^{12}C^{5+}$ ion beams. Photos at the 10th day after irradiation are shown.

Acknowledgments

This work was partially supported by JSPS KAKENHI 19K12333 and 16H06279.

References

[1] S. Kitamura *et al*., QST Takasaki Annu. Rep. 2023, **QST-M-52** 55 (2025)

3 - 08 The model liverwort *Marchantia polymolpha* partially relies on homologous recombination to repair DNA double-strand breaks

M. Teranishi [a)] and A.N. Sakamoto [b)]

[a)] Graduate School of Life Sciences, Tohoku University
[b)] Department of Quantum-Applied Biosciences, QST

Introduction

The model liverwort *Marchantia polymorpha* is a spore-forming nonvascular plant, belonging to a group of the first land plants like the model moss *Physcomitrium patens*. *P. patens* has been shown to be hyperresistant to γ-irradiation [1] and its radioresistance is completely diminished when *PpRAD51B* gene is disrupted [2]. The RAD51B is a one of the RAD51 paralogues which are conserved in both animals and plants and promotes homologous recombination. Thus, *P. patens* relies heavily on homologous recombination to repair γ-ray induced DNA double-strand breaks [2] unlike vascular plants. However, it remains unclear if the *RAD51B*-dependency is a common characteristic of basal land plants.

To examine if the function of *RAD51B* is conserved in *M. polymorpha*, we have created a *MpRAD51B*-disrupted plant by genome editing and measured the resistance to γ-irradiation.

Experimental

M. polymorpha male accession recombinant inbred line of Takaragaike-1 (Rit-1) was kindly provided by Dr. Takayuki Kohchi [3]. The nucleotide sequence of *MpRAD51B* was obtained from the Phytozome 14 (https://phytozome-next.jgi.doe.gov/). To knock out the *MpRAD51B,* a DNA fragment consist of MpU6-1 promoter and guide RNA was synthesized and cloned into the Cas9-expressing plasmid pMpGE013 [4]. The plasmid was introduced into Rit-1 by *Agrobacterium* infection to induce Cas9-digestion. The obtained hygromycin-resistant plants were further screened for disruption of *RAD51B* allele by genomic PCR. The *rad51b* plant carrying one base pair insertion at the digestion site was back-crossed to a female accession Rit-2 to remove the Cas9-expressing transgene.

Gemmae or vegetative reproductive tissues of Rit1 and *rad51b* were placed on the half-strength Gamborg's B5 medium and were kept cool (<10˚C) in dark for about 24 h. The plants were moved to a growth chamber and grown under white light (80-90 μmol photons/m^2/s) for another 24 h at 23-25˚C. The plants were exposed to ^{60}Co γ-rays at Co-60 irradiation facility and grown in a growth chamber for another 8 days. The size of thallus or leaf-like body was measured by Image J.

Results and Discussion

Thirty each of Rit-1 and *rad51b* gemmae placed on the medium were exposed to 30 to 120 Gy/h of γ-rays for 0.5 h. After 8 days, the vertical image of plants was photographed, and analyzed by image J. The size of plants was decreased depending on the γ-ray dose in both lines (Figure 1). The dose that reduced the size of Rit-1 plants by half was about 30 Gy, contrasting with the hyperradioresistance of *P. patens*, in which the dose causing a 50% reduction in dry weight was about 350 Gy.

At the dose of 15 Gy, the avarage plant size of *rad51b* was significantly smaller than that of Rit-1, suggesting that the MpRAD51B is important for the repair of γ-ray induced DNA double-strand breaks. However, the reduction was only 15% to the wild type (Rit-1) plants. This result suggests that *M. polymorpha* exhibits the lower dependence on homologous recombination than *P. patens*, reminiscent of flowering plants.

Our results suggest that the evolutional diversity of DNA repair activities along with the history of land plant lineage, which could provide a hint for other research fields such as cancer research.

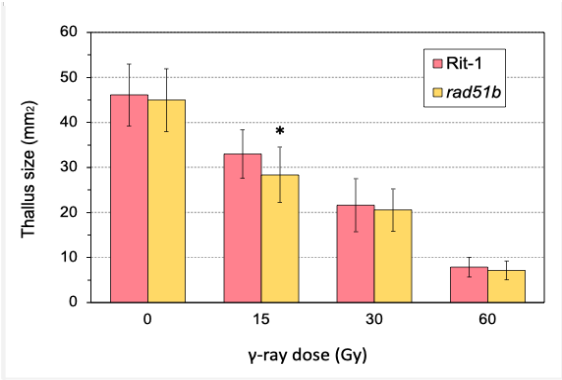

Fig.1 Effect of γ-irradiation on the growth of wild type (Rit1) and *rad51b* thalli of *M. polymorpha*. *: p<0.01

Acknowledgments

We thank Takayuki Kohchi for kindly providing us with *M. polymorpha* plants and plasmids. We also thank to Eri Yokozuka for γ-ray calibration.

References

[1] Y. Yokota *et al*., Genes **9**, 76 (2018). DOI: 10.3390/genes9020076
[2] A.N. Sakamoto *et al*., DNA Repair **152** (2025). DOI: 10.1016/j.dnarep.2025.103881
[3] Y. Tomizawa *et al*., Plant Cell Physiol. **64**, 1343 (2023). DOI: 10.1093/pcp/pcad117
[4] S.S. Sugano *et al*., PLoS One **13**, e0205117 (2018). DOI: 10.1371/journal.pone.0205117

3 - 09 Production of Auger-electron-emitting ^{103m}Rh via a ^{103}Pd/^{103m}Rh generator

T. Ohya [a], J. Ichinose [b], K. Nagatsu [b], Y. Sugo [b], N. S. Ishioka [b], H. Watabe [c], M. Itoh [c], K. Minegishi [a] and M-H. Zhang [a]

[a] Department of Advanced Nuclear Medicine Sciences, QST
[b] Department of Quantum-Applied Biosciences, QST
[c] Research Center for Accelerator and Radioisotope Science, Tohoku University

Introduction

In targeted radionuclide therapy, Auger and Coster–Kronig electrons show high linear energy transfer (~26 keV/μm) with a very short range (<0.5 μm). Therefore, they are promising for cancer therapy (Auger therapy), especially for micrometastases and disseminated tumors. Bernhardt et al. quantitively assessed the use of different radionuclides in Auger therapy to avoid excess exposure to healthy tissue [1]. ^{103m}Rh ($T_{1/2}$ 56 min, IT 100%) was selected as one of the top five candidates for Auger therapy. The feasible supply of ^{103m}Rh for clinical application should be achieved by a generator because of its short half-life. However, we cannot reproduce these generators presented in the past because the resins used as adsorbents for ^{103}Pd ($T_{1/2}$ 17 d, EC 100%) have been discontinued. The objective of this study was to develop a feasible generator with comparable performance to those reported previously.

Experimental

A 100-mg rhodium pellet was irradiated at the AVF cyclotron of Takasaki Ion Accelerators for Advanced Radiation Applications (TIARA) at QST (p-18 MeV, 5 μA) or the Cyclotron and Radioisotope Center (CYRIC) at Tohoku University (p-14 MeV, 4 μA). The energy of the proton beam was adjusted to 12 MeV on the target. The separation of no-carrier-added ^{103}Pd from a rhodium target has been reported elsewhere [2]. 3 mL of each resin (IRA410, IRA904, SA11AL, SA20) was added to a reservoir (Bond Elute Reservoir-2 Frits, Agilent Technologies, Santa Clara, USA), and then 20 mL of 0.1 M HCl was loaded onto the column at a flow rate of 0.5 mL/min for conditioning. Then, ^{103}Pd-HCl dissolved in 2–5 mL of 0.1 M HCl solution was loaded onto the reservoir at a flow rate 0.2 mL/min. Subsequently, 10 mL of 0.1 M HCl solution was loaded to remove the untrapped ^{103}Pd and ^{103m}Rh in the reservoir. For milking, 6 mL of 0.1 M HCl was loaded with a flow rate of 0.5 mL/min. The measurement of the yield of ^{103m}Rh and contamination of ^{103}Pd in the ^{103m}Rh fraction were conducted using a liquid scintillation counter and HPGe-detector [3].

Results and Discussion

The activity of ^{103}Pd in each generator was about 10 MBq. Figure 1 shows the typical gamma spectra of the generator using SA11AL before milking and the ^{103m}Rh product. Clear gamma peaks of ^{103}Pd above 40 keV were observed, although the peaks of 20–40 keV were only discernible in the ^{103m}Rh product.

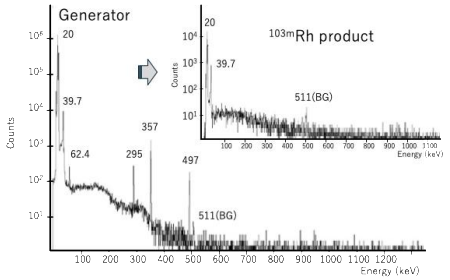

Fig. 1 Gamma spectra of the ^{103}Pd/^{103m}Rh generator using SA11AL and the ^{103m}Rh product.

We compare our results to those of previous reports in Table 1. The reported operation times were from 5 to 20 min. The activity of the product should have decayed during the milking period. Therefore, we estimated the actual yield considering the decrease due to the operation time; these values are shown in parentheses. The generator with SA11AL showed a yield of 39% (actual yield: 33%) and a ^{103}Pd impurity of 0.29%. This generator was comparable to those previously reported, although the radionuclide impurity was slightly higher.

Table 1
Comparison with previously reported ^{103}Pd/^{103m}Rh generators.

Report	Adsorbent (s)	Eluent	Yield (%)	Impurity (%)	Operation time
Bernhard et al. (1970)	Dowex 2x8, IRA93, DMG	0.2 M HCl 5–10 mL	20–25 (24)	<0.1	5–6 min
Berk (1971)	Dowex 2x8, IRA938, IRA400, Chelex-100	saline 20 mL	40 (31)	0–1	<20 min (×0.78)
Mamadaliev et al. (1978)	Dowex 2x8	0.2 M HCl 20 mL	35 (31)	0.003–0.3	N.A. < 10–20 min (×0.88)
Jensen et al. (2020)	16aneS4	0.1 M HCl 1 mL	5.8	0.72	N.A. < 1 min?
This work	SA11AL, SA20A, IRA410, IRA904	0.1 M HCl 6 mL	39 (33)	0.29	14 min (×0.84)

Acknowledgments

We thank the staff of RIPF, TIARA and CYRIC for their support. ^{103}Pd was supplied by Supply Platform of Short-lived Radioisotopes, supported by JSPS Grant-in-Aid for Transformative Research Areas, Grant Number 22H04924. This work was supported by JSPS KAKENHI, Grant Number JP23K07123.

References

[1] P. Bernhardt *et al.*, Acta Oncol. **40**, 602 (2001). DOI: 10.1080/028418601750444141
[2] T. Ohya *et al.*, Radiochim. Acta **110**, 251 (2022). DOI: 10.1515/ract-2021-1117
[3] T. Ohya *et al.*, Radiochim. Acta **112**, 37 (2024). DOI: 10.1515/ract-2023-0238

3 - 10 Development of a compact multiprobe system for monitoring radioisotope tracers in plant bodies

Y. Nagao [a)], M. Yamaguchi [a)], Y.-G. Yin [a)], N. Suzui [a)], Y. Miyoshi [a)], Y. Noda [a)], K. Enomoto [a)], M. Tsuda [a, b)], T. Yabe [a)], H. Watabe [a, b, c)] and N. Kawachi [a, d)]

[a)] Department of Quantum-Applied Biosciences, QST, [b)] Graduate School of Biomedical Engineering, Tohoku University, [c)] Research Center for Accelerator and Radioisotope Science, Tohoku University, [d)] Radiation Science, Medicine and Drug Development, & Industrial Applications for Radiation, F-REI

Introduction

Noninvasive monitoring of radioactive tracers at multiple points in plant bodies is essential for understanding how plants absorb and use the various elements present in the soil and atmosphere. Radioisotope tracer imaging, such as positron emission imaging, are powerful tools for analyzing tracer distribution and movement in a given field of view (FOV). However, the FOV of emission imaging systems sometimes cannot cover the whole plant body. On the other hand, owing to the recent advances of silicon photomultipliers (SiPMs), fabricating compact detector heads has become possible. To overcome the FOV limitation, we developed a compact multiprobe system (CMPS) for monitoring radioactive tracers in plant bodies at multiple points, including points separated by large distances, using compact detector heads with SiPMs.

Experimental

The CMPS operates as the single mode for single-photon or beta-ray emitting tracers and as the coincidence mode for positron-emitting tracers. The CMPS has 16 detector heads. Figure 1 shows a photograph of some of the detector heads. Each detector head consists of a 10 mm cubic high-resolution gadolinium aluminum gallium garnet (HR-GAGG) scintillator directly coupled to a SiPM.

We performed demonstration experiments for monitoring a ^{11}C tracer in strawberry stems. Four pairs of detector heads were assigned and fixed to strawberry plant stems. The distance between the two detector heads of each pair was approximately 10 mm. A ^{11}C-labeled carbon dioxide ($^{11}CO_2$) tracer was produced by bombarding pure nitrogen gas with 10-MeV protons from the cyclotron at Takasaki Institute for Advanced Quantum Science, QST, Gunma, Japan. The $^{11}CO_2$ was fed to a leaf of the plant with air, which resulted in the leaf fixation of 158 MBq. The measurement started 29 min after tracer feeding and continued for 164 min [1].

Results and Discussion

Figure 2 shows a two-dimensional energy spectrum of the data collected by a pair of detector heads as an example. The dominant events were the coincidence events of Compton scattering and subsequent photoabsorption of a single 511-keV gamma ray rather than photoabsorption, Compton scattering, or both of a pair of annihilation 511-keV gamma rays. These dominant events contained both signal events (from the stem between the two detector heads) and noise events (from the other parts of the plant, especially the leaf to which the tracer was fed), which can be eliminated by energy-window filtering.

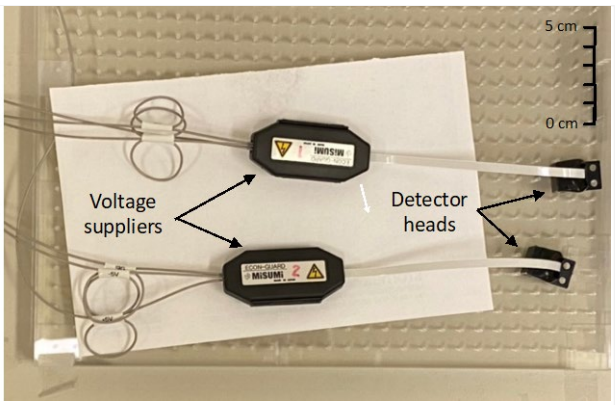

Fig. 1. Photograph of some of detector heads.

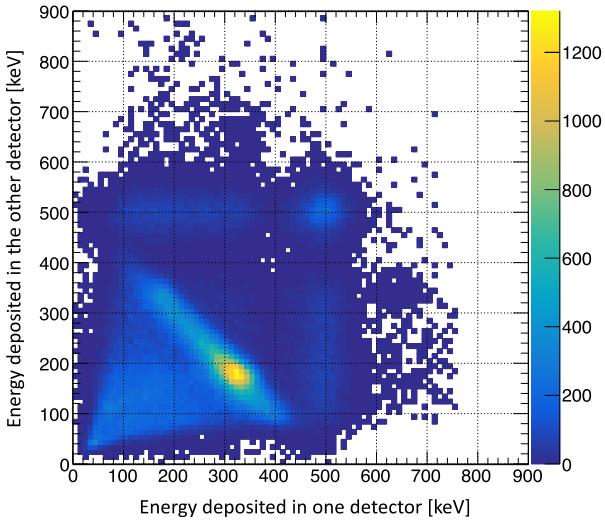

Fig. 2. Two-dimensional energy spectrum of the data collected by a pair of detector heads.

Acknowledgments

This work was supported in part by JSPS KAKENHI Grant Numbers JP16K15351, JP18K14556, JP20K15632, JP21K15855 and JP25K09351.

References

[1] Y. Nagao *et al.*, J. Instrum. **19**, P04023 (2024). DOI: 10.1088/1748-0221/19/04/P04023

3 - 11 Visualization of nickel (Ni) distribution in roots of oilseed rape plants *(Brassica napus)* by in-air micro-PIXE (Particle Induced X-ray Emission) analysis

S. Nakamura [a)], M. Tashiro [a)], T. Yuzawa [a)], A. Shinozawa [a)], K. Sato-Izawa [a)], R. Yamagata [b)], Y. Ishii [b)], T. Satoh [b)], Y. Noda [c)], Y. Miyoshi [c)], K. Enomoto [c)], Y.-G. Yin [c)], N. Suzui [c)] and N. Kawachi [c)]

[a)] Department of Bioscience, Faculty of Life Sciences, Tokyo University of Agriculture
[b)] Department of Advanced Quantum Beam Technology, QST
[c)] Department of Quantum-Applied Biosciences, QST

Introduction

Nickel (Ni) is recognized as an essential micronutrient for higher plants. The amount of Ni required for optimal plant growth is limited by an upper threshold. Therefore, in soils with high concentrations of Ni, such as serpentine soils, plants may develop nickel toxicity. To enable agriculture in such soils, it is necessary to impart Ni tolerance to plants. To achieve this, it is essential to elucidate the molecular mechanisms of Ni transport in plants and regulate them. However, these mechanisms have not been fully elucidated. Clarifying Ni distribution in root tissues contributes to understanding molecular mechanisms of Ni radial transport within root tissues. In-air micro-PIXE analysis allows us to visualize the distribution of various elements within tissue samples [1, 2]. Therefore, we used in-air micro-PIXE analysis to visualize the tissue distribution of nickel (Ni) in the roots of oilseed rape plants.

Experimental

Test plants (*Brassica napus* L. var. Westar) were grown hydroponically in a fully controlled environment [3]. In the present study, 100 μM of $NiSO_4$ was added to the nutrient solution for seven days prior to harvest to visualize the tissue distribution of Ni in the roots of the test plants. This concentration of Ni has been reported to induce Ni toxicity in *Brassica* plants [4]. The harvested plant roots were immediately embedded in clear resin (Cryomatrix, Epredia) for preparation of frozen sections and stored at -80°C. Cross sections were prepared for micro-PIXE analysis using a sectioning device (CM1520, Leica Biosystems). After slicing the samples to a thickness of 40 μm, the sections were immediately heated on a hot plate (NHP-45N, NISSIN) to remove excess moisture. Microscopic observations were performed to select the samples for in-air micro-PIXE analysis.

An in-air micro-PIXE analysis was performed at TIARA (Takasaki Ion Accelerators for Advanced Radiation Application) in Takasaki Institute for Advanced Quantum Science. Prepared section samples were irradiated with a 3-MeV proton beam for 60 min. The specific X-rays generated by irradiated proton beam were then detected. The distribution and intensity of several elements including Ni were determined from the detected X-ray.

Results and Discussion

Figure 1 indicates a microscopic observation of the prepared sections and the tissue distribution of Ni. In this study, we were able to visualize distribution of Ni in the roots of oilseed rape plants (Fig.1B and 1D). Under the present treatment conditions, Ni exhibited a similar distribution pattern in both the upper and apical regions of the root (Fig. 1B and 1D). These results suggest that an in-air micro-PIXE could serve as a powerful tool for elucidating the mechanisms that are controlling Ni behaviors in plant roots.

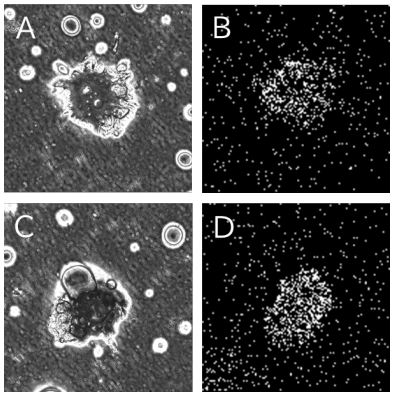

Fig. 1 An in-air micro-PIXE analysis in root cross sections prepared from roots of oilseed rape plants treated with 100 μM Ni for seven days. (A), (C) Microscopic observation, Tissue distribution of Ni in the upper parts (B) and apical region (D).

Acknowledgments

This research was partially funded by a Grant-in-Aid for Fukushima Institute for Research, Education and Innovation (F-REI) (JPFR24040101).

References

[1] T. Sakai *et al*., Nucl. Instrum. Methods Phys. Res. B. 190, 271-275 (2002). DOI:10.1016/S0168-583X (02)00469-X
[2] P.M. Kopittke *et al*., Plant Physiol. **182**, 1869 (2020). DOI:10.1104/pp.19.01306
[3] S. Nakamura *et al*., Plant Sci. **283**, 424 (2019). DOI: 10.1016/j.plantsci.2018.10.018
[4] A.M. Masidur *et al*., Photosynthetica. **45**, 139 (2007). DOI: 10.1007/s11099-007-0022-4

3 - 12 3D secondary electron bremsstrahlung imaging for carbon-ion therapy range verification: A Monte Carlo simulation study

M. Tsuda [a, b], M. Yamaguchi [a], T. Yabe [a], Y. Nagao [a], N. Kawachi [a] and H. Watabe [a, b, c]

[a] Department of Quantum-Applied Biosciences, QST
[b] Graduate School of Biomedical Engineering, Tohoku University
[c] Research Center for Accelerator and Radioisotope Science, Tohoku University

Introduction

Carbon-ion radiotherapy provides precise dose localization for cancer treatment. However, uncertainties in beam range necessitate range verification. Current range verification methods include positron emission tomography (PET) and prompt gamma imaging (PGI). PET is limited by biological washout, while PGI is limited by low detection efficiency. Secondary-electron-bremsstrahlung (SEB) imaging [1] detects prompt X-rays generated when secondary electrons interact with atomic nuclei. The SEB radiation is of relatively low energy, which facilitates detection, and it is not affected by biological washout. Previous studies have demonstrated the feasibility of 2D SEB imaging, but its 3D capability has not been investigated. This study aims to evaluate the feasibility of 3D SEB imaging for range verification in carbon-ion therapy using Monte Carlo simulations [2].

Simulation

Monte Carlo simulations were performed using Particle and Heavy Ion Transport code System (PHITS), version 3.27, to evaluate the feasibility of 3D SEB imaging [3]. A cylindrical acrylic target (50 mm radius, 150 mm height) was modeled. 24 pinhole X-ray cameras were arranged circumferentially around the target at 15° intervals, with 300 mm from the beam axis (Fig. 1). Each camera was equipped with a 5-mm-diameter pinhole with a 53° opening angle, coupled to a 0.5-mm-thick YAP(Ce) scintillator (20 × 20 mm). Carbon-ion beams were simulated at 4 energies (229.5, 236.7, 240.9, and 243.7 MeV/u) with lateral offsets of 0, 2, 5, and 10 mm from the central axis. The beam was modeled as a Gaussian distribution with a full width at half maximum (FWHM) of 5 mm. SEB photons were directly generated using a subprogram and detected within an energy window of 30–60 keV. Image reconstruction was performed using filtered back projection with Gaussian smoothing (FWHM = 30.3 mm), resulting in 44 × 44 × 44 voxel volumes with a voxel size of 4.3 mm.

Results and Discussion

The reconstructed 3D SEB images clearly visualized the depth and lateral distributions of the carbon-ion beam (Fig. 2). Spatial blurring was observed due to the limited resolution of the detection system (52.2 mm FWHM). Range estimation accuracy had maximum errors of 4.2 mm for individual slice profiles and 1.3 mm for summed profiles obtained by integrating across orthogonal planes. Lateral beam position estimation had errors up to 4.7 mm for the individual profiles and 2.9 mm for the summed profiles. The summed profiles consistently provided superior accuracy because of improved photon statistics. These results demonstrate the fundamental feasibility of 3D SEB imaging for range verification in carbon-ion therapy.

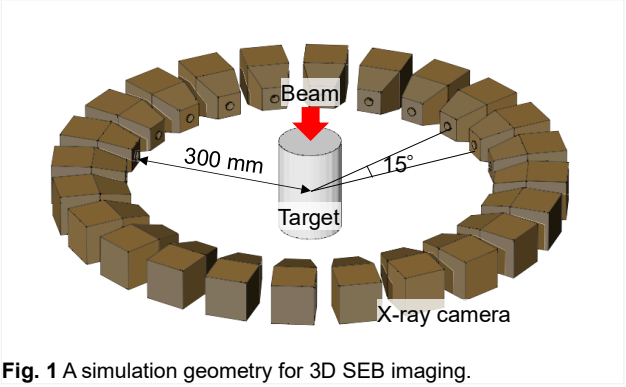

Fig. 1 A simulation geometry for 3D SEB imaging.

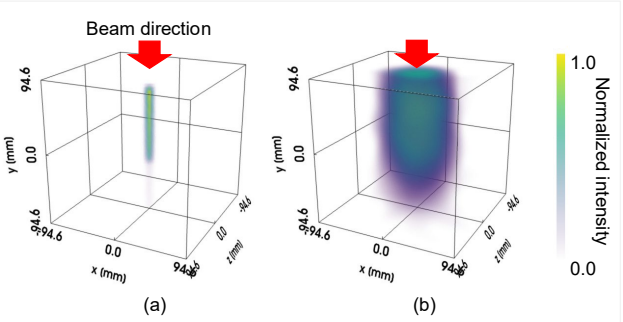

Fig. 2 3D SEB images for the 243.7 MeV/u beam: (a) ground truth distribution obtained from Monte Carlo simulation and (b) reconstructed image.

Acknowledgments

This research was conducted with the supercomputer HPE SGI8600 at the National Institutes for Quantum Science and Technology. This work was supported by the Japan Society for the Promotion of Science (JSPS) KAKENHI (Grant Number JP23KJ0221 and JP23K28462).

References

[1] M. Yamaguchi *et al.*, Phys. Med. Biol. **57**, 2843 (2012). DOI: 10.1088/0031-9155/57/10/2843
[2] M. Tsuda *et al.*, Jpn. J. Appl. Phys. (2025). (accepted) DOI: 10.35848/1347-4065/ae0776
[3] T. Sato *et al.*, J. Nucl. Sci. Technol., **61**, 127 (2024). DOI: 10.1080/00223131.2023.2275736

3 - 13 Effects of carbon-ion irradiation on the hatching of the nematode *Caenorhabditis elegans*

M. Suzuki and T. Funayama

Department of Quantum-Applied Biosciences, QST

Introduction

The damage caused to crops by plant-parasitic nematodes is significant. Crop diseases are a major threat to food security, but their rapid identification remains difficult in many parts of the world [1]. Plant-parasitic nematodes are particularly troublesome pests that are often difficult to identify, and completely suppressing their spread requires considerable time. Furthermore, reducing the use of environmentally harmful chemical pesticides to control them has become an urgent issue.

In order to address this issue, we plan to use radiation-induced sterility technology to control plant-parasitic nematodes. This study aimed to analyze the sterilising effects of carbon ions on nematodes to obtain foundational data. The first step of this study involved using the nematode *Caenorhabditis elegans* as a model organism. This species is well-established, non-parasitic and easy to handle in a laboratory setting. It is also known to be radiation-resistant [2].

Experiments

(1) Strains and cultures

The nematode *C. elegans* hermaphrodites of wild-type strain N2 were grown at 20°C on an agar plate with bacterial lawn (*Escherichia coli* OP 50) as a food source. Age-synchronized and well-fed young adults 2.5 days after hatching were used for all experiments.

(2) Carbon ion whole-body irradiation at TIARA

Animals on an agar plate with bacterial lawn were irradiated with a carbon-ion (C^{6+}, 320 MeV) broad beam at the HY1 port of TIARA. Four doses, 25 Gy, 50 Gy, 100 Gy, 150 Gy; and 0 Gy as a control, were irradiated independently.

(3) Incubation of irradiated parental individuals

After irradiation, the animals were individually picked up from the plates using a platinum wire picker and transferred to the Day 1 plates containing nematode growth medium (NGM) with a bacterial lawn. This procedure was repeated for five parental animals at every dose. One day (24 hours) after irradiation, the animals were transferred from the Day 1 plates to new NGM plates with a bacterial lawn (the Day 2 plates). Then, two days (48 hours) after irradiation, the animals were transferred from the Day 2 plates to new NGM plates with a bacterial lawn (the Day 3 plates). The number of eggs laid on the Day 1, Day 2 and Day 3 plates was counted visually under a microscope two, three and four days after irradiation, respectively. Furthermore, the number of hatchlings was counted one day later.

(4) The numbers of egg-laying and F1-generation hatching were counted after irradiation

For eggs laid on each day after irradiation (Day 1, Day 2 and Day 3), the number of hatched eggs was divided by the number of eggs laid by each irradiated parent to calculate the hatching rate. The hatching rate values for eggs laid by each of the five animals were averaged at every dose.

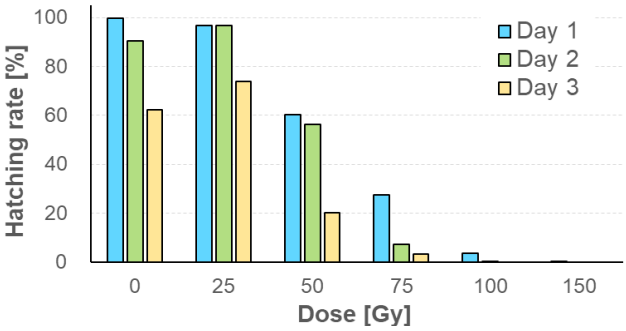

Fig.1 The hatching rate of the F1 generation spawned from irradiated parental *C. elegans*.

Results

Figure 1 shows the hatching rate of the F1 generation from animals that were irradiated with carbon ions. Preliminary results from a single experiment showed that the hatching rate decreased in a dose-dependent manner for eggs laid at any time during the following periods: immediately after irradiation; one day after irradiation; and two days after irradiation. It was found that 25 Gy was insufficient to reduce the hatching rate, whereas 150 Gy prevented hatching completely. Furthermore, eggs laid on Day 1 (light blue), which were either mature or nearly mature at the time of irradiation, hatched at a higher rate than those laid on Days 2 (yellow-green) and 3 (yellow), which were immature.

In the future, we will investigate the effects of whole-body carbon-ion irradiation on plant-parasitic nematodes.

Acknowledgments

We thank the Caenorhabditis Genetic Center of the University of Minnesota, which is funded by the NIH Office of Research Infrastructure Programs (P40 OD010440), for providing strains of *C. elegans* and *E. coli*. We thank the crew of the cyclotron of TIARA at TIAQS for their kind support for providing fine beams, and members of our project for valuable discussions.

References

[1] S.P. Mohanty *et al*., Front. Plant Sci. **7**,1419 (2016). DOI: 10.3389/fpls.2016.01419

[2] T. Sakashita *et al*., Biol. Sci. Space **26**, 7 (2012). DOI: 10.2187/bss.26.7

4 - 01 Ion beam induced luminescence and particle induced X-ray emission analyses of europium complexes in di(2-ethylhexyl)phosphoric acid solvent

M. Nakahara [a)], R. Yamagata [b)], Y. Ishi [b)] and M. Koka [c)]

[a)] Nuclear Fuel Cycle Engineering Laboratories, JAEA
[b)] Department of Advanced Quantum Beam Technology, QST
[c)] Beam Operation Co., Ltd.

Introduction

To recover trivalent minor actinides (MAs) such as Am and Cm from high-level radioactive liquid, solvent extraction and extraction chromatography have been studied with various extractants [1]. The determination of complex structures is important for efficient stripping and elution of MAs. Although X-ray absorption fine structure (XAFS) is generally used to evaluate complex structures, only one-dimensional data is obtained. Therefore, ion beam induced luminescence (IBIL) is proposed as an additional method to evaluate the complex structure and support the XAFS data. Collecting extensive IBIL datasets for various extractants is important for evaluating the complex structure. In a previous study [2], the IBIL of some adsorbents with various extractants was measured. In this study, the IBIL data for organic solvents were obtained to enable comparison with adsorbents and to examine extractant dependence. In addition, particle induced X-ray emission (PIXE) was analyzed because PIXE data provide valuable information for confirming the composition of the complexes.

Experimental

Di(2-ethylhexyl)phosphoric acid (HDEHP) is one of the extractants [3] for MA recovery and was used with diluted *n*-dodecane. Nonradioactive $Eu(NO_3)_3{\cdot}6H_2O$ powder, serving as a simulated MA, was dissolved in HNO_3 solution. The Eu nitrate solution was shaken with the HDEHP solvent, and then separated from the aqueous phase. The obtained organic solvents were placed in acrylic cases and sealed with Kapton® tape. At TIARA, a 3-MeV H^+ ion beam was utilized on the light-ion microbeam line connected to a 3-MV single-ended accelerator. The Ion Luminescence Microscopic Imaging and Spectroscopy (ILUMIS) system was developed to measure the IBIL and PIXE spectra simultaneously [4]. The samples were mounted on a revolving sample stage. The IBIL spectra of Eu complexes were measured using ultraviolet–visible spectrophotometry. The exposure time for IBIL analysis was 6.5 s, and PIXE was measured for 15 min.

Results and Discussion

Fig. 1 shows the PIXE spectrum of Eu complexes in HDEHP solvent. The P K_α line was detected at approximately 2010 eV, originating from the HDEHP solvent. A peak assigned to the Eu L_α line was observed at around 5850 eV. Two peaks at around 6460 and 6840 keV were attributed to the Eu L_β lines. Eu was detected in the sample, indicating extraction of Eu with HDEHP by PIXE analysis.

The IBIL spectra of Eu complexes in HDEHP solvent were measured simultaneously. A peak around 592 nm was observed and assigned to the $^5D_0 \rightarrow {}^7F_1$ transition. Two peaks appeared at 611 and 619 nm, corresponding to the $^5D_0 \rightarrow {}^7F_2$ transition. A peak near 700 nm was attributed to the $^5D_0 \rightarrow {}^7F_4$ transition. The spectrum of the HDEHP solvent is similar to that of the HDEHP adsorbent [2]. In contrast, the spectral shapes of Eu complexes in HDEHP solvent differed from those in *N*,*N*,*N*′,*N*′-tetraoctyl diglycolamide (TODGA) solvent [5]. Although TODGA complexes contain NO_3, HDEHP does not form complexes with NO_3 during Eu^{3+} extraction. Therefore, structural differences in Eu complexes may cause variations in the IBIL spectra. The influence of chemical structure on the IBIL spectra will be further investigated.

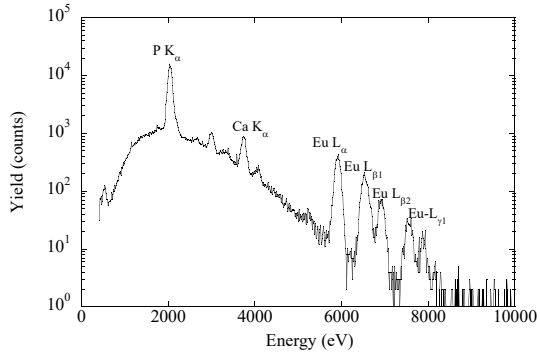

Fig. 1 PIXE spectrum of Eu complexes in HDEHP solvent

References

[1] P. Baron *et al*., Prog. Nucl. Energy **117**, 103091 (2019). DOI: 10.1016/j.pnucene.2019.103091
[2] M. Nakahara *et al*., Nucl. Instrum. Methods Phys. Res. B **542**, 144 (2023). DOI: 10.1016/j.nimb.2023.06.012
[3] B. Weaver *et al*., J. Inorg. Nucl. Chem. **30**, 263 (1968). DOI: 10.1016/0022-1902(68)80089-2
[4] W. Kada *et al*., Nucl. Instrum. Methods Phys. Res. B **318**, 42 (2014). DOI: 10.1016/j.nimb.2013.06.057
[5] M. Nakahara *et al*., Nucl. Instrum. Methods Phys. Res. B **554**, 165449 (2024). DOI: 10.1016/j.nimb.2024.165449

4 - 02 PIXE/PIGE analysis of the caries-preventive effect of fulvic acid in combination with titanium fluoride

K. Okuyama [a], Y. Matsuda [b], H. Yamamoto [c], T. Saito [b], M. Hayashi [c], Y. Tamaki [a], T. Sato [d], R. Yamagata [d], and Y. Ishii [d]

[a] Asahi University School of Dentistry,
[b] School of Dentistry, Health Sciences University of Hokkaido,
[c] Graduate School of Dentistry, Osaka University,
[d] Department of Advanced Quantum Beam Technology, QST

Introduction

Focusing on the chelating properties and matrix metalloproteinase (MMP) inhibitory activity of fulvic acid, a natural compound extracted from humic substances, previous studies have suggested its potential to inhibit dentin demineralization [1]. Meanwhile, titanium fluoride (TiF_4) also demonstrates dentin demineralization inhibition [2]. This study aimed to evaluate the demineralization-inhibiting effect of dentin when combined with TiF_4 using micro-PIXE/PIGE analysis.

Materials and Methods

Solutions prepared for this study included 1% fulvic acid (1F), 0.1% fulvic acid (01F), 0.5% TiF_4 alone (T), and TiF_4 combined with 1% or 0.1% fulvic acid (1FT and 01FT, respectively). Deionized water served as the control (CO).

Bovine cervical dentin sections approximately 500 μm thick were prepared, and a portion was coated with nail varnish to form a defined window for demineralization. The specimens were initially demineralized for 24 hours in a demineralization solution (pH 4.5) to create the demineralized area. Subsequently, half of the demineralized area was coated, and the specimens underwent a 4-week pH cycling treatment involving alternating demineralization and remineralization (pH 7.0) stages. Each specimen was immersed in the corresponding treatment solution for 10 minutes once per week.

After cycling, the specimens were analyzed using the micro-PIXE/PIGE system at QST Takasaki. Calcium (Ca) and fluorine (F) distributions were recorded, and lesion depth was defined from the point corresponding to 5% to 95% of the Ca content relative to sound dentin. Demineralization depth and mineral loss were calculated, and statistical analysis was performed using the Kruskal-Wallis and Steel-Dwass tests at a significance level of 5%.

Results

The fulvic acid groups (1F, 01F, 1FT, 01FT) showed significantly smaller lesion depths and lower mineral loss compared with the control group. The TiF_4 group also demonstrated reduced values relative to the control, although the difference was not statistically significant (Fig. 1). In terms of F incorporation, TiF_4-containing groups (T, 1FT, 01FT) exhibited significantly higher F uptake than groups without TiF_4 (1F, 01F, CO) (Fig.2).

Discussion

The results suggest that fulvic acid contributes to the inhibition of dentin demineralization, possibly through its buffering capacity, which may reduce the severity of acid challenges. TiF_4 alone tended to suppress demineralization, but its strong acidity (approximately pH:1) may have induced surface dissolution during treatment, reducing its overall effectiveness. The combined application of fulvic acid and TiF_4 demonstrated both inhibition of demineralization and enhanced fluoride incorporation, indicating a possible synergistic effect. This study indicated that fulvic acid, either alone or in combination with titanium fluoride, inhibited dentin demineralization.

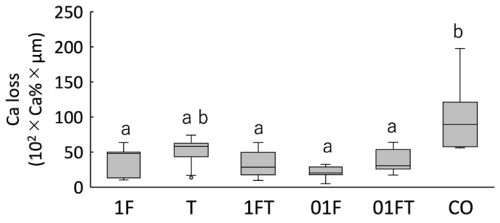

Fig.1 The difference in demineralization (Ca loss) before and after the pH cycle. Same letters indicate no significant differences ($p>0.05$).

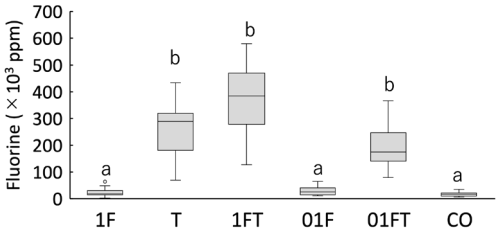

Fig.2 Cumulative fluorine concentration up to 200 μm from the surface after the pH cycle. Same letters indicate no significant differences ($p>0.05$).

References

[1] Okuyama K *et al.*, J. J. Dent. Mater. **43** (Special 82), 101 (2024).
[2] Okuyama K *et al.*, Dent. Mater. J. **40**(3), 736 (2021).

4 - 03 Density Dependence of irradiation defect for hydrogen isotope transport in advanced plasma-facing walls

Y. Oya [a], A. Sanfukuji [b] Y. Hoshino [b], S. Okumura [b] A. Hayakawa [b], K. Miura [b]
T. Nozawa [c], and M. Ando [c]

[a] College of Science, Academic Institute, Shizuoka University
[b] Graduate School of Integrated Science and Technology, Shizuoka University
[c] Department of Fusion Reactor Material Research, QST

Introduction

Tungsten (W) is a candidate material for plasma facing wall (PFW) in DT fusion reactors. W will be exposed to high heat loads and fuel particles such as neutron, deuterium (D) and Tritium (T). These damages will introduce the microstructural changes and lead to degradation of the superior thermo-mechanical properties of W. Alloying W with Tantalum (Ta) and Potassium doping (K-doping) are promising way to improve these properties [1-2]. In addition to thermo-mechanical properties, elucidation of hydrogen isotope behavior in PFW is essential from the perspectives of fuel balance and reactor safety. In this study, hydrogen isotopes behavior for W-Ta and K-doped W was investigated with various damage conditions.

Experimental

Polycrystalline disk W, K-doped W (40 appm), W-1,3,5%Ta (6 mm$^{\phi}$ × 0.5 mm^{t}) made by A.L.M.T. corp., were used in this study. These samples were heat treated at 1173 K for 30 minutes to remove residual hydrogen and surface impurities. After that, 6 MeV Fe^{2+} irradiation was performed to introduce irradiation defects by 3 MV Tandem Accelerator at Takasaki Ion Accelerators for Advanced Radiation Application (TIARA) facility in National Institute for Quantum Science and Technology (QST). The damage level was set up to 1 dpa at R.T. and 773 K. Positron Annihilation Spectroscopy (PAS) by ^{22}Na positron source was used to evaluate the size and density of irradiation defects. 3 keV D_2^+ implantation was performed with ion flux of 1.0×10^{18} D^+ m^{-2} s^{-1} up to the ion fluence of 1.0×10^{22} D^+ m^{-2} at R.T. for Fe^{2+} damaged K-doped W. Thermal Desorption Spectroscopy (TDS) measurement was applied from R.T. to 1173 K with the heating rate of 30 K min^{-1} to evaluate the D retention behavior.

Results and Discussion

Fig.1 shows the summary of positron lifetime for Fe^{2+} damaged W, K-doped W and W-1,3,5%Ta. Comparing W and K-doped W at 1 dpa, K-doped W had low density of the long lifetime component and the long lifetime. Therefore, K-doped W had a low density of large defects and had numerous small defects instead. These defects were also considered to exist stably and require high temperatures for recovery. Comparing W and W-Ta, no difference was observed in the positron mean lifetime. However, the long lifetime component was approximately 100 ps longer, and its proportion was about 10% reduction This result showed

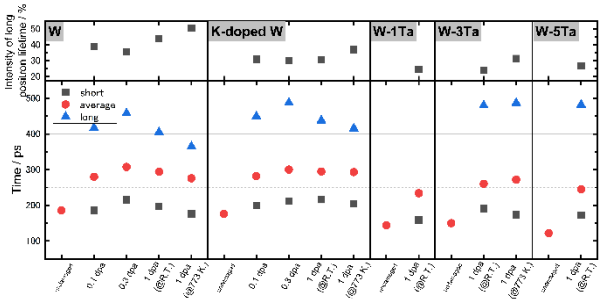

Fig.1 Summary of positron lifetime for W, K-doped W and W-1,3,5%Ta by PAS.

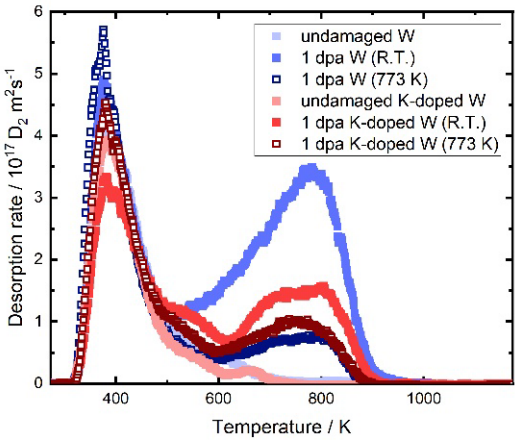

Fig.2 D_2 TDS spectrum for W and K-doped W after D_2^+ implantation.

W-Ta had large defects, but their density was relatively low. No difference was also observed for Ta concentrations ranging from 1% to 5%. This suggested that alloying with Ta, even at low concentrations, had an effect of reducing the generation of large defects. Fig.2 shows D_2 TDS spectrum for Fe^{2+} damaged W and K-doped W after D_2^+ implantation. K-doped W exhibited a smaller D_2 desorption at the higher temperature side than W at 1 dpa and R.T., but the difference at 773 K was slight. D_2 desorption on the higher temperature side was decreased due to the low density of large defects which was showed by PAS.

References

[1] S. Nogami, *et al.*, J. Nucl. Mater. **566**, 153740 (2022). DOI: 10.1016/j.jnucmat.2022.153740.
[2] S. Nogami, *et al.*, Fusion Eng. Des. **202**, 114403 (2024). DOI: 10.1016/j.fusengdes.2024.114403.

4 - 04 Sputtering of phenylalanine thin films bombarded with sub-MeV C_{60} ions at oblique angles of incidence

S. Kinoshita, R. Tsukishima, R. Igarashi, K. Kinomura and K. Nakajima

Department of Micro Engineering, Kyoto University

Introduction

Bombardment with C_{60} ions in the sub-MeV to MeV energy range produces an extremely high sputtering yield [1,2]. It can also form some characteristic anisotropic structures on the bombarded surface, depending on the energy and the angle of incidence [3]. However, there is still much unknown about the sputtering of organic materials when they are bombarded with energetic C_{60} ions. In this work, we examined the sputtering yield and surface topography of phenylalanine thin films bombarded with sub-MeV C_{60} ions at oblique angles of incidence.

Experimental

Samples of phenylalanine thin films were prepared by vacuum evaporation on silicon substrates as follows. A silicon wafer was cut into small pieces as the substrates and they were cleaned in acetone using an ultrasonic cleaner. L-(−)-Phenylalanine (≥ 99.0%, Nacalai Tesque, Inc.) was evaporated at about 240 °C and deposited on the substrates. The thickness of the prepared films was about 100 to 150 nm.

The samples were bombarded with 360 keV C_{60}^{2+} ions extracted from the 400 kV ion implanter of TIARA at QST Takasaki. The C_{60}^{2+} ion beam was scanned over a cross-sectional area of about 7×7 mm^2 to ensure uniform irradiation. The angles of incidence were 70°, 80° and 85° relative to the surface normal. The ion fluences varied from approximately 1×10^{11} to 1×10^{12} ions/cm^2 for each sample.

RBS analysis was performed to determine the sputtering yield. The measurements for the thickness of phenylalanine films were done at both the irradiated and non-irradiated regions for each sample. Sputtering yield was calculated from the relationship between the ion fluence and the difference in film thickness across both regions (sputtered depth). AFM analysis was also performed to clarify the development of surface topography by the bombardment with C_{60} ions.

Results and Discussion

Figure 1 shows an example of a height image of sample surface after the bombardment up to 1.1×10^{12} ions/cm^2 at 80°. A sub-micron scale structure with striations, which are parallel to the component of the C_{60} ion beam in the surface plane, is clearly visible. This structure developed over the ion fluence of about 5×10^{11} ions/cm^2 at the beginning of the bombardment. Development of a similar structure is also observed on the surface bombarded at 70° and 85°.

Figure 2 shows the sputtered depth as a function of the ion fluence for the samples bombarded at 80°. The sputtered depth is approximately proportional to the ion fluence throughout the whole fluence range, although the surface topography undergoes significant change meanwhile. Similar results were also obtained for the samples bombarded at 70° and 85°. This behavior contrasts with that in the case of bombardment at 0° in our previous work, in which the sputtering yield clearly declined with the increasing fluence in the early stage of bombardment. That decline in the sputtering yield was presumably due to significant surface roughening caused by the bombardment. In the present cases of oblique angles of incidence, however, the development of striated surface structures, as seen in Fig.1, does not have much influence on the sputtering yield.

The sputtering yields were approximately 2.8×10^4, 3.1×10^4 and 2.1×10^4 molecules/ion for the bombardment at 70°, 80° and 85°, respectively. They are significantly higher than that for the bombardment at 0°. The angular dependence is similar to that typically observed when inorganic samples are bombarded with monoatomic ions.

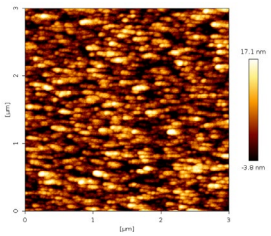

Fig. 1 Height image (3×3 μm^2) of a phenylalanine thin film after bombardment with 360 keV C_{60}^{2+} up to 1.1×10^{12} ions/cm^2 at 80°.

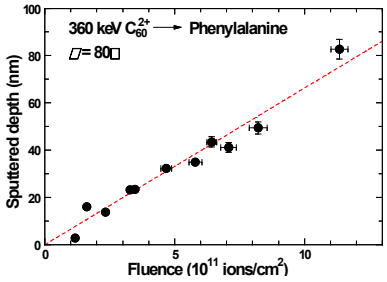

Fig. 2 Sputtered depth of phenylalanine as a function of ion fluence of 360 keV C_{60}^{2+} for bombardment at 80°.

Acknowledgments

This work was partially supported by JSPS KAKENHI Grant Number 24K15594.

References

[1] K. Narumi, *et al*., Quantum Beam Sci. **6**, 12 (2022). DOI: 10.3390/qubs6010012

[2] T. Kitayama, *et al*., Nucl. Instr. Meth. Phys. Res. B **365**, 490 (2015). DOI: 10.1016/j.nimb.2015.07.089

[3] N. Oishi, *et al*., J. Vac. Sci. Technol. A **40**, 063103 (2022). DOI: 10.1116/6.0002073

4 - 05 Gamma-ray irradiation experiment for ITER diagnostic systems in JADA VII

S. Kitazawa, R. Imazawa, E. Yatsuka, K. Nojiri, T. Ushiki, S. Tainaka, M. Fukuda, T. Kikuchi, T. Yokozuka, F. Tsutsumi and Y. Nunoya

Department of ITER Project, QST

JADA (ITER project Japan Domestic Agency) is developing to procure five diagnostic systems, microfission chamber (MFC), poloidal polarimeter (PoPola), Edge Thomson Scattering (ETS), divertor impurity monitor (DIM) and divertor infrared thermography (IRTh).

The reliability under the ITER radiation conditions of relevant equipment to be installed in the vacuum vessel, in the interspaces (IS) between the vacuum boundary and the biological shield and in the port cells (PC) outside the biological shields should be evaluated. In this project, we launched gamma-ray irradiation experiments in QST Takasaki Advanced Radiation Research Institute from 2018. The results obtained in the experiments are used important bases for showing that components can maintain their performances under the ITER radiation environment in the design review for each diagnostic system.

The gamma-ray irradiation experiments on optical components for plasma diagnostics have mainly been conducted by measuring optical density or reflectance before and after irradiations [1, 2, 3]. Regarding electronic equipment for diagnostic systems, we have conducted gamma-ray irradiation durability tests on piezo elements and electrical equipment, observing their characteristics before and after irradiation. As the ITER construction procurement activities progressed and the design was solidified, implementation verification became necessary, so we have launched in-situ experiments in which gamma rays were irradiated while the current was turned on.

For DIM, grass materials, a switching mechanism and cameras were tested. The spectral transmittance of lenses used in the spectrometer within the DIM PC was evaluated for i-line optical glasses (Nikon types 4786 and 7054) and synthetic quartzes (NIFS-A and NIFS-V). The i-line optical glass specimen showed a change in refractive index due to decreased transmittance after 10 kGy irradiation. The synthetic quartz specimen showed no observable changes even after exposure to 1 MGy. A candidate switching mechanism for the dichroic mirror in the pre-spectrometer (THORLABS ELL9K, 4-position slider with SM1 internal threading) was tested under gamma irradiation. A contact failure occurred at 200 Gy, and remote-control operation became impossible at 400 Gy. In-situ observations were performed on four camera models into two groups (#1 and #2, #3 and #4) which will be installed in the PC. The specifications are summarized in Table 1. The irradiation ratios were conducted at 5 Gy/h, because significant image distortions occurred during observations at the initially planned rate of 200 Gy/h. As results, for #1, a malfunction occurred at 293 Gy, for #2, there were no image issues up to 200 Gy, but it failed to reboot, for #3, image issues occurred at 157 Gy, and for #4, image issues occurred at 17 Gy.

Table 1
Specification of tested camera

#	Manufacturer & Model	Pixel Size	Resolution	Sensor Type
1	Teledyne KURO2048B-U3	11 μm	2048×2048 (4.2 MP)	sCMOS
2	Andor iXon Ultra 897	16 μm	512×512 (0.26 MP)	EMCCD
3	Andor Marana 4.2B-11	11 μm	2048×2048 (4.2 MP)	sCMOS
4	Teledyne ProEM-HS-512BX3-G	16 μm	512×512 (0.26 MP)	EMCCD

For IRTh, radiation resistance tests were conducted on the limit switch (IRELEC ALCEN / SW3-R), optical fiber (Ceram Optec / UVNSS 50/70/125/140 CP, NA=0.22), and a custom radiation-hardened encoder (ORE-55, developed by Oshima Prototype Engineering) which are planned for use in the IS. Under gamma irradiation conditions of approximately 1.7 MGy, no performance degradation was observed.

For common items for optical plasma diagnostic systems. The pressure gauge (HBK K-P8AP), intended for use in DIM, ETS, and IRTh, was tested for radiation resistance (pressure durability and measurement accuracy) under gamma irradiation in the PC and the IS. The specimen, which is a different lot of the same model tested last year, was irradiated up to 300 kGy, and its integrity was confirmed. A metal bellows pump (IBS MB-151AL), planned for use in DIM, ETS, and IRTh, was evaluated for radiation resistance in the PC and the IS. No operational abnormalities were observed up to 300 kGy.

Acknowledgments

We would like to thank Naotsugu Nagasawa, Hajime Seito, Yuuto Nagao, Eri Yokozuka, Hiroyuki Okazaki, Shunya Yamamoto and Hiroshi Koshikawa (TARRI) for their cooperation in the irradiation and observation.

References

[1] S. Kitazawa *et al.*, Plasma Fusion Res., **18** 2405014 (2023).
[2] E. Yatsuka *et al.*, Fusion Eng. Des., **160** 111846 (2020).
[3] T. Ushiki *et al.*, J. Nuclear Materials, **595** 155047 (2024).

4 - 06 Measurement of beam energy spread in the AVF cyclotron using the beam energy and position monitor

N. Miyawaki [a)], H. Kashiwagi [b)], S. Watanabe [b)], N. S. Ishioka [b)] and S. Kurashima [a)]

[a)] Department of Advanced Quantum Beam Technology, QST
[b)] Department of Quantum-Applied Biosciences, QST

Introduction

The energy spread ($\Delta E/E$) of the beam accelerated by the TIARA AVF cyclotron was measured using the Beam Energy and Position Monitor (BEPM). The BEPM was installed on the straight beamline to measure the energy of the He beam used for ^{211}At production in real time [1]. The production rate of ^{211}At increases with the energy of the He beam up to approximately 30 MeV. However, when the beam energy exceeds 29 MeV, the isotope ^{210}At is produced, which decays into the highly toxic nuclide ^{210}Po. Therefore, we developed a method to control the beam energy in the cyclotron to obtain a high production rate of ^{211}At without generating ^{210}At [2]. The control of beam energy is achieved by varying the beam trajectory in the cyclotron. However, because the extracted beam from the cyclotron has an energy spread, it is necessary to measure not only the central energy but also the energy spread to ensure that the high-energy tail does not exceed the ^{210}At production threshold. Therefore, we developed a method to estimate the beam energy spread using the time-profile broadening observed in two voltage signals from the BEPM.

Measurement Method for ΔE/E using the BEPM

Voltage-induced signals are generated each time the beam bunch passes through the BEPM, which consists of two pickup electrodes (upstream and downstream) installed on the LA beamline. The time variation of the voltage signals obtained from the two pickup electrodes is shown in Fig. 1. The voltage signals varied in the order of minimum value, zero, and maximum value with each passing beam bunch.

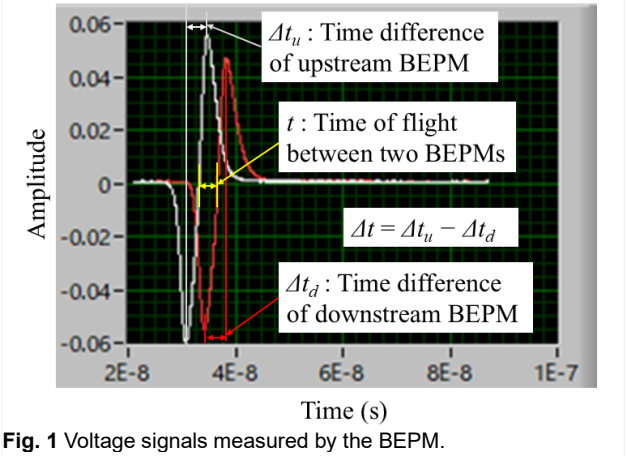

Fig. 1 Voltage signals measured by the BEPM.

In conventional energy measurement, the center of the beam bunch was defined as the zero-crossing point between the minimum and maximum signals of the pickup electrode. The time difference between the centers of the beam bunch at the two electrodes was measured as the flight time difference t, and the energy E was calculated as

$$E = E_0\left(\frac{1}{\sqrt{1-\beta^2}} - 1\right) = E_0\left[\frac{1}{\sqrt{1-\left(\frac{L}{t \times c}\right)^2}} - 1\right] \quad (1)$$

where E_0 is the rest energy, L is the distance between pickup electrodes, and c is the speed of light. On the other hand, beam bunches with finite energy widths increase in width along the traveling direction of the beam in the drift space. Unless acceleration or deceleration occurs after extraction, as in a cyclotron, the time difference in the traveling direction of the beam bunch increases from upstream to downstream. Therefore, the energy spread $\Delta E/E$ can be determined by measuring the difference Δt in the time width between the maximum and minimum values of the signal at the upstream and downstream electrodes of the BEPM, as given below.

$$\frac{\Delta E}{E} = \frac{1+\sqrt{1-\beta^2}}{1-\beta^2}\frac{\Delta\beta}{\beta} = \frac{1+\sqrt{1-\beta^2}}{1-\beta^2}\sqrt{\left(\frac{\Delta t}{t}\right)^2} = \alpha\frac{\Delta t}{t} \quad (2)$$

Measurement Results

The $\Delta E/E$ of the 50 MeV $^4He^{2+}$ beam used for ^{211}At production was obtained by measurements using the BEPM, as shown in Table 1. For comparison, Table 1 lists the $\Delta E/E$ for the 160 MeV $^{16}O^{5+}$ beam, which is adjusted to approach single-turn extraction requiring a small $\Delta E/E$, and for each beam with the buncher ON and OFF.

Table 1
Beam energy spreads $\Delta E/E$

Beam	Buncher ON	Buncher OFF
50 MeV $^4He^{2+}$	3.09E-03	4.90E-03
160 MeV $^{16}O^{6+}$	7.93E-04	1.99E-03

The $\Delta E/E$ for the $^4He^{2+}$ beam was larger than that for the $^{16}O^{6+}$ beam and the typical cyclotron value of 2.0E-03, regardless of the buncher. The larger $\Delta E/E$ of the $^4He^{2+}$ beam compared to typical values confirmed the expected influence of beam energy control. The effect of the ΔE/E of the $^4He^{2+}$ beam on the production of ^{211}At will be investigated by simulation. Additionally, the cyclotron will be adjusted to reduce the $\Delta E/E$ for the $^4He^{2+}$ beam, similar to the $^{16}O^{6+}$ beam.

References

[1] N. Miyawaki *et al.*, QST Takasaki Annu. Rep. 2022, **QST-M-47** 97 (2024).
[2] N. Miyawaki *et al.*, QST Takasaki Annu. Rep. 2023, **QST-M-52** 67 (2025).

4 - 07 γ-ray irradiation effect on ammonia radical derived from hydrothermal montmorillonite: A physical basis for the application to fault dating

T. Fukuchi

Faculty of Education, Graduate Faculty of Interdisciplinary Research, University of Yamanashi

Introduction

It is important to determine the absolute age of unrecognized active faults for the assessment of fault activity during the Quaternary period. The ESR (electron spin resonance) dating technique is applicable to radical centers detected from fault rocks [1]. Previous studies showed that the Mo quartet signals with the signal intensity ratio of 1:3:3:1, the intrinsic g-values and the hyperfine splitting parameter of A=2.4mT, which were originally detected from natural montmorillonite in fault rocks and attributed to hydronium (H_3O^+) radicals, can be used for fault dating [2]. Recent ESR studies have revealed that similar quartet signals are detected from the hydrothermally altered K-feldspar in naturally fractured granite and attributed to the ammonia ($\cdot NH_3^+$) radicals [3,4]. It remains unsolved whether the quartet signals from the hydrothermally altered K-feldspar are identical to the Mo quartet signals from montmorillonite.

Experimental

I carried out hydrothermal reaction experiments (for 2 weeks at 250°C) under pure water (H_2O) and an aqueous solution of 10%NH_4Cl using the JCSS (Clay Science Society of Japan) standard montmorillonite (JCSS-3102) and then investigated γ-ray irradiation effect on radical centers detected from the original standard and hydrothermal reaction samples using ESR. The γ-ray irradiation was carried out with a ^{60}Co source in the γ-ray irradiation facility (No.1 bld., No.1 cell) at Takasaki Advanced Radiation Research Institute, QST. The ESR measurements were done with an X-Band ESR spectrometer (JES-FA300) at the University of Yamanashi.

Results and Discussion

The standard sample (JCSS-3102) before γ-ray irradiation has shown the Mo quartet signals, however these signals irregularly increase by γ-ray irradiation, implying the signal saturation (Fig.1A). On the other hand, the hydrothermal reaction samples have no signal before γ-ray irradiation, and the Mo quartet signals emerge after γ-ray irradiation (Figs.1B and 1C). The radiation sensitivity of the Mo quartet signals from the sample under pure water becomes much lower than that from the standard sample, whereas that from the sample under an aqueous solution of 10%NH_4Cl is higher than the standard one. This indicates that NH_4^+ ions as precursors of $\cdot NH_3^+$ radicals existing in the interlayer of montmorillonite were eluted during the hydrothermal reaction under pure water, whereas NH_4^+ ions were replaced with K^+ ions existing in the interlayer during the hydrothermal reaction under an aqueous solution of 10%NH_4Cl. In conclusion, the Mo quartet signals originate from $\cdot NH_3^+$ radicals rather than H_3O^+ radicals.

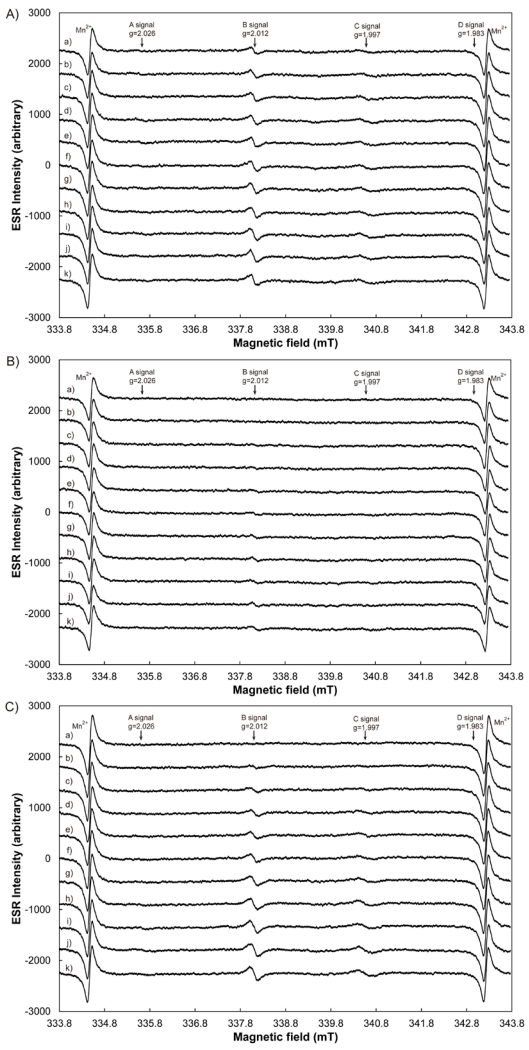

Fig. 1 γ-ray irradiation effect on radical centers detected from the standard and hydrothermal reaction samples. A) JCSS-3102 standard montmorillonite, B) hydrothermal reaction sample under pure H_2O, C) hydrothermal reaction sample under an aqueous solution of 10%NH_4Cl. ESR spectra were measured at 1 mW and room temperature. The irradiation dose rate is 281.9 Gy/h (A), 210.4 Gy/h (B) and 295.5 Gy/h (C). Irradiation time: a) 0h, b) 1h, c) 2h, d) 3h, e) 4h, f) 5h, g) 6h, h) 7h, i) 8h, j) 9h, k) 10h.

References

[1] T. Fukuchi, Radioisotopes, **70**, 131 (2021). Doi: 10.3769/radioisotopes.70.131

[2] T. Fukuchi, Jpn. J. Appl. Phys., **35**, 1977 (1996).

[3] T. Fukuchi, QST Takasaki Annual Report 2022, **2-26**, 66 (2024).

[4] T. Fukuchi, QST Takasaki Annual Report 2023, **2-19**, 47 (2025).

4 - 08 Inhibition of dentin demineralization by a newly developed fluoride gel

Y. Matsuda [a)], K. Okuyama [b)], H. Yamamoto [c)], M. Sakurai [a)], T. Saito [a)], M. Hayashi [c)], Y. Tamaki [b)], T. Sato [d)], N. Yamada [d)], and R. Yamagata [d)]

[a)] School of Dentistry, Health Sciences University of Hokkaido,
[b)] Asahi University School of Dentistry,
[c)] Graduate School of Dentistry, Osaka University,
[d)] Department of Advanced Quantum Beam Technology, QST

Introduction

One of the effective dental caries-preventing fluoride topical materials is high-concentration fluoride gel. The fluoride gel differs from fluoride varnish, which is hydrophobic; it is a water-soluble material, so it is easily applied to the tooth surface under a wet environment. Additionally, it could diffuse fluorine immediately to the dentin surface by applying the materials. The automatic pH-cycling system that we developed can simulate daily pH movement in the intraoral region. In this study, we investigated the effectiveness of fluoride gel as a topical application material by examining fluoride uptake and its demineralization-inhibiting effects using an automated pH cycling device and the In-air micro proton-induced gamma/X-ray emission（PIGE/PIXE） method.

MATERIALS AND METHOD

In this study, evaluation specimens of dentin were prepared using extracted bovine teeth. The root surfaces were smoothed with #1000 waterproof abrasive paper, then the non-polished areas were coated with sticky wax to create the specimens.

The materials evaluated were: as a fluoride varnish, 5% NaF White Varnish (FV, Solventam); and as fluoride gels, Fluor Jelly (FL, Beebrand Medico Dental) and Clinpro™ Clear Fluoride Gel (FG, Solventam). Each group was left undisturbed for 1 minute after application, then rinsed with water.The control group (C) underwent the same procedure without any application. After treatment, each sample was sectioned to a thickness of 200 μm to create single-section specimens. The sectioned surfaces were coated with sticky wax to prepare the specimens. The obtained specimens underwent one week of automated pH cycling treatment.

The fluorine content of each sample was analyzed using the proton-induced gamma-ray emission (PIGE) technique at the Takasaki Ion Accelerators for Advanced Radiation Application (TIARA) [18]. In-air micro-PIGE/PIXE (proton-induced X-ray emission) analysis was performed as described previously [19]. More specifically, the ZCF nanocomposite was attached directly to the window of an ion microbeam system, wherein a 3.0 MeV proton beam bombards the sample under ambient air conditions. The diameter of the beam spot was approximately 1 μm, and the beam current was 100 pA. The maximum scanned area was 1000μm2. A nuclear reaction [19F (p, αγ)160] was used for F estimation, wherein gamma rays were detected using an 81 cm sodium iodide detector placed 5 mm behind the sample. Micro-PIXE was simultaneously performed using a silicon lithium detector in vacuum to estimate the Ca concentration.

Results and Discussion

Figure 1 shows the distribution maps of calcium and fluoride. The material group demonstrated fluoride uptake into the surface layer of dentin even after pH cycling, indicating that fluoride is retained in the surface layer after loading. Furthermore, compared to the material group, the control group exhibited weaker calcium signals in the dentin surface layer, suggesting a tendency for the material group to inhibit demineralization.

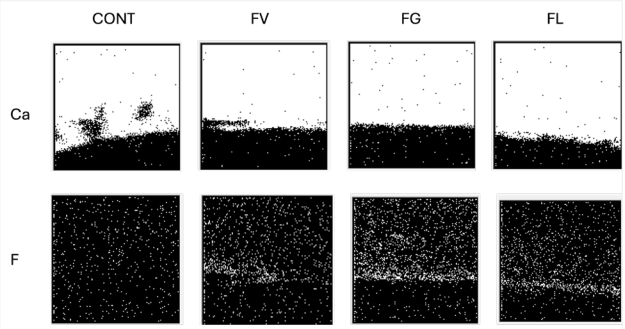

Fig. 1 Elemental PIXE map (calcium) and PIGE map (fluorine) of the dentin after the pH-cycle simulation. White dots in the maps (270 μm × 270 μm area) represent PIXE or PIGE signals from calcium, and fluorine, respectively.

This study suggests that applying fluoride gel to tooth surfaces enables rapid fluoride uptake into dentin and provides demineralization inhibition effects equivalent to those of varnish. In particular, gel formulations are expected to find clinical application as an alternative to varnish in cases where moisture control is difficult

References

[1] Yasuhiro, M. Nucl. Instr. Meth. B **348**, 156 (2015).

4 - 09 Production of Ba isotope having a specific nuclear spin I = 1/2 for quantum information processing

H. Shimada [a)], N. Miyawaki [a)], Y. Yuri [a)], K. Narumi [b)], I. Sasaki [c)], S. Watanabe [c)], and N. Ishioka [c)]

[a)] Quantum Materials and Applications Research Center, QST
[b)] NanoTerasu Center, QST
[c)] Department of Quantum-Applied Biosciences, QST

Introduction

In the field of quantum information processing, trapped and cooled atomic ions have drawn attention as information carrier. Ions having non-zero nuclear spin $I > 0$, have been widely investigated in this context. In particular, ions with I = 1/2 having the simplest hyperfine structure are advantageous for their capabilities of precisely manipulating and discriminating the quantum states [1]. However, only limited kinds of such ions have been trapped and laser-cooled so far; namely, $^{111}Cd^+$, $^{171}Yb^+$, and $^{199}Hg^+$. These ions have their main optical transitions in the UV range, posing some difficulties in optical manipulations and long-distant communications.

Recently, a new ion $^{133}Ba^+$ (I = 1/2) has been added to this list [2]. Its main optical transitions are in the visible range, evading the above difficulties. One drawback of this otherwise suitable ion is that it is radioactive (half life of 10.5 yr); its treatment requires special facilities, and it is usually provided by manufacturers only in the form of hydrochloric or nitric acid solution.

Usually, atoms are laser-ablated from a solid-state target and then loaded into a trap. It has been reported that released Ba atoms/ions from strongly ionic compounds such as $BaCl_2$ tend to have higher energies and thus difficult to load into traps compared to weakly ionic compounds [3]. Therefore, for efficiently loading ^{133}Ba into ion traps, weakly or non-ionic compounds are desirable. The final goal of this study is to produce weakly or non-ionic chemical compounds of radioactive ^{133}Ba appropriate for the ablation target in the atom source used in ion trap experiments.

Experimental

For this purpose, we have investigated various nuclear reactions leading to the production of ^{133}Ba nuclei. One such reaction,

$$^{nat}Ba + p^+ \rightarrow {}^{133}La + x \rightarrow {}^{133}Ba + \gamma$$

is investigated in the present experiment. Solid targets of $^{nat}BaCO_3$ and $^{nat}BaTiO_3$, are irradiated by a proton beam (E = 30 MeV) from the AVF cyclotron of TIARA. The time-developments of γ ray spectra from the irradiated targets are investigated using a Ge spectrometer. The dose of irradiation in the experiment is varied from 10^{-4} to 10^{-1} μAh for covering both short-time (t < 24h) and long-time (t > 10 d) behavior of the whole decay chains including various time constants. The populations of various nuclei are then extracted from the measured γ ray spectra and are compared with the calculated results using a Monte Carlo simulation code PHITS [4].

Results and Discussion

Figure 1 shows typical time dependences of radioactivity of various nuclei relevant for this study calculated using PHITS. The analysis of the experimental γ ray spectra is in progress. As far as analyzed so far, overall good agreement has been obtained between the experimental and the calculated results. Thus, it is likely that the experimental irradiation conditions are well characterized and that the nuclear reactions and subsequent decays are quite close to those described by the PHITS calculations. In particular, the observed and calculated radioactivity of ^{133}Ba well agrees with each other.

After establishing the correspondence between experimental and calculated results, we will next try increasing the concentration of ^{133}Ba within the target, necessary for a practical ^{133}Ba atomic source.

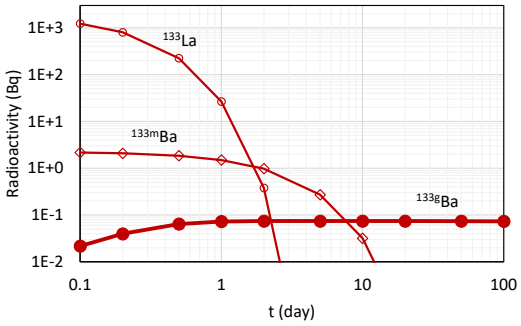

Fig. 1 Typical time dependences of radioactivity calculated using PHITS code.

Acknowledgments

This work was supported by the JST Moonshot R&D Grant Number JPMJMS2063.

References

[1] S. Olmschenk *et al.*, Phys. Rev. A **76**, 052314 (2007). DOI: 10.1103/PhysRevA.76.052314
[2] J. E. Christensen *et al.*, npj Quantum Inf. **6**, 35 (2020). DOI: 10.1038/s41534-020-0265-5
[3] B. M. White *et al.*, Phys. Rev. A **105**, 033102 (2022). DOI: 10.1103/PhysRevA.105.033102
[4] T. Sato *et al.*, J. Nucl. Sci. Technol. **61**, 127 (2024). DOI: 10.1080/00223131.2023.2275736

4 - 10 Development of a 553 nm light source for Ba isotope selective excitation using a distributed feedback laser and a periodically poled $LiNbO_3$ waveguide

K. Tamura, H. Shimada, H. Kashiwagi, R. Nakanishi,
K. Ogura, K. Hosaka, and K. Narumi

Quantum Materials and Applications Research Center, QST

Introduction

A light source for barium excitation is applicable to barium isotope excitation and loading to an ion trap, where barium isotope is considered as a qubit candidate in quantum computation schemes with high fidelity state preparation and measurement [1]. In this application, the light source needs to have sufficient output power and power stability.

In this report, a 553 nm light source for Ba excitation was developed using a distributed feedback (DFB) laser, and a Zn-doped periodically-poled $LiNbO_3$ (PPLN) ridge waveguide, and the laser output power required to Ba isotope selective loading were measured.

Experimental

DFB laser module operated at the wavelength of 1107 nm was set on a laser mount and was controlled by a laser diode driver. The DFB fiber connector is directly connected to the PPLN input connector for second harmonic generation (SHG). The temperature of the PPLN waveguide is controlled with a temperature controller.

Results and Discussion

Figure 1(a) shows the 1107 nm and 553 nm power as a function of DFB current. It was estimated by the output power from the fiber connector of the module measured with a power meter. Since 1107 nm output in the PPLN output was negligible, the PPLN output power was regarded as 553 nm output. The 1107 nm output increased linearly with the DFB current and was approximately 86 mW at the DFB current 200 mA. The SHG power increased and showed saturation at high DFB current region. The maximum 553 nm output at the DFB current 200 mA was approximately 15mW. Since the barium loading rate of approximately 60 ions /min was reported for the first step power of 5mW [2], the 553 nm output from our system was sufficient for loading.

Figure 1(b) shows the photon conversion efficiency, where PPLN temperature was adjusted to maximize the output at each point. The efficiency started to saturate at a fundamental power above approximately 160 mW. The photon conversion efficiency was approximately 18 % at the maximum DFB current. The normalized conversion efficiency is also shown in Fig. 2(b).

For the continuous utilization of the developed laser system, laser output power was monitored. Figure 2 shows the long-term stability of the 1107 nm and 553 nm output power, which were measured at 10 second intervals, where typical room temperature change during these measurements was approximately 0.5-0.7 degree. During 4 hours of operation, the reduction of 1107 nm output power was less than 0.2 %, showing 1107 nm output was very stable. The reduction of 553 nm output was approximately 2 % and was also stable. The reduction of 553 nm output power in this measurement was caused by the slight detuning of optimal thermal conditions by room temperature change during this period, which was readily recovered by re-optimization of the thermal tuning.

The laser wavelength stability required for selective tuning to the isotope was also realized by strict thermal insulation of the laser system.

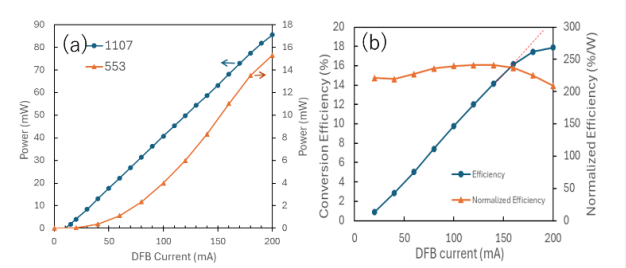

Fig. 1 (a) DFB output power (1107) and SHG power (553) as a function of DFB current. (b) The conversion efficiency and normalized conversion efficiency as a function of DFB current.

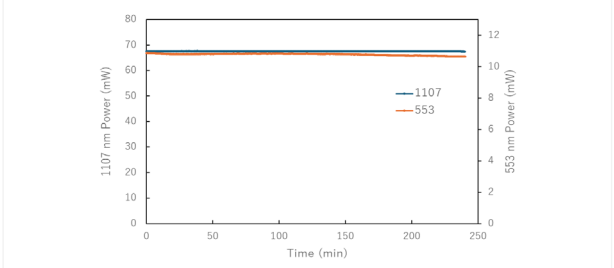

Fig. 2 Long-term stability of DFB and SHG output power.

Acknowledgments

This research is supported by the JST Moonshot R&D Grant Number JPMJMS2063, and QST President's Strategic Grant QST Advanced Study Laboratory.

References

[1] J.E. Christensen *et al.*, npj Quantum Inf **6**, 35 (2020). DOI: https://doi.org/10.1038/s41534-020-0265-5

[2] G. Leschhorn *et al.*, Appl Phys B **108**,159 (2012). DOI: https://doi.org/10.1007/s00340-012-5101-y

4 - 11 Electron-stimulated luminescence of liquid water under electron energies near the Cherenkov threshold

K. Enomoto [a)], Y. Nagao [a,b)], T. Yabe [a)], M. Tsuda [a], M. Yamaguchi [a)], S. Yamasaki [b)], S. Kano [c)], N. Nagasawa [b)], and N. Kawachi [a, d)]

[a)] Department of Quantum-Applied Biosciences, QST, [b)] Department of Advanced Quantum Beam Technology, QST, [c)] Takasaki Establishment, Radiation Application Development Association, [d)] Radiation Science, Medicine and Drug Development, & Industrial Applications for Radiation, F-REI

Introduction

When charged particles travel through liquid water at speeds below the Cherenkov light (CL) threshold (245 keV) in the medium, they emit weak luminescence.[1] However, the luminescence produced in water by electron deposition is often obscured by the background noise in the radiation field.[2] In this study, we present a method to suppress bremsstrahlung X-rays generated during electron-beam irradiation, thereby enabling the visualization of faint sub-threshold luminescence in water, as well as its energy dependence and the transition to CL.

Experimental

Luminescence images emitted from water phantom were acquired with a charge-coupled device (CCD) camera (Hamamatsu C4742-98-24ER) equipped with a Spacecom lens. The sample cell consisted of an 84 × 84 × 30 mm^3 acrylic cuvette with one transparent window and blackened sides, filled with 43 mL of ultrapure water. The camera was located perpendicular to the direction of electron beam irradiation. Lead-block shielding adjacent to the camera was used to minimize irradiation damage.

Electron beam irradiation (0.5 MeV, 0.1 mA) of the water phantom was performed at QST Takasaki (Fig. 1a). The electron beam was collimated through a 20 × 20 mm^2 aperture. A 3 mm-thickness polyethylene plate was placed on the irradiation surface of the collimator to suppress bremsstrahlung X-rays generated during electron beam irradiation. The cutoff energy, ranging from 200 to 300 keV, was controlled by varying the thickness of aluminum films (309–485 μm) used as a low-pass filter; the corresponding energy was calculated using PHITS simulation.[3] During electron beam irradiation of the phantom under air, luminescence imaging was performed with the CCD camera for 120 s and subsequently analyzed using ImageJ.

Results and Discussion

At 244 keV, faint sub-threshold luminescence was observed around the water surface, attributable to energy deposition by the incident electrons (Fig. 1b). Within the sub-threshold region, the luminescence intensity increased further. The luminescence yield exhibited a strong dependence on beam energy, increasing exponentially between 200 and 300 keV (Fig. 1c). No clear onset of CL was observed. This increase reflects both sub-threshold luminescence and the transition to CL. The former likely dominates even above 245 keV, because the mode of the energy distribution lies 36 keV below the cutoff energy. At a cutoff energy of 281 keV, for example, the mode is located near 245 keV; hence, the contribution of CL is minor.

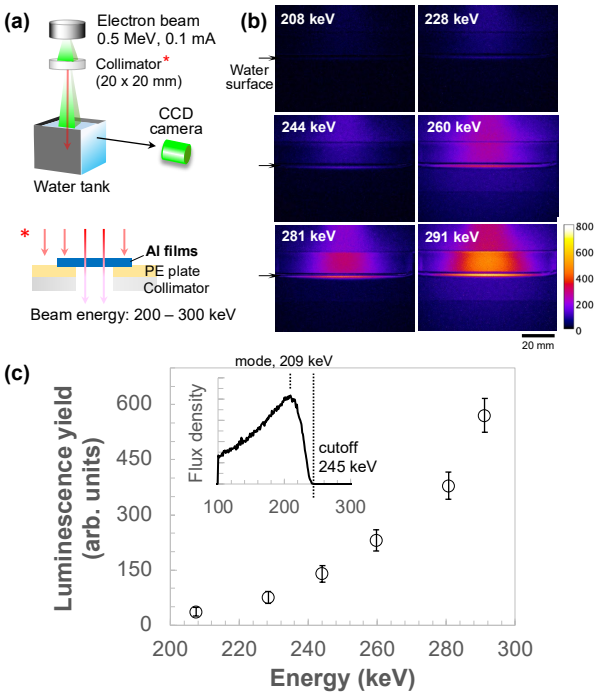

Fig. 1 (a) Experimental setup and the CCD detection system. (b) Electron-stimulated luminescence images of the water phantom irradiated at 200–300 keV for 120 s. (c) Luminescence yield of neat water as a function of the incident electron energy. Inset shows energy distribution at a cutoff energy of 245 keV. The error bars represent ±3SD.

We visualized sub-threshold luminescence in water by suppressing bremsstrahlung X-rays during electron-beam irradiation. This noise-reduction method may contribute to the elucidation of the underlying luminescence mechanism.

Acknowledgments

This research was performed by the commissioned research fund provided by F-REI (JPFR24040101). This research is partly supported by TERUMO LIFE SCIENCE FOUNDATION and JSPS KAKENHI Grant Numbers JP23H03774.

References

[1] S. Yamamoto, Radiol. Phys. Technol. **14**, 16 (2021). DOI: 10.1007/s12194-020-00588-x

[2] K. Enomoto *et al.*, QST Takasaki Annu. Rep. **2023**, 73 (2025).

[3] T. Sato, *et al.*, J. Nucl. Sci. Technol. **61**, 127 (2024). DOI: 10.1080/00223131.2023.2275736

4 - 12 Development of an ultra-high-intensity spin-polarized positron pulse beam

M. Maekawa [a)], A. Kawasuso [b)], A. Ishida [b)] and T. Namba [b)]

[a)] Department of Advanced Quantum Beam Technology, QST
[b)] Department of Physics, Graduate School of Science, and International Centre or Elementary Particle Physics (ICEPP), The University of Tokyo

Introduction

Positronium (Ps), a hydrogen-like bond of a positron and an electron, has been attracting attention as the first antimatter system for achieving Bose - Einstein condensation (Ps-BEC). This is due to its potential for the next-generation quantum technologies, such as ultra-short gamma-ray lasers. The critical condition for Ps-BEC is a density of Ps of over 10^{18}/cm³ at a cooling temperature of 10 K. The Ps cooling has been successfully achieved by a laser cooling method [1], however, the production of such high-density positronium remains a hard challenge.

When both positrons and electrons are not spin-polarized, the positroniums of spin singlet (para-Ps, |00>, here |S, M_s> denotes a state with total spin S and magnetic quantum number M_s) and spin triplet (ortho-Ps, |11>, |10>, |1-1>) states are produced in a 1:3 ratio. However, the majority (approximately 95%) of positronium annihilate within hundreds of picoseconds before Ps-BEC occurs due to unnecessary processes, such as self-annihilation of the |00> state, magnetic quenching of the |10> state or molecule formation of the |11> and |1-1> states [2]. On the contrary, if both positrons and electrons are fully spin-polarized, only the |11> state necessary for Ps-BEC are generated. Employing spin-polarized positrons enables significant enhancements in efficiency, which makes it advantageous in the realization of Ps-BEC.

From above conditions, the required intensity of positron beam is estimated to be the range of 10^{14} to 10^{15} e^+/s for a continuous (DC) beam. No facility currently exists that can generate such a high-intensity positron beam. Therefore, we have developed a spin-polarized positron accumulator to enhance beam intensity by converting a weak DC positron beam into a high-intensity single pulse with reference to previous studies [3,4].

Present status of development of positron accumulator

Schematic of the positron accumulator is shown in Fig.1. Incident positrons with an energy of 50 eV lose their energy to several eV by the collisions with gas molecules when they pass through a deceleration area equipped with a gas inlet. Subsequently, they are trapped in an electrostatic potential, which is formed by several ring electronodes. Trapped positrons accumulated over several hundred seconds are rapidly ejected as a single pulse beam, exhibiting an intensity that is enhanced by two orders of magnitude. Although this apparatus is under construction, beam tests are scheduled to commence in near future.

To produce spin-polarized positron beam, a compact

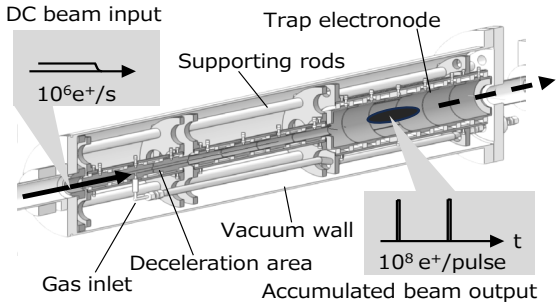

Fig. 1 Schematic diagram of a positron beam accumulator. This apparatus generates a single intense pulsed beam from a continuous slow positron beam.

Na-22 source with a small active area of 2 mm was fabricated (Fig. 2). Using this source and the accumulator, the positron pulse including 10^8 e^+ is expected. To exceed the critical density of the Ps-BEC, this pulse must be focused onto the diameter of 5 μm. Our small source is advantageous for focusing the beam to a smaller size. By the production of a larger amount of positron source using nuclear reactions based on the cyclotron accelerator, such as ^{68}Ge or ^{44}Sc [5], the realization of Ps-BEC would be further facilitated.

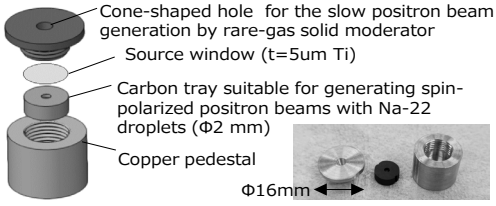

Fig. 2 A compact Na-22 source for generating a high-brightness spin-polarized positron beam. The activity of this source is 500 MBq.

Acknowledgments

This work was supported by JSPS KAKENHI Grant No. 23H05462 and JST CREST JPMJCR23O3.

References

[1] K. Shu *et al.*, Nature **633**, 793 (2024). DOI: 10.1038/s41586-024-07912-0
[2] O. Morandi *et al.*, J. Phys. B: At. Mol. Opt. Phys. **47** (2014) 155202. DOI:10.1088/0953-4075/47/15/155202
[3] D. B. Cassidy *et al.*, Rev. Sci. Inster.**77** (2006) 073106. DOI:Rev. Sci. Inster.77 (2006) 073106
[4] J. Clarke *et al.*, Rev. Sci. Inster.**77** (2006) 063302. DOI:10.1063/1.2206561
[5] M. Maekawa *et al.*, QST Takasaki Annu. Rep. 2022, **QST-M-47** 98 (2023).

4 - 13 Dose response of the ESR signal intensity of the heat-treated E_1' center in quartz in aeolian dust

K. Okada [a], S. Toyoda [b] and M. Takada [c]

[a] Graduate School of Science and Engineering, Okayama University of Science
[b] Institute of Paleontology and Geochronology, Okayama University of Science
[c] Department of Geography, Nara Women's University

Introduction

Analysis of aeolian dust is an essential approach to identifying its provenance and reconstructing variations in the direction and intensity of monsoon during past glacial and interglacial periods. The number of oxygen vacancies in quartz observed as the ESR signal of the E_1' center has been employed for such studies [1].

The E_1' center is an oxygen vacancy in quartz (SiO_2) with an unpaired electron. It is well known that the E_1' center is enhanced upon heating. It was proposed to be due to transfer of electronic holes trapped at Al centers ($[AlO_4]^0$) migrating upon heating to one of the two electrons at the Si–Si bond of an oxygen vacancy and recombination of one of the electrons, thereby forming the E_1' center [2]. Utilizing this property, it has was demonstrated that the signal intensity of E_1' center observed after irradiation and subsequent heating represents the number of oxygen vacancies in quartz [3] (heat-treated E_1' center).

A gamma-ray dose is required to form the Al center from which a hole is transferred. It was reported that the dose should be above 200 Gy [3]. In the subsequent practical studies, doses around 2.5 kGy are commonly employed [4]. In this study, we examined the dose response using actual samples in order to find the appropriate dose to be given.

Experimental

Quartz particles (20–50 μm in diameter) extracted from aeolian deposits at the Kamiyoshida outcrop, Rokunohe, Aomori Prefecture, at a depth of 180–185 cm from the top were used in the present study. Gamma-ray irradiation was conducted at the ^{60}Co gamma-ray facility of the Takasaki Institute for Advanced Quantum Science. Aliquots with 100 mg were given doses of 200–5000 Gy (2.42–5.47 C/kgh), followed by heating at 300 °C for 15 minutes.

Electron spin resonance (ESR) measurements were performed with an ESR spectrometer, JEOL JES-PX2300, at Research Instrument Center, Okayama University of Science. The measurements were carried out at room temperature under the following conditions: microwave power of 0.01 mW, magnetic field modulation frequency of 100 kHz, and modulation amplitude of 0.1 mT. The peak height of the observed E_1' center signal was taken as the signal intensity.

Results and Discussions

The observed results are shown in Fig. 1. The signal intensity of the E_1' center increased with dose up to 1000 Gy, reached saturation, and increased again at 5000 Gy.

This trend of reaching saturation is consistent, though at slightly different dose, with a previous report indicating that above 200 Gy, the number holes transferring from Al centers becomes sufficient, while the concentration of oxygen vacancies is limited, therefore, the heat treated E_1' center signal intensity approaches a constant value [3].

The slight increase in the signal intensity at 5000 Gy would also be in agreement with a paper that oxygen vacancies are formed at high gamma ray doses, albeit with low efficiency [5].

Conclusion

Taken together, these results suggest that a dose of 2.5 kGy is acceptable for the purpose of observing the number of oxygen vacancies at the saturating level without substantial artificial increase. However, the results also indicate that lower doses, such as 1 kGy, are sufficient and even preferable in order to avoid additional formation of oxygen vacancies.

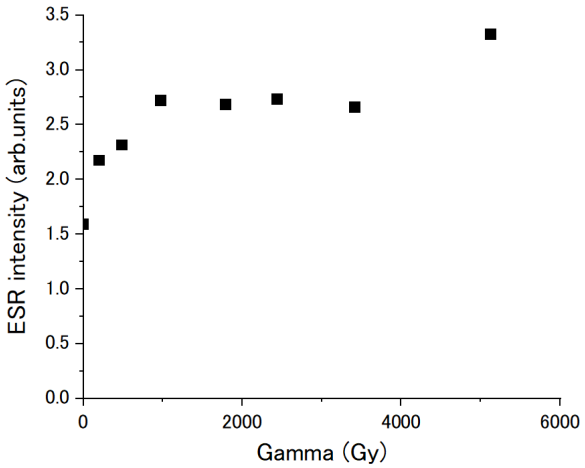

Fig. 1 Dose response of the E_1' center ESR signal intensity after irradiation and heating (heat treated E_1' center).

References

[1] S. Toyoda and T. Naruse, Japanese Geomorphological Union **23**, 811-820 (2002).
[2] M. Jani *et al.*, Phys. Rev. B **27**, 2285-2293 (1983).
[3] S. Toyoda and M. Ikeya, Geochem. Jour. **25**, 437-445 (1991).
[4] K. Nagashima *et al.*, Geochemistry Geophysics Geosystems **8**, Q02Q04 (2007).
[5] Toyoda *et al.*, Appl. Radiat. Isot. **47**, 1393-1398 (1996).

4 - 14 Enhancing sensitivity and stability in liquid LIBS with a sheet jet: application to precious metal analysis

R. Nakanishi [a)], M. Saeki [a)] and H. Ohba [b)]

[a)] Department of Advanced Functional Material Research, QST
[b)] Department of PhysicsCollaborative Laboratories for Advanced Decommisioning Science(CLADS), JAEA

Introduction

The recovery and recycling of precious metals have become critical due to their limited supply and increasing demand. Recovery processes often involve extracting these metals from acidic aqueous solutions, making it essential to monitor the residual metal content in real-time. Conventional analytical methods like Atomic Absorption Spectroscopy (AAS) or Inductively Coupled Plasma (ICP) techniques are laboratory-based, require sample pre-treatment, and are too time-consuming for on-site, real-time monitoring.

Laser-Induced Breakdown Spectroscopy (LIBS) offers a promising alternative for rapid, in-situ elemental analysis. However, its application to liquid samples faces a major challenge: liquid splashing and surface fluctuations caused by laser ablation quench the plasma, which degrades sensitivity and reproducibility. To overcome this, this study proposes a LIBS technique combined with a liquid sheet jet. By using a thin liquid sheet, liquid splashing is mitigated, resulting in a more persistent and luminous plasma [1]. Furthermore, to enable the direct analysis of the highly corrosive solutions used in metal recovery, a novel, acid-resistant glass slit nozzle was developed. This work demonstrates the sensitive and direct detection of six precious metals (Au, Pt, Pd, Ag, Rh, and Ru) in acidic solutions using this new system [2].

Experimental

The experimental setup consisted of a liquid recirculation system, a Q-switched Nd:YAG laser (532 nm), and a Czerny-Turner spectrometer equipped with an intensified charge-coupled device (ICCD) camera. A custom-fabricated glass slit nozzle with an exit of 0.3 x 0.6 mm was used to generate a stable liquid sheet jet with a thickness of 10-20 μm. Due to its resistance to corrosion, this nozzle allowed for the direct analysis of acidic samples without pre-treatment. Sample solutions were prepared by diluting ICP standard solutions with either 5 wt% HCl (for Au, Pt, Rh) or 5 wt% HNO_3 (for Ag, Pd, Ru). The 532 nm laser pulse was focused onto the liquid sheet to generate plasma. The resulting optical emission was collected at a right angle to the laser beam and guided via an optical fiber into the spectrometer for analysis.

Results

First, the optimal liquid sheet thickness for LIBS measurements was determined to be 14 μm by analyzing the emission intensity and signal-to-background ratio (SBR). Experimental parameters, such as laser energy and gate delay time, were then optimized to maximize the SBR for the selected analytical lines. The optimal laser energy was 60 mJ/pulse, while the optimal gate delays varied significantly by element: 6–8 μs for Au and Pt, and longer than 15 μs for Ag, Pd, Rh, and Ru. Under these optimized conditions, univariate calibration curves were constructed (Fig.1) and showed excellent linearity ($R^2 > 0.998$) for all elements. From these curves, the limits of detection (LODs) were calculated as: Au(0.62 mg L^{-1}), Pt 0.97 mg L^{-1}, Pd (0.09 mg L^{-1}), Ag (0.14 mg L^{-1}), Rh (0.09 mg L^{-1}), and Ru (0.15 mg L^{-1}). These values are all below 1 mg L^{-1} and represent a significant improvement over previously reported results for direct liquid LIBS [3], with the LODs for Pd and Rh being the first reported for direct liquid analysis.

This research successfully demonstrated the sensitive detection of six trace precious metals in acidic solutions using a novel liquid sheet jet LIBS system equipped with an acid-resistant glass nozzle.

Acknowledgments

This work was supported by JSPS KAKENHI (Grant Number JP24K00622) and the Adaptable and Seamless Technology transfer Program through Target-driven R&D (A-STEP) from the Japan Science and Technology Agency (JST) (Grant NumberJPMJTM20KV)

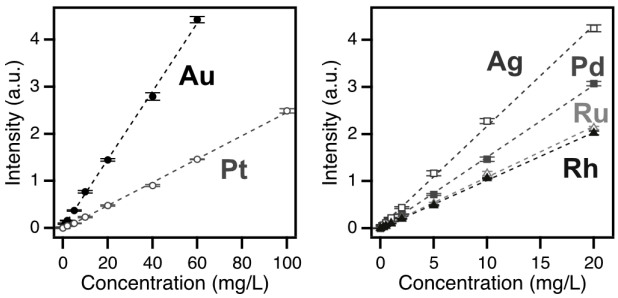

Fig. 1 Calibration curves for each analyte element.

References

[1] R. Nakanishi *et al*., Opt. Express **29**, 5205 (2021). DOI: 10.1364/oe.415308
[2] R. Nakanishi *et al*., J. Anal. At. Spectom. **40**, 1185 (2025). DOI: 10.1039/d4ja00467a
[3] N. Schlatter *et al*., Spectrosc. J., **2**, 1 (2024). DOI: 10.3390/spectroscj2010001

4 - 15 Study of multi ion-irradiation effects on fusion reactor materials using a micro-tensile testing method

M. Ando and T. Nozawa

Department of Fusion Reactor Materials Research, QST

Introduction

Reduced activation ferritic/martensitic steels (RAFM) such as F82H and EUROFER97 are candidates for DEMO blanket structural materials. Many reactor irradiation studies have shown possible neutron irradiation effects on RAFM, however, the details of the 14 MeV fusion neutron effect are still unknown since a fusion neutron irradiation facility is currently unavailable. Instead, several simulated fusion neutron irradiation damage experiments are used to understand their effects. For instance, ion irradiation experiments using multiple accelerators can partially simulate the characteristics of fusion neutron irradiation, i.e., displacement damage and helium production at a certain rate, however unfortunately the evaluation volume is very small and only limited evaluation methods can be applied.

In the past, as ion irradiation experiments and post-irradiation examinations, evaluation of void swelling (mainly cavity microstructure analysis) has been conducted mainly by electron microscope observation, and strength for irradiated materials (irradiation hardening/softening) has been conducted by micro-hardness tests.

On the other hand, while the ductility and brittleness after irradiation can be assessed to some extent by evaluating the fracture surface after tensile testing, there have been few examples of micro-sized specimens. Therefore, in this study, neutron-irradiated F82H with pre-evaluated macro-mechanical properties was used to compare fracture surfaces after micro-tensile tests before and after irradiation, and an evaluation of the relationship between fracture surface changes and macro-properties was performed. Furthermore, comparisons were made with fracture surface results obtained from ion-irradiated F82H, which had been studied previously.

Experimental

It is considered that a kind of fracture stress (μ-FS) and fracture surface morphology for a single-block F82H can be obtained by using μ-tensile specimens with notches because the local constraint occurs around notches [1]. Evaluation samples included unirradiated F82H (ductile-brittle transition temperature: -84°C for 1/3CVN specimen) and F82H irradiated at 300°C, 5 dpa in the HFIR (ductile-brittle transition temperature: 23°C for 1/3CVN specimen) [2]. Notched micro-tensile tests were performed on these samples. The fracture surfaces after failure were examined using SIM imaging, and the fracture surface morphologies were compared.

Results and Discussion

Five micro-tensile tests were performed on the neutron-irradiated sample. Figure 1 shows the results evaluated for deformation near the notch, compare with the results for the ion-irradiated F82H. Previously, ion-irradiated F82H around 300°C showed a tendency for deformation (ductility) to decrease with increasing irradiation dose (blue markers plot). This same trend was confirmed for neutron-irradiated F82H irradiated at 300°C and 5 dpa (red markers plot). As shown on Figure 2, regarding fracture surface morphology, while unirradiated F82H exhibits necked fracture surfaces (ductile behavior: fracture surfaces cannot be matched together), ion-irradiated F82H tends to show reduced necking and flat-like fracture surfaces (brittle behavior: fracture surfaces can be matched together). A similar trend was observed in neutron-irradiated F82H. As the irradiation dose increases, the tendency toward flat fracture surfaces also increases. Since macro-strength information cannot be obtained from ion-irradiated F82H, this method can provide useful judgmental information for evaluating the deformation capability (ductility/brittleness) of irradiated F82H at room temperature through micro-tensile testing.

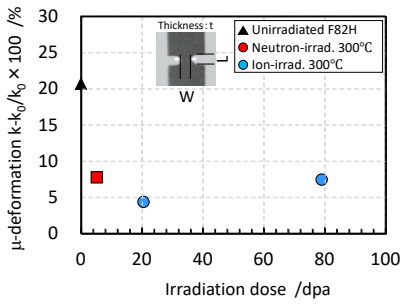

Fig. 1 Irradiation dose dependence of notch-root dimension changes

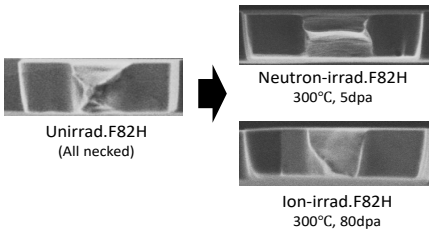

Fig. 2 Example of fracture surface results (observed from the tensile axis direction): In non-irradiated F82H, a necked fracture surface is observed, while neutron/ion-irradiated F82H tends to exhibit a flat-like fracture surface, enabling brittle fracture identification.

References

[1] M. Ando *et al*., Nucl. Mater. Energy **41**, 101731 (2024). DOI: 10.1016/j.nme.2024.10731

[2] H. Tanigawa *et al*., Fusion Sci Technol **44**, 206 (2003). DOI: 10.13182/FST44-206

5 - 01 Utilization status at the TIARA facility

H. Hanaya[a)], I. Ishibori[a)], S. Watanabe[a)], M. Sugimoto[a)]
N. Kubota[a)], T. Shimizu[b)] and S. Kaneya[c)]

[a)]Department of Advanced Quantum Beam Technology, QST,
[b)]Takasaki Establishment, Radiation Application Development Association
[c)]Beam Operation Co., Ltd.

Four kinds of accelerators, a cyclotron and three electrostatic accelerators (tandem accelerator, single-ended accelerator and an ion implanter), are used at the TIARA facility to meet various researchers' needs. The activities of research fields that the cyclotron was used for the past 5 fiscal years are shown in Fig. 1. Total utilization time of each fiscal year (FY) was in the range of 379 to 1,095 hours. The utilization time of FY 2021, FY 2022 and FY2024 was lower than FY 2020 because of changing of the cyclotron daily operating time from 24 hours to 14 hours. And also, the utilization time of FY 2023 was lower than the other fiscal years because the operation time was decreased under the influence of the rising energy costs. The utilization time of "Life Science" and "Material Science" accounted for more than about 70% of the total time.

On the other hand, for the three electrostatic accelerators, as shown in Fig. 2, the utilization time of "Material Science" and "Basic Technology of Quantum Beam" accounted for more than about 50% of the total time. Total utilization time of each fiscal year was in the range of 330 to 390 days.

The trend of the number of project category (Internal use, Joint research, Cooperation priority research, and Facility use program) for the past 5 years is shown in Fig. 3. The total number of projects was in the range of 55 to 68 per year.

The trend of the number of users in the past 5 years is shown in Fig. 4. The total number of users was in the range of 286 to 493 per year.

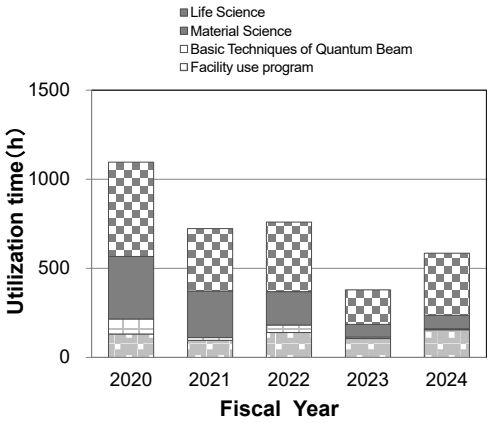

Fig. 1. Research activities for the cyclotron for the past 5 years.

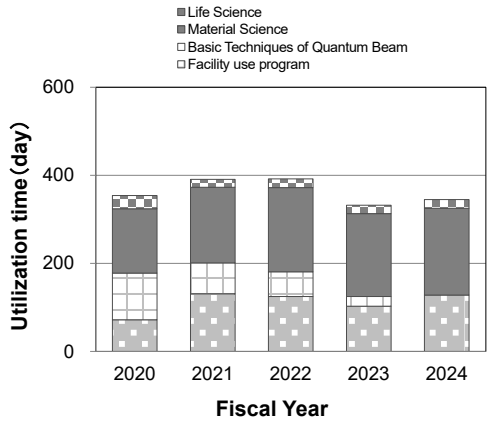

Fig. 2. Research activities for the three electrostatic accelerators for the past 5 years.

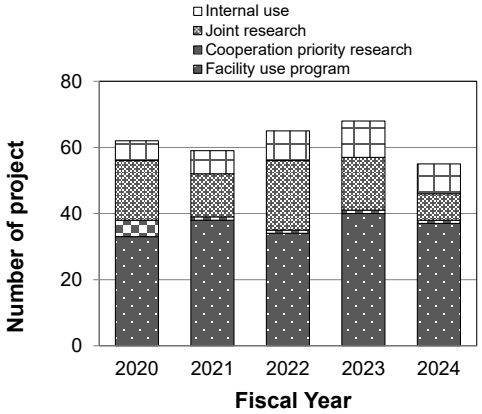

Fig. 3. The number of projects for the past 5 years.

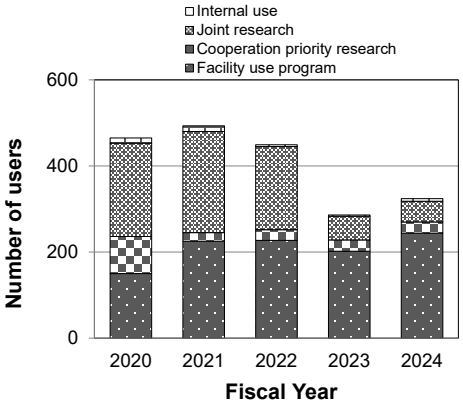

Fig. 4. The number of users for the past 5 years.

5 - 02 Operation of the AVF cyclotron

K. Yoshida, T. Yuyama, T. Ishizaka, S. Hosoya, K. Takano,
H. Saitoh, N. Miyawaki, H. Kashiwagi, and S. Kurashima

Department of Advanced Quantum Beam Technology, QST

Operation

At the start of operation of the cyclotron in fiscal 2024, a malfunction occurred in the synthesizer of RF system. After replacing the synthesizer with a used one, the cyclotron was operated without any serious trouble.

Due to the high electricity costs since last year, the operation period for the general users of the cyclotron was only twenty days. However, total operation times increased by 45 percent compared with the previous year because of increase of machine users which paid all the cost for operation. The annual operation times of the cyclotron ultimately reached 966 hours, and the number of experiments of the year was 108.

The accumulative operation times was 91681 hours, and the total number of experiments was 13041 from the first beam extraction in 1991 to March 2025

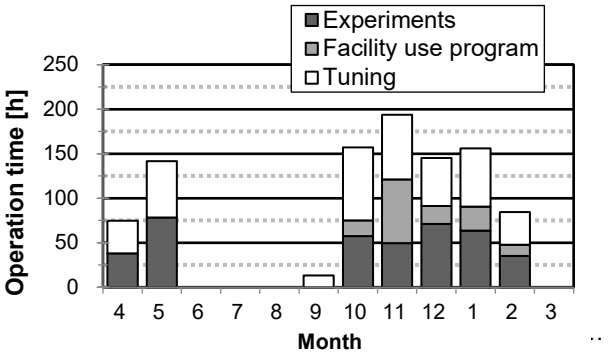

Fig. 1 Monthly operation times in fiscal 2024

Table 1
Statistics for cyclotron operation.

Fiscal year	2024	2023
Beam service time	542 h	346 h
Beam tuning	424 h	302 h
Machine study	0 h	8 h
Total operation time	966 h	656 h
Change of particle and/or energy	107 times	77 times
Change of beam course	96 times	63 times
Change of harmonic number	37 times	28 times
The number of experiments	108	86
Cancellation due to machine trouble	0	0

Monthly operation times are shown in Fig. 1. Table 1 shows the statistics of the cyclotron operation of fiscal 2024, with the data of fiscal 2023 for comparison. The percentages of operation times of the year used for regular experiments, facility use program and promotion of shared use program, beam tuning are 40.7%, 15.4%, and 43.9%, respectively. Table 2 shows the total operation times of each ion source. NANOGAN ion source is used to produce H, D, and He ions. For production of ions heavier than He, HYPERNANOGAN ion source is used. OCTOPUS ion source which has been used as backup ion source for HYPERNANOGAN. However, OCTOPUS ion source is not available except for periodic inspection owing to a trouble of the remote-control system. Therefore, the total operation times was only 0.2 hours. Fractional distribution of major ions used for experiments is shown in Fig. 2.

Table 2
Operation times of ion sources.

ECR Ion source	2024	2023
NANOGAN	598.4 h (58.5%)	305.3 h (43.4%)
OCTOPUS	0.2 h (0.0%)	4.6 h (0.7%)
HYPERNANOGAN	424.4 h (41.5%)	393.2 h (55.9%)

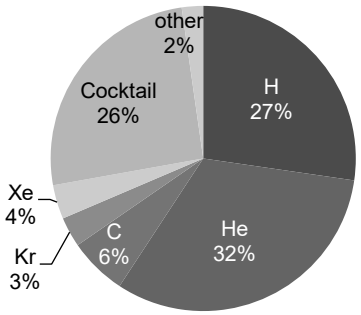

Fig. 2 Ion species used for experiments in fiscal 2024

Machine trouble and maintenance

The scheduled maintenances were carried out from summer to autumn and at the end of fiscal year. The major items of maintenance were polishing the deflector electrodes and total characteristic test of the RF system. The other items of maintenance were as follows: 1) Replacement of the water pump of cooling system for the trim coils. 2) Inspection of all power supply for magnet coils. 3) Change of lubricating oil for 47 vacuum pumps. 4) Replacements of internal power supply and cooling fan in the device controller of the cyclotron.

When the operation resumed at the end of September, malfunctions occurred again this year because of long time shutdown. The malfunctioned devices were the relay board for vacuum gauge (CCG) and the unit of turbo molecular pump (TTPLD1). The number of machine troubles and maintenances of the fiscal year were 87 and 19, respectively.

5 - 03 Operation of electrostatic accelerators in TIARA

A. Chiba, K. Yamada, Y. Hirano, R. Suganuma,
S. Kanai, Y. Aoki, M. Hashizume, and S. Kurashima

Department of Advanced Quantum Beam Technology, TIAQ, QST

Out of the experiments with ion beams scheduled to be conducted in FY2024 using three electrostatic accelerators in TIARA, all irradiation experiments assigned to the tandem accelerator and the single-ended accelerator were completed as planned, but two experiments with the ion implanter were postponed due to serious troubles. The annual operating times, including conditioning operations for voltage stabilization, of the tandem accelerator, the single-ended accelerator, and the ion implanter were 1111.3, 1115.7, and 815.5 hours, respectively. The trends in annual operating times of each accelerator since its first beam and the operating times by the use patterns over the past three years are shown in Fig. 1 and Fig.2, respectively. The annual operating times of the three accelerators were almost the same as last year, but the ratio of facility use programs increased for each accelerator. Figure 3 shows the utilization ratio of ion species for each accelerator. Among the ion species provided by the tandem accelerator and the ion implanter, ions of N^+, Ni^+, Sn^+, Si^+, and Pr^+ were mainly used in experiments to develop functional materials with quantum effects. For users of the ion implanter, we are actively developing ion beams of rare earth elements such as Pr, which are relatively difficult to ionize. Previous experiments using Er^+ ion beams had been plagued by current instability, but by adopting $ErCl_3$ as a new source material of the ion beam, we succeeded in generating a stable beam of 200 nA. Table 1 summarizes the number of troubles and maintenance cases for each accelerator in FY24. The numbers of parentheses indicate those from last fiscal year. The tandem accelerator has experienced more troubles recently than the other two. One possible cause is a series of failures due to deterioration over time and initial defects in the newly updated equipment. Major troubles with the tandem accelerator included offset-error drift in the GVM value, failure of the cooling water chiller, defect in the control device of the magnet power supply, and malfunction of the assignable controller. The quartz tube of the RF ion source equipped on the single-ended accelerator has been replaced with a new one approximately every two years. The ion beam intensity generated by the new quartz tube that was replaced this year was about half of the normal intensity, so early replacement was deemed necessary. Two irradiation experiments assigned to the ion implanter were postponed due to troubles: a large water leak caused by a rupture in a urethane tube supplying cooling water to the beamline equipment, and a leak of the sample gas inlet tube on the ion source of the ion implanter. As part of facility maintenance, the aging surveillance cameras installed in the accelerator rooms and target rooms were upgraded. The new surveillance system allows a total of 12 cameras to be remotely controlled from any PC on the internal network.

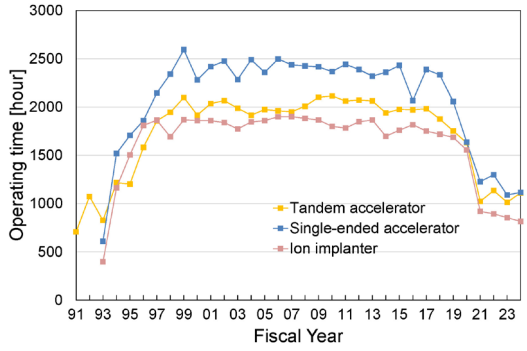

Fig. 1 Transitions of annual operating times.

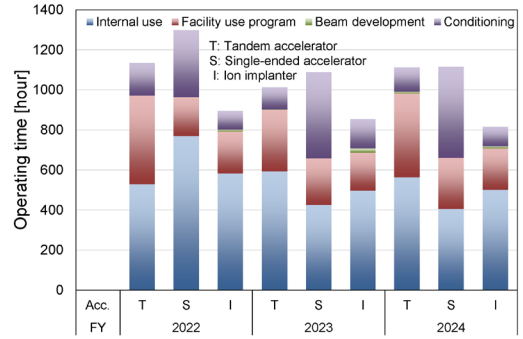

Fig. 2 Operating times for use patterns over the past three years.

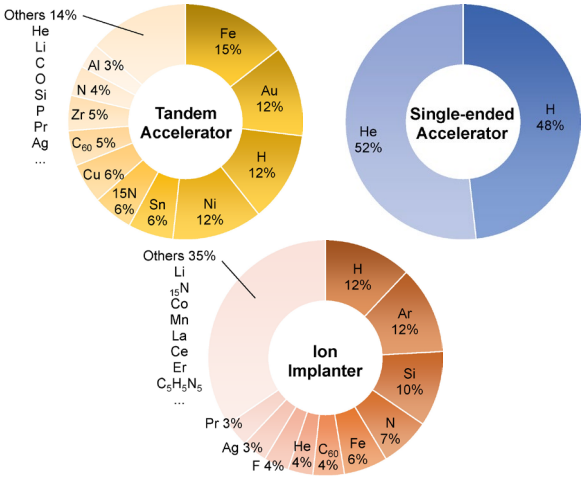

Fig. 3 Utilization ratio of ion species.

Table 1
Number of machine troubles and maintenances.

	Tandem Accelerator	Single-ended Accelerator	Ion Implanter
Minor trouble	21 (20)	4 (9)	10 (10)
Serious trouble	10 (8)	4 (1)	3 (3)
Maintenance	26 (27)	16 (17)	12 (11)
Cancellation or Postponement	0 (1)	0 (0)	2 (0)

5 - 04 Operation, maintenance and utilization status of the cobalt-60 gamma-ray irradiation facilities

Y. Nagao[a)], E. Yokozuka[a)], H. Seito[a)], M. Takagi[b)], N. Yagi[b)], T. Agematsu[a)], S. Yamasaki[a)], and N. Nagasawa[a)]

[a)] Department of Advanced Quantum Beam Technology, QST
[b)] Takasaki Establishment, Radiation Application Development Association

Operation

The cobalt-60 (^{60}Co) gamma-ray irradiation facilities at the Takasaki Institute for Advanced Quantum Science operated smoothly during fiscal year (FY) 2024. The food irradiation facility was permanently closed at the end of February 2022.

The ^{60}Co gamma-ray irradiation facilities, consisting of two buildings with six irradiation rooms, cover a wide dose-rate range from 2×10^{-1} Gy/h to 7×10^{3} Gy/h as of March 2025. As shown in Fig. 1, the annual operation times were 15,362 hours for the first facility and 31,706 hours for the second. Due to seismic retrofitting of the buildings, the annual operation times of the first and second ^{60}Co gamma-ray irradiation facilities were reduced in FY 2021. The annual operation times of the first and the second ^{60}Co gamma-ray irradiation facilities in FYs 2022–2024 increased from that in FY 2021. However, the total annual operation time remained below FY 2020 levels due to the closure of the food irradiation facility. Additionally, the annual operation time of the first ^{60}Co gamma-ray irradiation facility did not increase significantly due to the extended maintenance period.

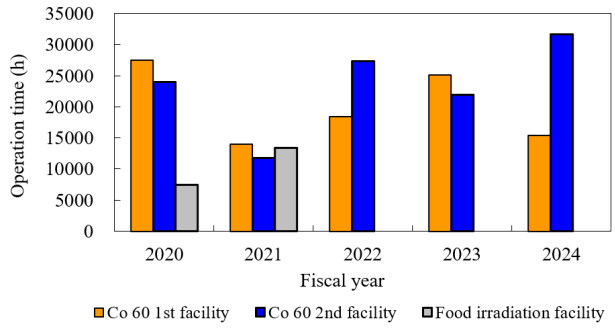

Fig. 1 Annual operation time of the gamma-ray irradiation facilities from FY 2020 to FY 2024.

Maintenance

The water purification system for the pools of the ^{60}Co gamma-ray irradiation facilities was damaged due to long-term use. In November 2024, the drain pump of the primary storage tank, which stores overflowed water from the pools and neutralized water after restoring ion exchange resins, failed and was replaced in December 2024. In addition, the pH meter of the primary storage tank was also replaced in March 2025.

The annual maintenance check focusing on mechanical systems for radiation source transport is performed every year at one of the ^{60}Co gamma-ray irradiation facilities in turn. The maintenance check of the first ^{60}Co gamma-ray irradiation facility was carried out from July to September 2024, during which operations were suspended for 75 days.

Utilization

The two facilities were operated for various research subjects according to the operation plans of the FY 2024. Figure 2 shows the irradiation time and the number of experiments by research fields in FY 2024. The facilities were mainly used in the field of materials science, including research on metal absorbents, biocompatible protein hydrogels, polymer membranes for fuel cells, and radiation-resistant materials and components of the International Thermonuclear Experimental Reactor (ITER). Furthermore, radiation effect tests on microorganisms and plants in the life science field were conducted.

In the field of materials science, long-term radiation resistance evaluations of fusion reactor equipment and materials are being conducted. In contrast, in the field of life science, including research on the effects of irradiation on animal and plant cells, irradiation time is often short (e.g. on the order of a few tens of minutes), and experiments are conducted frequently.

The facility use program is often used to evaluate the radiation resistance of space electronic equipment and nuclear reactor materials.

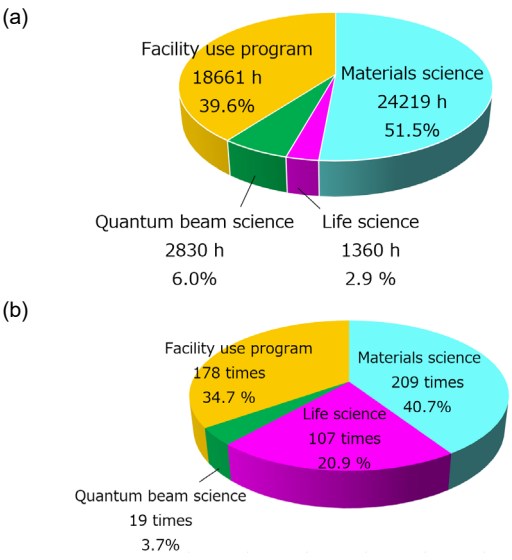

Fig. 2 The irradiation time (a) and the number of experiments (b) by research fields in FY 2024.

5 - 05 Operation, maintenance and utilization status of the electron accelerator

S. Yamasaki [a)], H. Seito [a)], E. Yokozuka [a)], S. Kano [b)], M. Takagi [b)], N. Yagi [b)], T. Agematsu [a)], Y. Nagao [a)] and N. Nagasawa [a)]

[a)] Department of Advanced Quantum Beam Technology, QST,
[b)] Takasaki Establishment, Radiation Application Development Association

Operation

The electron accelerator in Takasaki Institute for Advanced Quantum Science was operated smoothly during fiscal year (FY) 2024.

Figure 1 shows the annual operation time from FY2020 to FY2024. The accelerator was used for various research projects according to the FY2024 operation plan. In FY2020, the facility use program decreased significantly due to the COVID-19 pandemic, but the QST's internal use increased, resulting in approximately 1,000 hours of operation similar to typical years.

In FY2021, a long shutdown of about 10 months occurred due to seismic retrofitting and upgrades to the electronic flow control system, reducing operation time to about 300 hours-roughly 30% of a normal year. Except for FY2021, the annual operation time was about 1,000 hours, nearly reaching the upper limit in the current operation plan.

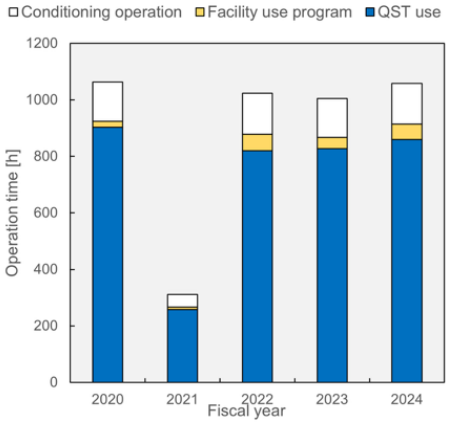

Fig. 1 Annual operation time from FY2020 to FY2024.

Maintenance

Major failures and maintenance activities in FY2024 included:

(1) Repair of the high voltage switching device
(2) Repair of the electron current control system
(3) Repair of the shielding door in the horizontal irradiation room

(1) The high voltage switching device, which applies high voltage to the horizontal acceleration tube, was damaged, suspending horizontal operation since 2022. As the components were nearly 40 years old and no longer manufactured, replacement parts were procured, and custom connectors and fixtures were fabricated to complete the repair.

(2) The electron current control system consists of two subsystems: an optical converter and inverter control. The optical converter adjusts electron flow with high precision by switching current ranges (1 mA, 10 mA, 30 mA) via relays. The optical converter for vertical electron current measurement and the mercury relay used for horizontal range switching were damaged and replaced with new parts.

(3) The electric opening/closing function of the shielding door malfunctioned due to cracks in welded joints of hinges and drive shafts caused by long-term use. Although welding repairs were performed, wear and misalignment between the hinge and drive shafts could not be fully repaired. Therefore, mechanical adjustments were made to restore proper function.

Utilization

Figure 2 shows the operation time by experimental fields in FY2024. The accelerator was used by QST researchers in materials science for the experiments of quantum materials such as diamond for quantum sensors, catalysts for fuel cell and polymer modification (grafting polymerization, crosslinking, and degradation) for biodevices.

It was also used by the facility use program for radiation resistance studies on satellite materials and components. Approximately 70% of the operation time was devoted to quantum material development, which has higher demand than actual usage. To meet user requirements, it is necessary to increase the upper limit by revising the operation plan.

Development is underway to introduce a new electron beam irradiation facility (3 MV–20 mA), scheduled for completion in FY 2027.

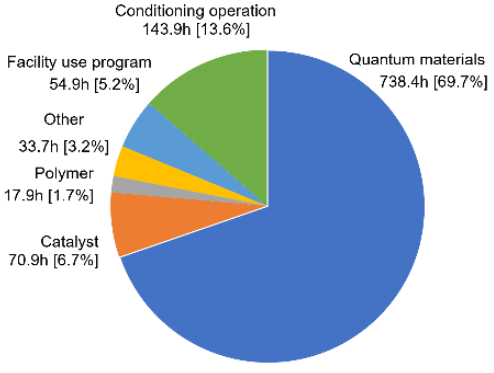

Fig. 2 The operation time by experimental fields in FY2024.

5 - 06

Radiation monitoring in QST Takasaki

Department of Administrative Services, QST

Individual monitoring

(1) Individual monitoring for radiation workers

Table 1 shows the distribution of effective doses among radiation workers in FY 2024. The effective dose values for almost all radiation workers were below the detection limit of 0.1 mSv. However, seven workers had effective doses from external exposure that exceeded this detection limit.

The maximum effective dose from external exposure received by one worker was 0.3 mSv/y, resulting from experiments with unsealed radioisotopes at TIARA.

Table 1

Distribution of effective doses among radiation workers in FY 2024.

Items		Quarterly totals and annual unique count				
		1st quarter	2nd quarter	3rd quarter	4th quarter	Annual
Distribution of people by effective dose range	HE ＜ 0.1	391	435	534	549	733
	0.1 ≦ HE ≦ 1.0	3	4	0	0	7
	1.0 ＜ HE ≦ 5.0	0	0	0	0	0
HE:Effective dose *1 (mSv)	5.0 ＜ HE ≦ 15.0	0	0	0	0	0
	15.0 ＜ HE	0	0	0	0	0
Total number of people (A)		394	439	534	549	740
Exposure above 1mSv	Number of people (B)	0	0	0	0	0
	(B)/(A)×100(%)	0	0	0	0	0
Collective dose (Person･mSv)		0.3	0.5	0.0	0.0	0.8
Mean effective dose (mSv)		0.00	0.00	0.00	0.00	0.00
Maximum effective dose (mSv)		0.1	0.2	0.0	0.0	0.3

*1 The effective dose from internal exposure was not detected.

(2) Individual monitoring for visitors and others

Table 2 shows the number of people who temporarily entered the radiation-controlled areas. The effective doses for all people were less than 0.1 mSv.

Table 2

Number of people who temporarily entered the radiation-controlled areas in FY 2024.

Quarters	1st quarter	2nd quarter	3rd quarter	4th quarter	Total
Number of people	265	472	1,487	436	2,660

Monitoring of radioactive gases and dust at TIARA

Table 3 shows the maximum radioactive concentrations and total activities for radioactive gases released from the stack of TIARA during each quarter of FY 2024.

Small amounts of ^{11}C, and ^{41}Ar, were occasionally detected during the operation of the cyclotron or experiments, but the particulate radioactive substances (e.g., ^{65}Zn) were not detected.

Table 3

Monitoring results of released radioactive gases and dust in FY 2024.

Nuclide	Items \ Quarters	1st quarter	2nd quarter	3rd quarter	4th quarter	Total
^{41}Ar	Maximum concentration	$<1.1\times10^{-4}$	$<1.1\times10^{-4}$	$<1.1\times10^{-4}$	$<1.1\times10^{-4}$	
	Activity	0	0	0	7.0×10^{7}	7.0×10^{7}
^{11}C	Maximum concentration	$<1.1\times10^{-4}$	—	$<1.1\times10^{-4}$	$<1.1\times10^{-4}$	
	Activity	1.1×10^{8}	—	2.4×10^{8}	1.4×10^{8}	4.9×10^{8}
^{65}Zn	Maximum concentration	$<6.2\times10^{-10}$	$<6.0\times10^{-10}$	$<8.0\times10^{-10}$	$<7.2\times10^{-10}$	
	Activity	0	0	0	0	0

Unit : Bq/cm^3 for Maximum concentration, Bq for Activity.

Monitoring of external radiation and surface contamination at TIARA

The monitoring for external radiation and surface contamination was routinely performed in/around the radiation-controlled areas. Neither anomalous value of dose equivalent rate nor surface contamination was detected.

Figure 1 shows a typical example of the distribution of the γ-ray dose equivalent rate in the radiation-controlled area of the cyclotron building.

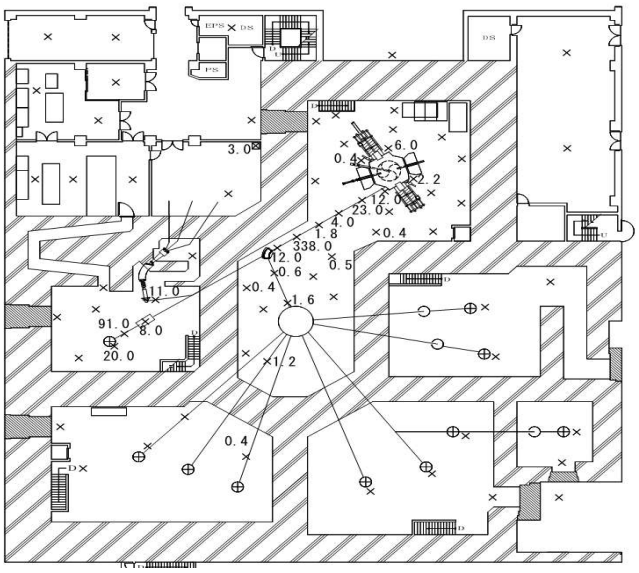

Fig. 1 Distribution of the γ-ray dose equivalent rate in the radiation-controlled area of the cyclotron building.
Measurement date : March 26 , 2024.
Measuring position : Indicated with × (1 meter above floor).
Unit : μSv/h(Values below 0.2 μSv/h are not displayed.)

5 - 07 Radioactive waste management in TIARA

N. Higuchi [a)], K. Iida [a, b)], H. Hanaya [b)], S. Watanabe [b)] and M. Sugimoto [b)]

[a)]Department of Administrative Services, QST
[b)]Department of Advanced Quantum Beam Technology, QST

Radioactive waste management

The radioactive waste generated in TIARA is managed by Utilization and Coordination Section. The main radioactive waste is the solid waste generated from research experiments and the maintenance of the cyclotron. Other radioactive waste is the liquid waste such as inorganic waste fluids generated from research experiments and the air-conditioning machines in the radiation controlled area. These wastes are managed according to their properties. Radioactive waste is stored in a storage facility and handed over to the Japan Radioisotope Association for disposal.

Solid radioactive waste

Table 1 shows the amounts of various types of solid waste generated in each quarter of FY 2024. Combustible waste consists of papers and clothes, and so on. Flame-retardant waste consists of rubber gloves, plastic articles, and polyethylene articles. Incombustible waste consists of metal pieces and the glasses, and so on. Solid waste emitting α, β, and γ is classified according to the properties.

Liquid radioactive waste

Table 2 shows the amounts of liquid waste generated in each quarter of FY 2024. The main liquid waste is inorganic water, which consists of condensed water generated from the air-conditioner installed in the radiation controlled area and waste water generated from chemical experiments. In Table 2, large amount of inorganic waste water is generated in 2nd quarter. It is due to the condensed water generated from the air-conditioner. To reduce the inorganic waste water, distillation of the inorganic waste water is carried out. After the distillation, small amount of distillation residual liquid remains, and that is discarded for liquid waste. On the other hand, the purified water prepared by distillation is reused in the radiation controlled area.

Table 1
Radioactive solid waste generated in FY 2024.

Amounts / Items	Amounts of generation in each period (m^3)					Number of package /drum
	1st quarter	2nd quarter	3rd quarter	4th quarter	Total	
Category β, γ*	0	0	0	0.16	0.16	10 *
Combustible	0	0	0	0.04	0.04	1 *
Flame-retardant	0	0	0	0.08	0.08	2 *
Incombustible(Compressible)	0	0	0	0.04	0.04	1 *
〃 (Incompressible)	0	0	0	0	0	6
Laboratory animal	0	0	0	0	0	0
Filters	0	0	0	0	0	-
Category α*	0	0	0	0.16	0.24	4
Combustible	0	0	0	0	0	0
Flame-retardant	0	0	0	0.12	0.20	4
Incombustible(Compressible)	0	0	0	0.02	0.02	0
〃 (Incompressible)	0	0	0	0	0	0
Laboratory animal	0	0	0	0.02	0.02	0
Filters	0	0	0	0	0	-

* defined by amount in Bq (β, γ): < 2 GBq , (α) : < 37 MBq
** 50-liter drum.

Table 2
Radioactive liquid waste generated in FY 2024.

Amounts / Items	Amounts of generation in each period (m^3)					Number of package /drum
	1st quarter	2nd quarter	3rd quarter	4th quarter	Total	
Category β, γ*	3.29	25.81	8.06	0.82	37.98	-
1)Inorganic	3.29	25.81	8.06	0.82	37.98	-
Inorganic	3.29	25.76	8.06	0.82	37.93	0
Distillation residual liquid, Sludge	0	0.05	0	0	0.05	2
2)Organic	0	0	0	0	0	0
Organic	0	0	0	0	0	0
Oil	0	0	0	0	0	0
Category α*	0	0	0	0	0	0

* defined by concentrations in Bq/mL (β, γ Inorganic) : < 200 kBq, (Organic) : < 2 kBq, (α) : ≤ 1.85 kBq

5 - 08 The Shared Use Program of QST facilities in Takasaki

S. Nozawa, H. Hanaya and A. Shimada

The First Office of Research Planning and Promotion,
Department of Management and Planning, QST

Introduction

The irradiation facilities at the Takasaki Institute for Advanced Quantum Science are available to researchers from universities, public institutions, and private-sector R&D divisions (hereafter “external users”).

Under the Shared Use Program of QST Facilities (“Shared Use Program”), external users can perform irradiation experiments using gamma rays, electron beams, and ion beams provided by Co-60 gamma-ray facilities, an electron accelerator, and four ion accelerators at TIARA. Users are responsible for the operating costs of these facilities.

Pricing system of the Shared Use Program

Charges under the Shared Use Program comprise service fees, irradiation fees, and additional costs (e.g., consumables and technical support).

Users conducting research intended for publication may receive partial discounts on irradiation fees, subject to approval of their research proposals by an expert committee. This discount does not apply to Co-60 gamma-ray facilities or the electron accelerator.

Irradiation experiments conducted under the Shared Use Program in FY2024

The number of irradiation experiments under the Shared Use Program in FY2024 is shown in Table 1. The number of experiments conducted at the Co-60 gamma-ray irradiation facilities was much higher than at other facilities.

Table 2 shows the number of experiments classified by users’ affiliations. The four accelerators at the TIARA facilities and the electron accelerator were mainly used by researchers from academia, such as universities and public institutes. In contrast, many users of the Co-60 gamma-ray irradiation facilities were from private companies.

Additional information about this program is available at the following QST website:
https://www.qst.go.jp/site/shisetsukyoyo-takasaki/

Table 1
Number of irradiation experiments under the Shared Use Program of QST Facilities in FY2024

Irradiation facility \ Pricing system		Public disclosure	Non-disclosure	Total
TIARA	AVF cyclotron	3	15	18
	3 MV tandem accelerator	28	17	45
	3 MV single-ended accelerator	20	5	25
	400 kV ion implanter	13	12	25
Co-60 gamma-ray irradiation facilities		-*	179	179
Electron accelerator		-*	15	15
Total		64	243	307

*: Discounting was not applied

Table 2
Number of irradiation experiments classified by user’s affiliations in FY2024

Irradiation Facility \ User’s affiliation		University	Public institute	Private company	Total
TIARA	AVF cyclotron	9	3	6	18
	3 MV tandem accelerator	30	11	4	45
	3 MV single-ended accelerator	10	15	0	25
	400 kV ion implanter	20	5	0	25
Co-60 gamma-ray irradiation facilities		25	19	135	179
Electron accelerator		9	2	4	15
Total		103	55	149	307

Appendix

Quantum Beam Facilities in QST Takasaki

Takasaki Ion Accelerators for Advanced Radiation Application (TIARA) consisting of four ion accelerators, an electron accelerator, and gamma-ray irradiation facilities are available to researchers in QST and other organizations for R&D activities on new functional and environmentally friendly materials, biotechnology, radiation effects of materials, and quantum beam analysis. We are developing various shape area irradiation technique at the cyclotron. In addition, technical developments of elemental map imaging by C_{60} fullerene microbeam at the electrostatic accelerators are in progress.

Takasaki ion accelerators for advanced radiation application: TIARA

TIARA facility

Cyclotron

Tandem accelerator

Single-ended accelerator

Ion implanter

Typical available ions

Accelerator	Ion	Energy (MeV)
AVF Cyclotron (K=110MeV)	H	10～ 80
	He	20～107
	C	75～320
	Ne	75～350
	Ar	150～520
	Fe	200～400
	Kr	210～520
	Xe	324～560
	Os	490
Tandem Accelerator (3 MV)	H	0.8～ 6.0
	C	0.8～18.0
	Ni	0.8～18.0
	Au	0.8～18.0
	C_{60}	0.8～9.0
Single-ended Accelerator (3 MV)	H	0.4～ 3.0
	D	0.4～ 3.0
	He	0.4～ 3.0
	e^-	0.4～ 3.0
Ion Implanter (400 kV)	H	0.02～0.38
	Ar	0.02～0.38
	Bi	0.02～0.37
	C_{60}	0.02～0.36

Energy-element range covered by the four accelerators

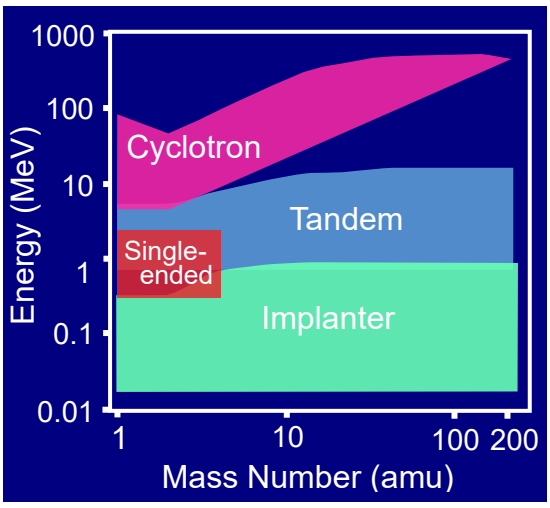

Cobalt-60 gamma-ray and electron beam irradiation facilities

Gamma-ray irradiation facility building

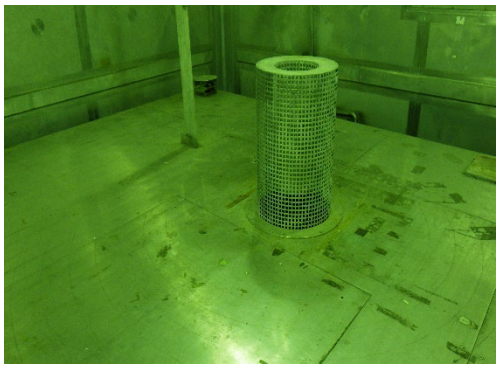

Gamma-rays irradiation room

Electron accelerator
(0.5～2.0 MeV, 0.1～30 mA)

Electron irradiation room with conveyor system

Specification

Apr. 2025

Name of facility	Cobalt-60 activity (PBq)	Number of rooms	Principal utilization
Co No.1 bldg.	3.5	3	Radiation-resistance test, radiation effects on materials as polymers, semiconductors, and biological substances as bacteria, cell, plant
Co No.2 bldg.	5.0	3	R & D on functional organic materials, inorganic materials and dosimetry

Dose-rate range

Unit：kGy/h

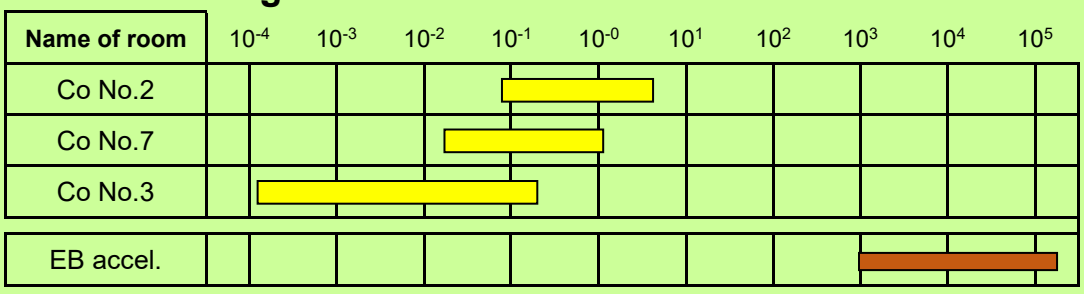

QST Takasaki Annual Report 2024
Research Promotion Office

Date of Publishing: February 2026

Takasaki Institute for Advanced Quantum Science
National Institutes for Quantum Science and Technology
1233 Watanuki, Takasaki, Gunma 370-1292, Japan

Tel: +81-27-346-9232
E-mail: taka-annualrep@qst.go.jp
Homepage: https://www.qst.go.jp/site/taka/

QST-M-56

https://www.qst.go.jp